

Rigidity and Elasticity beyond Isostaticity

by

Shang Zhang

A dissertation submitted in partial fulfillment
of the requirements for the degree of
Doctor of Philosophy
(Physics and Scientific Computing)
in the University of Michigan
2021

Doctoral Committee:

Associate Professor Xiaoming Mao, Chair
Associate Professor Emanuela Del Gado
Associate Professor Emanuel Gull
Professor Michael J. Solomon
Professor Robert M. Ziff

Shang Zhang

zhshang@umich.edu

ORCID iD: 0000-0003-0759-2080

© Shang Zhang 2021

To my parents and my girlfriend.

ACKNOWLEDGMENTS

I would like to express my greatest gratitude to my advisor Prof. Xiaoming Mao for her thorough guidance throughout the years of my PhD study. Without her, none of the materials in this thesis would be possible. Xiaoming always has the magic of sparking questions of importance, and turning unfinished ideas into fruitful results. Her continual guidance, support and care benefit me a lot, and help me learn how to become a critical thinker, problem solver and supportive collaborator. I am extremely fortunate to have Xiaoming as my advisor.

I must also thank Prof. Emanuela Del Gado for the great opportunity to collaborate with her. It benefits me a lot from her invaluable insights in our fruitful discussions. Besides, I would like to thank my other committee members, Prof. Emanuel Gull, Prof. Michael Solomon and Prof. Robert Ziff for providing me guidance and feedback that helped me with my thesis and becoming a better researcher.

It is my great honor to work with my excellent colleagues. Dr. Zeb Rocklin and Dr. Leyou Zhang guided me to start my research in the field of soft matter physics. I always enjoyed the academic discussions and beyond with my lab mates including Dr. Desh Bedi, Dr. Di Zhou, Harry Liu, Shae Machlus, Dr. Francesco Serafin, Dr. Ethan Stanifer and Dr. Farzan Beroz. I am also very fortunate to have the opportunities to work with outstanding physicists from Del Gado's group, including Dr. Mehdi Bouzid and Dr. Vishwas Vasisht. Thanks also to Boulder School 2017, for the insightful discussions and enjoyable moments.

I would like to extend my sincere thanks to my friends. Special thanks to Jia Li, for being supportive ever since high school and all the journey together at Michigan. Dr. Yangwenxiao Zeng, for sharing experience together as graduate students. Dr. Jiahua Gu, Dr. Xiao Zhang and Dr. Lin Li, for their help as senior graduate students. Liuxing Shen, Mengyi Sun, Hao Huang, etc. for having fun together at Ann Arbor. Thanks should also go to Ruoxi Wang, Yaotian Wang, Dr. Ruizhou Ding, Yihao Chen, Ziyao Yu and many others.

Finally, I would like to thank my parents and my girlfriend, Zhi Zheng. Their love gives me the momentum to pursue science while being able to appreciate all the other wonderful things in life. This thesis is dedicated to them.

TABLE OF CONTENTS

Dedication	ii
Acknowledgments	iii
List of Figures	vi
List of Abbreviations	xi
Abstract	xii
Chapter	
1 Introduction	1
1.1 Overview	1
1.1.1 Maxwell lattices and the isostatic point	1
1.1.2 Physics near isostaticity	4
1.1.3 Rigidity beyond isostaticity	8
1.2 Rigidity percolation	12
1.2.1 Connectivity percolation	12
1.2.2 Phenomena of rigidity percolation	13
1.3 Linear elasticity in discrete models	15
1.3.1 The equilibrium matrix and the compatibility matrix	16
1.3.2 States of self-stress (SSS) and zero modes (ZM)	18
1.3.3 The dynamical matrix	19
1.4 Outline	20
2 General Computational Techniques	22
2.1 The “pebble game” algorithm	22
2.1.1 The pebble search	23
2.1.2 Rigid cluster decomposition	25
2.1.3 Emergence of the spanning rigid cluster	27
2.2 Matrix decomposition in linear elasticity	29
2.2.1 Numerical orthonormal null space bases	30
3 Correlated Rigidity Percolation and Colloidal Gels	32
3.1 Introduction	32
3.2 Models and Methods	35
3.3 Results	37

3.4	Appendices	43
3.4.1	The “pebble game” method: rigid cluster decomposition	43
3.4.2	Colloidal gel simulation	44
3.4.3	Finite-size scaling for lattice model	45
3.4.4	The rigidity diagram for gelation of colloidal particles	51
4	Correlated Rigidity Percolation in Fractal Lattices	55
4.1	Introduction	55
4.2	Model	57
4.3	Method & Results	59
4.4	Interpretation	64
4.5	Conclusions, discussions, & extensions	67
4.6	Appendices	70
4.6.1	Calculating ϕ_{SGL}	70
4.6.2	Calculating Critical Exponents	71
4.6.3	Fragility of an SG	71
5	Prestressed Elasticity of Amorphous Solids	75
5.1	Introduction	75
5.2	Prestressed mechanical networks	79
5.2.1	Prestressed networks	79
5.2.2	Continuum elasticity with prestress	81
5.2.3	Prestressed rigidity	84
5.3	States of self-stress in stressed elasticity	86
5.3.1	States of self-stress in stress-free systems	86
5.3.2	States of self-stress and zero modes in prestressed systems	88
5.3.3	Stress distribution as linear combinations of states of self-stress	94
5.3.4	Dipole response	95
5.4	Prestressed triangular lattices	97
5.5	3D numerical simulations of soft repulsive particle assemblies	100
5.6	Results	103
5.6.1	Spatial heterogeneity of stress fields	103
5.6.2	Calculating stress response to shear using states of self-stress	104
5.6.3	General statistics of states of self-stress	106
5.6.4	Local dipole stiffness in prestressed glasses	108
5.7	Discussion	110
5.8	Appendices	110
5.8.1	SSSs formulation for shear response of prestressed networks	110
5.8.2	Dipole stiffness κ in prestressed systems	117
6	Summary and Outlook	124
6.1	Conclusions	124
6.2	Outlook	125
	BIBLIOGRAPHY	128

LIST OF FIGURES

FIGURE

1.1	Frames of bonds connecting $N = 6$ sites. (a) has 6 sites, 7 bonds, 5 ZMs and two floppy modes indicated by the dotted bonds. (b) has 6 sites, 8 bonds, 4 ZMs and one floppy mode. (c) and (d) are constructed from (b) by adding an additional diagonal bond. (c) satisfies the Maxwell's rule with only the three trivial ZMs. (d) has 4 ZMs and one SSS indicated by the arrows on the bonds in the left square.	3
1.2	Jamming phase diagram. Outside the shaded green region, at high temperature T , applied shear stress Σ , and high inverse density $1/\phi$, the system is unjammed and can flow; inside the shaded green region, the system is jammed. The lines in the $(T - 1/\phi)$ and $(1/\phi - \Sigma)$ planes represent the generic dynamical glass transition and yield stress, respectively. The point “ J ” marks the jamming transition for ideal spheres at zero temperature and applied stress.	5
1.3	(a) Packed bi-disperse discs just above the jamming transition. The dark red lines are chains of force that are a response to the pressure required to pack the particles at $z > z_c$. (b) A representative bond-diluted lattice near the rigidity percolation threshold of $z_c \approx 3.96$. (c) Square, (d) distorted square, (e) kagome lattice and (f) twisted kagome lattice.	7
1.4	(a) Original jamming phase diagram and (b) generalized jamming phase diagram with shear jamming in the $T = 0$ plane.	9
1.5	A colloidal gel sample with $\phi = 0.045$	11
1.6	The probability for a bond-diluted generic network to have a spanning rigid cluster with respect to bond concentration p . Periodic (free) boundary conditions with various system sizes are shown with solid (dashed) line segments drawn between data points.	14
1.7	A frame of six sites (<i>red numbers</i>) and nine springs (<i>circled black numbers</i>) and its 12×9 equilibrium matrix \mathbb{Q} with rows ordered according to the sites degrees of freedom, $\{x_1, y_1, x_2, y_2, \dots, x_6, y_6\}$, and columns ordered according to the springs.	17
2.1	Method for detecting cluster wrapping for connectivity percolation on periodic boundary conditions. In RP problem, all the sites in the connected cluster represent sites in the giant rigid cluster.	28

3.1	Examples of rigid cluster decomposition of the correlated lattice model ($\phi_l = 0.6$) at different correlation strengths [$c = 0$ in (a) and $c = 0.6$ in (b)], and the attractive gel model ($\phi_g = 0.6$) at $k_B T/\epsilon = 0.4$ in (c) and 0.1 in (d). Red particles belong to the largest rigid cluster, and other particles are colored in gray. In both models, correlation/attraction induces rigidity at volume fractions below the rigidity transition in the uncorrelated/repulsive limit. The rigid clusters percolate in (b) and (d) where there is strong correlation/attraction, but not in (a) and (c). The inset in (a) shows an extreme example where particles are perfectly correlated (on a Warren truss) and exhibit rigidity at $\phi = 0$ in thermodynamic limit.	35
3.2	(a) $P(\phi_l, c, L)$ at different L and c (symbols and line styles defined in legends). Inset: ν for different c (blue with error bars), in comparison with average (red line) and standard error (yellow dashed line) of ν in the classical RP (from Ref. [1]). (b) $\mathcal{M}(\phi_l, c, L)$ at different L and c . Inset: d_f for different c (blue with error bars), in comparison with average (red line) and standard error (yellow dashed line) of ν in the classical RP (from Ref. [1]). In both (a) and (b), curves for different L cross at the same point (marked by red lines), indicating continuous transitions at every c at different $\phi_{l,c}(c, L = \infty)$	38
3.3	Phase diagram of the correlated lattice model (without and with the strong correlation correction). Calculated phase boundary $\phi_{l,c}(c, L = \infty)$ are shown as yellow dots (before correction: with black circles around the dots, after correction: without circles; They overlap at small c). The red dashed line and the black solid line show the phase boundaries before and after the correction by connecting the dots, respectively. The $c \rightarrow 0$ limit (classical RP) is shown as the black dashed line. The insets are configurations taken at $c = 0.9$, $\phi_l = 0.5$ (the yellow star) with and without the strong correlation correction, which avoids the formation of disconnected dense blobs and leads to a percolating rigid cluster.	40
3.4	(a) Phase diagram of the attractive gel model. Simulated parameters ($\phi_g, k_B T/\epsilon$) are shown as squares colored according to their measured $P_g(\phi_g, k_B T/\epsilon)$ (color scale shown in legend). Black stars show fitted phase boundary at each $k_B T/\epsilon$ and the black line is the phase boundary from fitting these transition points to third order polynomial. The hard sphere limit of the transition is shown as a black dashed line. (b,c) show two example configurations with their rigid cluster decomposition, chosen at the two marked points on the phase diagram. The largest rigid cluster percolates in (c) but not in (b), agreeing with the phase boundary.	41
3.5	Linear extrapolation of the finite-size critical volume fractions as a function of $L^{-1/\nu}$ ($\nu = 1.21$ [2]). The dashed lines are linear fits, and the y-intersects of these dashed lines represent the infinite-size limit of the critical volume fractions $\phi_{l,c}(c, L = \infty)$	46
3.6	Transition point $\phi_{l,c}(c = 0, L = \infty)$ as a function of c for the correlated lattice model, without and with the strong correlation correction.	47
3.7	The fitting of the phase boundary as a function of the correlation strength c , as described in Eq. (3.10), without and with the strong correlation correction. . . .	48

3.8	Collapsing of data for P , the probability of having a spanning rigid cluster, for the correlated RP, showing the master curve $\tilde{\mathcal{P}}(z)$, where $z = [\phi_l - \phi_{l,c}(c, L = \infty)]L^{1/\nu}$ and $\nu = 1.21$. The exponent is from the uncorrelated RP[2]).	49
3.9	Collapsing of data for \mathcal{M} , the mass of rigid cluster in the correlated RP, showing the master curve $\tilde{\mathcal{M}}(z)$, where $z = (\phi_l - \phi_{l,c}(c, L = \infty))L^{1/\nu}$ and $\beta = 0.18, \nu = 1.21$. The exponents are from the uncorrelated RP [2].	50
3.10	<i>Bond Orientational Order Parameter</i> (BOP) in sample configurations. (a,b) $k_B T/\epsilon = 0.23, \phi = 0.6$. (c,d) $k_B T/\epsilon = 0.38, \phi = 0.6$. (a,c) BOPs without the damping process. (b,d) BOPs with the damping process.	53
3.11	Fitting of $P_g(\phi_g, k_B T/\epsilon)$ to second order polynomial in two example cases, 9a) $k_B T/\epsilon = 0.2$ and (b) $k_B T/\epsilon = 0.35$, where the black stars indicate the extrapolated transition point defined as $P_g(\phi_g, k_B T/\epsilon) = 0.5$	54
4.1	(a,b) Sierpiński gasket (SG) of fractal iteration $n = 2, 5$. (c,d) Lattices of SG's are models for ultra-low-density networks at $n = 2, 5$. In (c) semi-transparent purple disks represent the physical particles we are modeling. The diameter of each particle is equal to the bond length, which we set to 1.	59
4.2	(a) The correlation length exponent ν_{SGL} at $n = 1, 2, 3, 4, 5$. (b) The spanning rigid cluster fractal dimension $d_{f,\text{SGL}}$ for the five values of n . The red lines show these exponents for classical RP in the regular triangular lattice ($\nu = 1.21 \pm 0.06$ and $d_f = 1.86 \pm 0.02$) [1]. The error bars are 95% confidence intervals.	62
4.3	Extracting $p_{c,\text{SGL}}(n, L = \infty)$ from the linear extrapolation of the finite-size critical occupancy fractions $p_{c,\text{SGL}}(n, L)$ as a function of $L^{-1/\nu_{\text{SGL}}}$ where $\nu_{\text{SGL}} = 1.21$. The lines are linear fits, and the y-intercepts are the infinite-size limit of the critical occupancy fractions $p_{c,\text{SGL}}(n, L = \infty)$. The error bars are 95% confidence intervals.	63
4.4	The triangular plate model (TPL) is a regular triangular lattice which has been diluted in units of upwards pointing equilateral triangles (black).	65
4.5	The difference between the upper bound on $p_{c,\text{SGL}}$ given by the TPL, $P_{c,\text{SGL}}$, and the measured $p_{c,\text{SGL}}$ becomes smaller as n increases. The error bars are 95% confidence intervals.	67
4.6	(a) The correlation length exponent ν_{SGL} and (b) the fractal dimension $d_{f,\text{SGL}}$ for the SGL are both obtained from the slopes of the linear fits for each n according to Eqs. (4.7) and (4.8). The error bars are 95% confidence intervals.	69
4.7	(a) An $n = 1$ SG. (b) Removing any non-corner site (red) from an $n = 1$ SG leaves two rotors attached to a rigid triangle. The triangle and both rotors (particles with only one bond) each have a corner site (black), so all three corner sites belong to distinct rigid clusters.	72
4.8	(a) An $(n + 1)$ -level SG, composed of three n -level SG's (black). (b) Case (i), a site connecting two n level SG's (red) is removed, allowing independent motion of the three corner sites (black). (c) Case (ii), a non-corner site is removed from an n -level SG (gray with white hatching). If the three corners of the n -level SG are in separate rigid clusters, the three corners of the $(n + 1)$ -level SG can move independently and are thus also in separate rigid clusters.	73

5.1	Prestress in structural engineering and materials science.	76
5.2	Prestressed rigidity. (a) A mechanical network of concentric similar triangles. When stress-free, this network has one floppy mode. When prestressed, this floppy mode is eliminated. Black dashed arrows denote the floppy mode. Green (red) bonds are under tension (compression). The thickness of the bond is proportional to the magnitude of the prestress. (b) A honeycomb lattice exhibits an extensive number of floppy modes. When prestressed (equal tension on all bonds), these floppy modes are eliminated. (c) Phonon dispersion relation of the honeycomb lattice when stress-free (orange) and when stretched with tensile prestress (blue). (d) Eigenvalues of the dynamical matrix of a mechanical network (right). When prestress on the network increase beyond a threshold, one normal mode (e) becomes unstable.	85
5.3	Examples of SSSs in prestressed systems. Red and blue arrows denote t^{\parallel}, t^{\perp} respectively. (a) SSS of a stress-free mechanical network. The two mechanical frames are shown as (a) the four grey sites connected by dotted lines as bonds to form a 2D frame; (g) the six grey sites connected in 3D to form a tensegrity T3 prism. When only considering \parallel directions, there is one SSS for the 2D frame, which is the single SSS shown in (a). After taking \perp directions into account, there are six SSSs for the 2D frame in total, which are shown from (a)-(f). With a tensegrity T3 prism structure, (g) indicates the single SSS when only considering \parallel directions. There are 21 SSSs in total when considering \perp directions, including (g)(h) shown as examples.	93
5.4	Vibrational modes of prestressed triangular lattices. (a) a site-localized SSS $ t_{\ell}\rangle$ on a triangular lattice, where bonds surrounding the hexagon carry tension, and bonds in the hexagon carry compression. The red disk on the center site represent the strength of this SSS. (b) A prestressed triangular lattice with the prestress generated using a linear combination of site-localized SSSs with independent coefficients on each site. (c) A triangular lattice with positional disorder. (d-f) Dynamical matrix eigenvalue analysis of 32×32 triangular lattices under periodic boundary condition with prestress (d-e) or positional disorder (f). (d) Lowest 300 eigenvalues λ of the dynamical matrix of prestressed triangular lattices in ascending order, at $\tilde{c} = 0$ (blue), $\tilde{c} = 0.1$ (orange), $\tilde{c} = 0.2$ (green), from top to bottom. (e) The lowest eigenvalue λ_{min} as a function of \tilde{c} . (f) Lowest 300 eigenvalues λ of the dynamical matrix of triangular lattices with positional disorder, at $\tilde{u} = 0$ (blue), $\tilde{u} = 0.1$ (orange), $\tilde{u} = 0.2$ (green), from top to bottom. (g) Phonon dispersion relation of the lowest band of triangular lattices with no prestress (yellow, upper), and critical compressive prestress (blue, lower) where modes along ΓM approach instability.	97

5.5	<p>Prestressed triangular lattice under load. A triangular lattice with disordered prestress ($\bar{c} = 0$, $\tilde{c} = 0.12$ and all modes stable) in (a) responds to simple shear σ_{xy}, with longitudinal $t^{\parallel}\rangle$ and transverse $t^{\perp}\rangle$ forces shown in (b,c). Red and green denote compression and tension in (b). Orange and cyan denote clockwise and counter clockwise in (c). Note the stress shown in (b,c) is in addition to the prestress in (a). At different \bar{c} and \tilde{c} (d), the lattice exhibit shear modulus shown in (e). (f-i) longitudinal and transverse responses to longitudinal (f,g) and transverse (h,i) force dipoles (black arrows show directions of forces). (j,k) Stiffness against longitudinal and transverse dipoles.</p>	98
5.6	<p>(a) Prestress visualization of colloidal glass systems. The system size is $N = 10976$ with preparation cooling rate $\Gamma = 5 \times 10^{-6} \epsilon / (k_B \tau_0)$. (b) Initial bond tension distribution for the configuration shown in (a).</p>	102
5.7	<p>Actual tension increment compared to the tension increment prediction from pre-stressed elasticity and stress-free elasticity. (a) Cooling rate $\Gamma = 5 \times 10^{-2} \epsilon / (k_B \tau_0)$ with shear strain 1%, (b) cooling rate $\Gamma = 5 \times 10^{-6} \epsilon / (k_B \tau_0)$ with shear strain 0.01%. The system size is $N = 10976$ in both (a) and (b). (c) Clustering tendency index H averaged over two different samples with stress-free and pre-stressed elasticity compared to the actual H. The actual tension response is measured with shear strain 1% with system size $N = 10976$ and preparation cooling rate $\Gamma = 5 \times 10^{-6} \epsilon / (k_B \tau_0)$. The red dashed line indicates the threshold to determine whether or not the tension change is clustered. . . .</p>	104
5.8	<p>(a) Linear response of tension increment with and without considering prestress in the system. The pre-stressed tension increment are the tension increment along longitudinal directions; (b) Comparison to actual tension increment including transverse directions. Note: Here the actual tension increment response is from 0.01% strain compared to the initial configuration, and the system size is $N = 10976$, $\Gamma = 5 \times 10^{-6} \epsilon / (k_B \tau_0)$. (c) Shear modulus G from stress-free response and pre-stressed response compared to actual G. Note: Here the actual G is measured from 1% shear strain to the initial configuration, and the system size is $N = 10976$ with preparation cooling rate $\Gamma = 5 \times 10^{-6} \epsilon / (k_B \tau_0)$. G is averaged over three different samples for each data point.</p>	105
5.9	<p>(a) Number of SSSs (N_{SSS}), (b) number of bonds (N_b), (c) measured shear modulus (G), (d) averaged normal stress (P) for different cooling rates Γ. Those quantities are averaged over 5 different configurations for each cooling rate, and the system size is $N = 10976$.)</p>	108
5.10	<p>(a) Tension responses of a \perp force dipole applied on the highlighted bond with black color. The 2-D color scheme contains t_{\parallel} indicating tension/compression in bonds and t_{\perp}/t indicating the rotational responses. (b) gives a zoomed-in view to the dipole force response in (a). The visualized sample configuration has system size $N = 2916$ with preparation cooling rate $\Gamma = 5 \times 10^{-6} \epsilon / (k_B \tau_0)$. (c) Distribution of minimum κ for systems with different preparation protocols. System size: $N = 2916$; The histogram is averaged over 10 different samples for each preparation cooling rate.</p>	109

LIST OF ABBREVIATIONS

ZM Zero Mode

SSS State of Self Stress

RP Rigidity Percolation

MD Molecular Dynamics

BOP Bond Orientational Order Parameter

SG Sierpiński Gasket

SGL Sierpiński Gasket Lattice

TPL Triangle Plate Lattice

ST Sierpiński Tetrahedron

PBC Periodic Boundary Condition

SVD Singular Value Decomposition

ABSTRACT

Isostatic mechanical structures, where numbers of constraints arising from physical interactions balance the number of internal degrees of freedom, are on the verge of mechanical instability. Isostatic structures exhibit fascinating phenomena, showing criticality in mechanical responses and other properties. Such critical mechanical structures, including jamming, *Rigidity Percolation* (RP) and Maxwell lattices, have been widely explored. In those structures, the emergence of rigidity is controlled by the isostatic point and the density is moderately high.

This dissertation focuses on critical mechanical phenomena when the connectivity of the structure is *away from isostaticity*. The study of these systems unravel the complexity of rigidity in a broad range of materials. The first act of this dissertation discusses the emergence of rigidity in ultra-low-density systems with the introduction of positional correlations, including two projects related to correlated rigidity percolation. In addition to low-density solids, high-density solids like glasses exhibit interesting phenomena and different mechanical behaviors compared with isostatic systems. The second act of this dissertation studies high-density glasses and includes a project discussing stressed elasticity in over-isostatic region.

The first project presented in this dissertation concerns RP with structural correlations, an effect ignored in classical theories albeit relevant to many liquid-to-amorphous-solid transitions, such as colloidal gelation, which is introduced by attractive interactions and aggregation. Using a lattice model, we show that structural correlations shift RP to lower volume fractions. Through molecular dynamics simulations, we show that increasing attraction in colloidal gelation lowers the RP transition, and this phenomena agrees with experiments. Hence, the emergence of rigidity at colloidal gelation can be understood as a RP transition, but occurs at volume fractions far below values predicted by the classical RP, due to attractive interactions which induce structural correlation.

Motivated by the experimentally observed fractal nature of materials like colloidal gels and disordered fiber networks, the second project discussed in this dissertation studies RP in a fractal network where intrinsic correlation in particle positions is controlled by fractal iteration. Specifically, we calculate the critical packing fractions of site-diluted lattices of

Sierpiński Gasket (SG)'s with varying degrees of fractal iteration. Our results suggest that although the correlation length exponent and fractal dimension of the RP of these lattices are identical to those of the regular triangular lattice, the critical volume fraction is dramatically lower due to the fractal nature of the network. Furthermore, we develop a simplified model for a SG lattice based on the fragility analysis of a single SG. This simplified model provides an upper bound for the critical packing fractions of the full fractal lattice, and this upper bound is strictly obeyed by the disorder averaged RP threshold of the fractal lattices. Our results characterize rigidity in ultra-low-density fractal networks.

The third project presents a systematic method based on *States of Self-Stress* (SSSs) to investigate how prestress affects elastic response of amorphous solids. Using a triangular lattice model with varying prestress, and also in amorphous configuration of compressed repulsive particles, as a model for a colloidal soft solid, we show how prestress determines the response of glasses to both macroscopic shear strain and local dipole forces, where they display behaviors qualitatively different from un-stressed random networks with the same geometry. We also use this method to study the dependence of the stress-bearing ability of the system on the preparation protocol, which changes the microscopic prestress distribution, as well as signatures of the spatial evolution of stress under strain. The heterogeneity of stress change and mechanical responses are accurately depicted from the SSS calculation when prestress is included. Our results characterize the elasticity for prestressed amorphous solids.

CHAPTER 1

Introduction

1.1 Overview

1.1.1 Maxwell lattices and the isostatic point

In 1864, James Clerk Maxwell published a remarkable paper [3] and took the first systematic study on mechanical stability of frames. In this paper, Maxwell introduced frames as points (referred as *site*) connected by rigid struts (referred as *bond*), and argued that a *stiff* frame, which is defined as ‘*the distance between any two points cannot be altered without altering the length of one or more of the connecting lines of the frame*’, requires that

$$N_b \geq dN - \frac{d(d+1)}{2}, \quad (1.1)$$

where N_b is the number of bonds, N is the number of sites and d is the dimension of the system. The term $\frac{d(d+1)}{2}$ corresponds to the number of translations and rotations under free boundary, sometimes referred as “trivial” zero modes. Equation 1.1 is known as the *Maxwell’s rule*, and plays a fundamental role in understanding the mechanical stability of materials.

The Maxwell’s rule also gives a critical threshold to separate stiff and floppy systems

as

$$z_c^N = 2d - \frac{d(d+1)}{N},$$

where $z \equiv 2N_b/N$ is defined as the average coordination number. Following the Maxwell's rule, when $z > z_c^N$, the system is stiff, and when $z < z_c^N$ the system is not stiff.

z_c^N reduces to $z_c^\infty = 2d$ in the limit of large N , and the term *Maxwell lattice* is commonly used for lattices which have the average coordination number $z = z_c \equiv 2d$.

However, the Maxwell's rule is not a general rule since there could be *redundant* constraints, which are constraints not needed for rigidity [4]. Thus a generalized Maxwell relation is developed and known as the *Maxwell Calladine Index Theorem*:

$$N_0 - N_s = dN - N_b, \tag{1.2}$$

where N_0 is the number of *Zero Mode* (ZM), corresponding to the set of site displacements that produce no changes in bond lengths, and N_s is the number of *State of Self Stress* (SSS), corresponding to the set of tensions that produce no forces at any site.

N_0 includes the counting for "trivial" ZMs from rigid translations and rotations, and there are $\frac{d(d+1)}{2}$ trivial ZMs. Any other ZMs involving internal displacements of sites are called *floppy modes*. The number of floppy modes are

$$\begin{aligned} M &= N_0 - \frac{d(d+1)}{2} \\ &= dN - N_b + N_s - \frac{d(d+1)}{2}, \end{aligned}$$

from the Maxwell Calladine index theorem. Those internal ZMs are usually called as floppy modes in the physics literature [5] and *mechanisms* in the engineering literature [4]. From the concept of floppy modes, one can have a more rigorous way of defining "rigid"

(or stiff) compared to the Maxwell's rule: *a system is rigid if it has no floppy modes.*¹ This rule of determining rigidity takes care of redundant constraints which the Maxwell's rule does not.

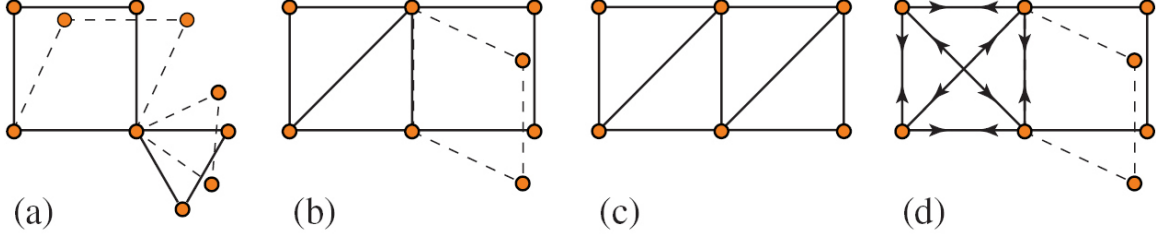


Figure 1.1: Frames of bonds connecting $N = 6$ sites. (a) has 6 sites, 7 bonds, 5 ZMs and two floppy modes indicated by the dotted bonds. (b) has 6 sites, 8 bonds, 4 ZMs and one floppy mode. (c) and (d) are constructed from (b) by adding an additional diagonal bond. (c) satisfies the Maxwell's rule with only the three trivial ZMs. (d) has 4 ZMs and one SSS indicated by the arrows on the bonds in the left square.

Now let's look at a few examples of frames with some of them satisfying the Maxwell's rule in Fig. 1.1 [6], to illustrate the relationship between the Maxwell's rule and the Maxwell Calladine index theorem. Fig. 1.1(a) gives a simple example of the Maxwell Calladine index theorem. There are $N = 6$ sites, and $N_b = 7$ bonds in the frame. There are no SSSs in the frame ($N_s = 0$) so the number of ZMs is $N_0 = dN - N_b = 5$. Removing the 3 trivial ZMs, there are 2 floppy modes in such system, which are indicated by the dotted bonds. In Fig. 1.1(b), there is one additional bond compared to the frame in Fig. 1.1(a) and there are no SSSs either. As a result, the number of ZMs in such system is one fewer than the system in (a), and this decrease of ZMs reflects a number decrease in floppy modes. Fig. 1.1(c) and (d) are obtained from adding additional bond to the frame in (b). However, the bond added in frame (d) is redundant, which doesn't take away ZMs and provides a SSS instead, while the added bond in frame (c) is not. When considering the Maxwell's rule, the frames in (c) and (d) both follow the rule that $N_b \geq dN - \frac{d(d+1)}{2}$. While in the case of frame (d), the whole system is not rigid since one can find a floppy mode indicated by the dotted bonds

¹Note that this is one way of defining rigidity. One can also define rigidity as the capability of carrying load (SSSs).

in Fig. 1.1(d). From the examples shown above, we can see that the Maxwell's rule does not apply for all frames when determining rigidity. A more rigorous way of determining rigidity is to follow the count of Calladine index theorem and see if there are no floppy modes.

From the Maxwell Calladine index theorem, a system with neither any floppy modes ($M = 0$) nor any SSSs ($N_s = 0$) is defined as *isostatic*. Maxwell frames ($z = 2d$) with no SSSs are thus called *isostatic* frames. Such isostatic systems necessarily satisfy the relation $z = z_c$, but for systems with $z = z_c$, they could have finite number of SSSs then the system is not isostatic.

The above definition of isostaticity is unambiguous for finite free boundary systems, since it takes into account of trivial ZMs in such boundary condition when counting floppy modes. However, there is a problem with the same way of defining isostaticity under Periodic Boundary Conditions (PBCs) [7]. The lattice must have at least $d(d + 1)/2$ SSSs in order to be elastically stable. Reference [6] proposes calling systems under PBCs as *isostatic* if $N_0 = d$ and $1 \leq N_s \leq d(d + 1)/2$ and uniquely calling periodic lattices as *isostatic lattices* when $N_0 = N_s = d$.

1.1.2 Physics near isostaticity

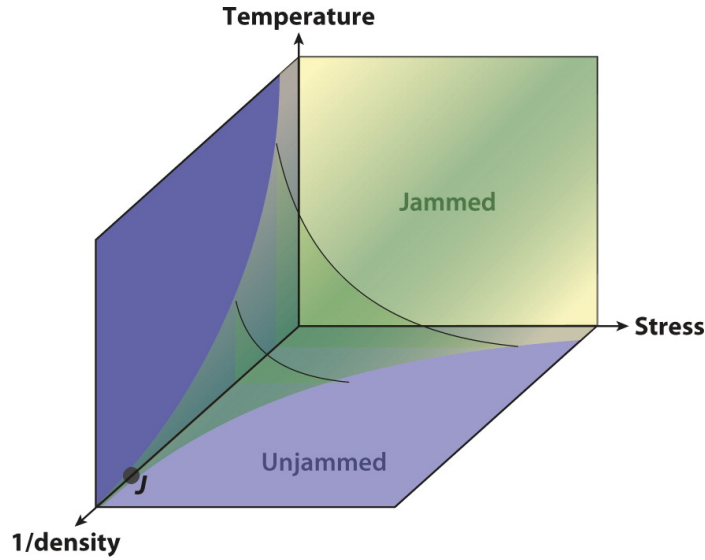
The isostatic point, defined as the critical point where the system is isostatic, is on the verge of mechanical instability, and it is critical to understand systems as diverse as engineering structures [8, 9], diluted lattices near RP [1, 2, 10–13], jammed systems [14–21], biopolymer networks [22–29] and network glasses [30, 31]. In this section, we will briefly review several typical isostatic systems and discuss their behaviors.

1.1.2.1 Emergence of rigidity

Rigidity Percolation (RP) - RP describes the emergence of rigidity in central-force networks, which could be generic lattices or disordered systems. Such rigidity transition oc-

occurs at the marginal condition where the equality of the Maxwell's rule holds [2], as a result of locating near the isostaticity. More details about RP will be discussed in Section 1.2.

Jamming - Starting from the simplest model: frictionless spheres interacting via repulsive finite-range forces at zero temperature, Liu and Nagel proposed a remarkable phase diagram describing the rigidity transition known as the Jamming transition [14].




 Liu J, Nagel R. 2010. Annu. Rev. Condens. Matter Phys. 1:347 – 69

Figure 1.2: Jamming phase diagram. Outside the shaded green region, at high temperature T , applied shear stress Σ , and high inverse density $1/\phi$, the system is unjammed and can flow; inside the shaded green region, the system is jammed. The lines in the $(T - 1/\phi)$ and $(1/\phi - \Sigma)$ planes represent the generic dynamical glass transition and yield stress, respectively. The point “ J ” marks the jamming transition for ideal spheres at zero temperature and applied stress.

In the context of the jamming diagram as shown in Fig. 1.2, the jamming transition is controlled by three parameters: temperature, density and stress. Point J in the jamming diagram, defined as the jamming transition point for ideal spheres at zero temperature and zero applied stress, is a special transition point with aspects of both first- and second-order phase transitions. The order parameter that characterizes the jamming transition is $z \equiv 2N_b/N$, the average coordination number. At low packing density $\phi < \phi_c$, $z = 0$

since particles are not forced to be in contact. z jumps discontinuously from $z = 0$ to the non-zero value z_c at the jamming transition packing fraction ϕ_c . Interestingly, it turns out that Point J ($\phi = \phi_c$), which describes the minimal rigidity for mechanical stability in jamming transition, is at the isostatic point ($z_c = 2d$) [18]. When the system is compressed to packing fraction above the transition point, a scaling relation is verified as [32]

$$(z - z_c) \sim (\phi - \phi_c)^{\beta \approx 1/2},$$

implying a diverging length scale near isostaticity. This brings us the insight that even for systems as complex as jammed solids, isostaticity is a great indicator for mechanical stability.

1.1.2.2 Elasticity and topological mechanics

Both RP and jamming study the emergence of rigidity in disordered systems, and show criticality at the isostatic point. In the meantime, there are profound results of the elastic and dynamical properties at or near isostaticity [6] and some of those studies excite an emergent field: *topological mechanics*, where concepts of electronic topological states of matter are applied to mechanical systems [33, 34].

Topological Mechanics of Maxwell Lattices - In 2014, Kane and Lubensky published a landmark paper connecting the topological mechanical modes and the topological band theory of electronic systems in isostatic lattices, and proposed a topological invariant to identify distinct topological states [33]. Owing to the criticality of isostaticity, any Maxwell lattice has at least $d(d-1)/2$ homogeneous soft deformations, so called Guest-Hutchinson floppy modes, and these homogeneous soft deformations provide a tool to change the lattice geometry and thus are able to induce transitions between different topological states [34]. Examples of topological Maxwell lattices include 1-D mechanical Su-Schrieffer-Heeger model and 2-D deformed Kagome lattices. The manipulability of these topological me-

chanical states opens the way to the creation of metamaterials that display designable and reliable behaviors.

1.1.2.3 Examples of isostatic systems

Here we introduce some typical examples of 2-D isostatic or near-isostatic systems in Fig. 1.3.

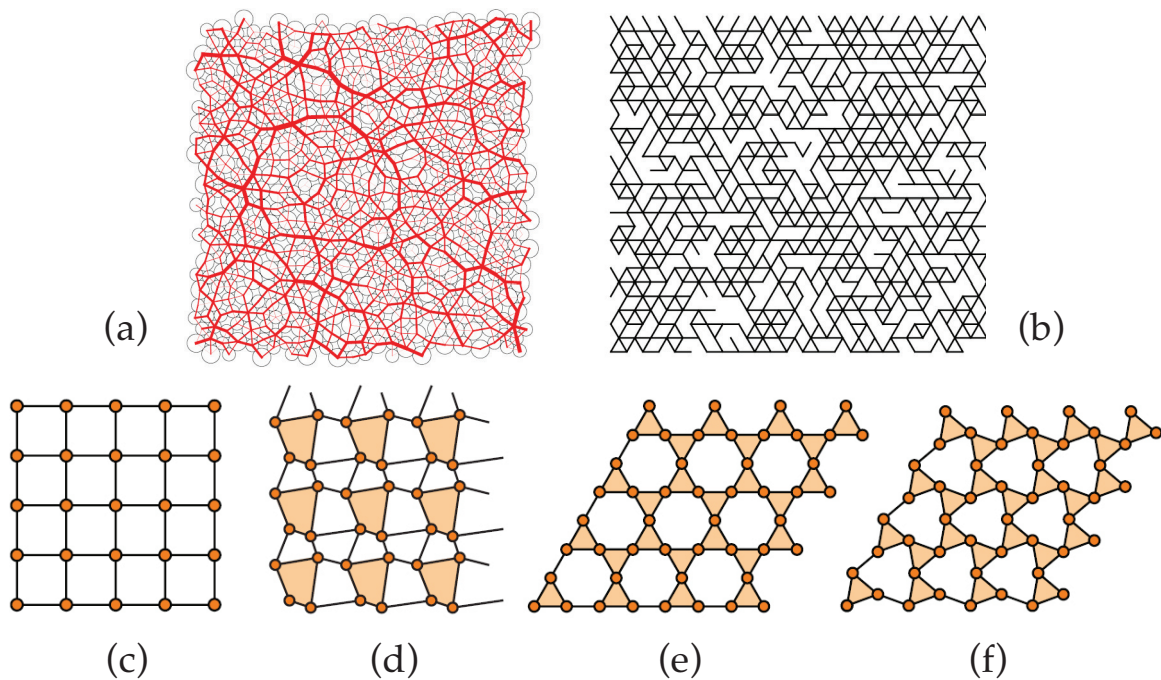


Figure 1.3: (a) Packed bi-disperse discs just above the jamming transition. The dark red lines are chains of force that are a response to the pressure required to pack the particles at $z > z_c$. (b) A representative bond-diluted lattice near the rigidity percolation threshold of $z_c \approx 3.96$. (c) Square, (d) distorted square, (e) kagome lattice and (f) twisted kagome lattice.

Fig. 1.3 (a) and (b) are disordered systems close to the isostatic point. Those systems representatively show examples of the emergence of rigidity for amorphous solids. Fig. 1.3 (c-f) are examples of isostatic lattices, which have special elasticity due to their criticality and some of them could be tuned for different topological mechanical states.

1.1.3 Rigidity beyond isostaticity

Isostatic systems are interesting due to their criticality, elasticity and manipulability. Looking at the examples of Fig. 1.3 (a) and (b), the packing fractions for reaching such isostaticity are rather moderate. The critical density for jamming threshold is $\phi_J \approx 0.84$ for 2-D bi-disperse packings and $\phi_J \approx 0.64$ for 3-D mono-disperse spheres. The bond RP threshold for 2-D generic triangular lattice is $p_c \approx 0.66$ and the site RP threshold for such system is $p_c \approx 0.70$. In this section, we will introduce systems of both much lower density and higher density than the isostatic systems which we just went over. Interestingly, lower density systems can still have rigidity even much sparser than jammed packings or RP. High density systems also have rich elasticity which is worth paying attention to. Those behaviors are all untypical to the isostaticity we just talk about, so we will look at those special isostaticity and systems beyond isostaticity in both low and high densities for the following discussion.

1.1.3.1 Low density solids

Shear Jamming - The jamming transition has the threshold of $\phi_J \approx 0.84$ for 2-D bi-disperse packings and $\phi_J \approx 0.64$ for 3-D mono-disperse spheres, however, jamming of frictional, disk-shaped particles can be induced by applying shear stress at densities lower than the critical value ϕ_J [35].

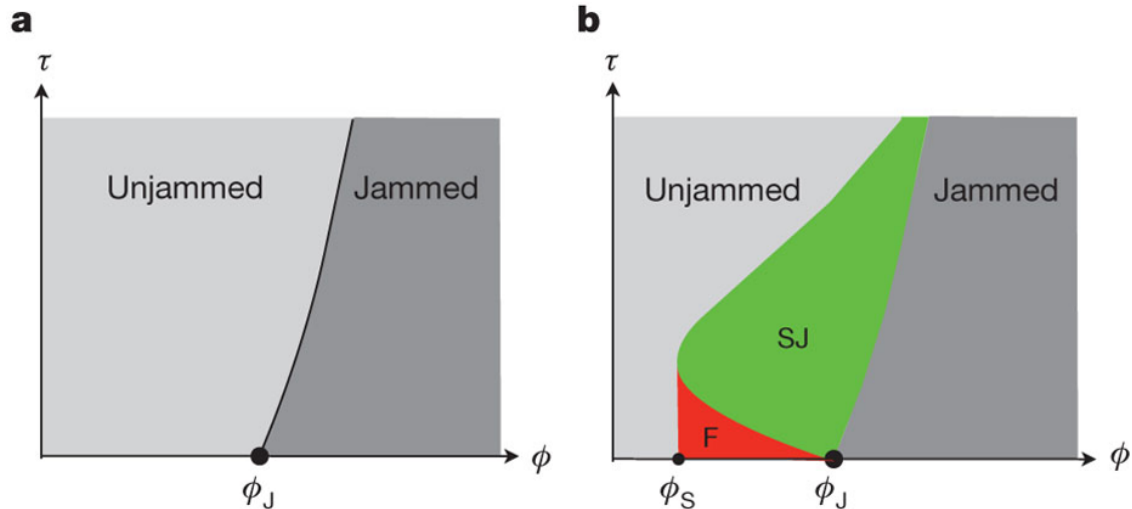


Figure 1.4: (a) Original jamming phase diagram and (b) generalized jamming phase diagram with shear jamming in the $T = 0$ plane.

Fig. 1.4(b) is a generalized jamming phase diagram proposed by Bi and coworkers in 2011 [35], including the shear-jammed (SJ) and fragile (F) states. Along the density axis ϕ , two special densities exist: ϕ_S , below which there is no shear jamming, and ϕ_J , above which isotropically jammed states exist (point J). For $\phi_S \leq \phi \leq \phi_J$, jamming can occur with application of shear stress.

Since the SJ region has the density below point J , we can see that while frictionless spheres at jamming are isostatic, frictional spheres at jamming (unjammed to SJ transition) are not. This violation of isostaticity for the emergence of rigidity in shear-jammed system is due to the fact that besides of the constraints of normal motions between connected sites, a frictional packing needs to satisfy one additional group of constraints: the sliding motion when there is static friction in between particles. As a result, even a smaller coordination number $z < 2d$ can provide enough constraints for the system to reach minimal rigidity.

For a packing of N interacting particles, there are Nd force balance equations and $d(d-1)N/2$ torque balance equations, and the number of contacts is $zN/2$. If we treat these tangential forces as independent new degrees of freedom in the constraint counting, the threshold for having a stable packing is $z_c^t = d + 1$. In the case that not all of the

tangential forces provide the degrees of freedom for torque balance, one can expect *any* z in the range of $z_c^u \equiv d + 1 \leq z \leq z_c$. To resolve the conundrum compared to the original definition of isostaticity, a criterion called *generalized isostaticity* was introduced as [36, 37],

$$z_c^m = (d + 1) + \frac{2n_m}{d},$$

where n_m is the mean number of fully mobilized contacts per particle and z_c^m is the generalized isostaticity criterion. This equation describes a line of transition points in 2-D system interpolating from $z = d + 1$ at $n_m = 0$, corresponding to the limit of $\mu = \infty$ where μ is the friction coefficient, to $z_c = 2d$ at $n_m = 1$, corresponding to the limit of $\mu = 0$ [36].

Along the route of recounting contact constraints to extend frictional jamming from frictionless jamming, RP can also be extended to frictional RP by generalizing the rigid cluster decomposition algorithm [37–39], and the frictional RP threshold approaches to the general isostaticity counting z_c^m instead of the original isostaticity counting rule z_c , which goes below the isostatic point.

Colloidal Gels - Another interesting phenomenon I want to bring up is colloidal gels, disordered arrested states of matter at very low packing fraction ϕ , which do not flow but behave solid-like mechanical properties such as a yield stress. One important nature which leads to the gel transition is the short-range interaction in colloidal systems, and multiple routes to the gel state have been proposed and critically examined [40]. Fig. 1.5 gives the 3D reconstruction of a colloidal gel sample, with the inset as 2D confocal microscope image [41]. This gel structure is in a very low volume fraction $\phi = 0.045$, far below point J , but still has structural rigidity.

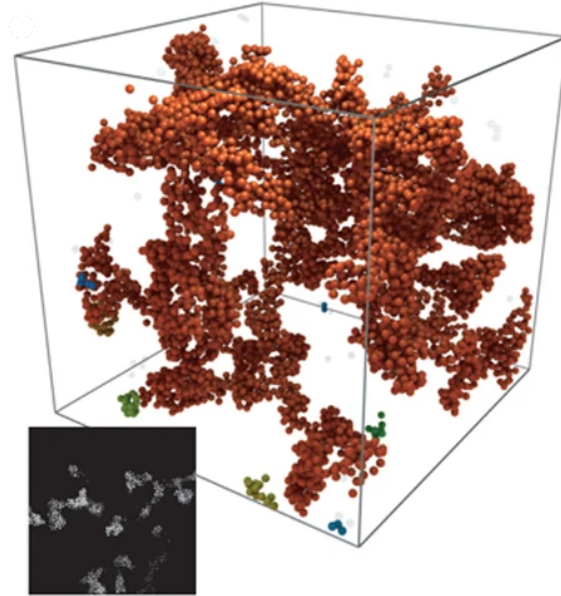


Figure 1.5: A colloidal gel sample with $\phi = 0.045$

In this dissertation, we are not focusing on the transition to gels. Instead, we will try to look at one straightforward but important question: after the formation of gels, how can they obtain solid-like mechanical properties with such low volume fractions? Theoretical models are proposed to dive into such questions and more details will be discussed in Chapter 3 and Chapter 4;

1.1.3.2 High density solids

Glasses - For amorphous solids which have higher volume fractions compared to either point J or RP threshold, their responses to mechanical perturbations are always interesting. Understanding glassy rheology is the key to designing disordered materials and developing predictive models for flow and failure in disordered systems. Such glassy systems are usually above isostaticity and have overconstrained regions, which provide additional structural supports to marginal rigidity. Just like stress plays a role in stabilizing the soft modes of tenuous bonding structures in shear jammed states, stress also takes great impact on the rheology of amorphous solids, especially in over isostatic systems with high volume

fractions. We will discuss those high density solids beyond isostaticity with more details in Chapter 5.

1.2 Rigidity percolation

Rigidity Percolation (RP), as mentioned in Section 1.1.2, is a concept describing the emergence of rigidity in disordered networks. In this section, I will give an overview on RP with its development and phenomena, providing a solid background for the study in Chapter 3 and Chapter 4.

1.2.1 Connectivity percolation

Before diving into RP, let's look at connectivity percolation first. Connectivity is essential for physics of disordered systems. Starting from 1940s, scientists studied the emergence of system-wise connectivity by developing theory of *percolation*, which describes how small molecules react and form very large macromolecules connected by chemical bonds [42, 43]. Later, the field of connectivity percolation rapidly evolves and has been applied to many disciplines in statistical physics and mathematics. In Stauffer's textbook for percolation theory [44], percolation is illustrated as: *Each site of a very large lattice is occupied randomly with probability p , independent of its neighbors. Percolation theory deals with the clusters thus formed, in other words with the groups of neighboring sites.* Connectivity percolation is a geometric type of phase transition, because a critical fraction $1 - p_c$ of removal to the network breaks the macroscopically connected network into significantly smaller connected clusters. The critical threshold p_c and critical phenomena close to p_c for connectivity percolation have been deeply examined [44].

Connectivity percolation studies the connectivity between nodes via bond and uses bond connections as an approach for mechanical behaviors of disordered systems. However, the emergence of rigidity demands more than simple connectivity. Imagine a system

of three nodes connected by two rigid bars, even though all nodes are connected, the whole system is not rigid since the two connecting bars can freely rotate using the center node as a pivot point. Considering such limitations of connectivity percolation in the article of rigidity, a more specified and concrete concept, *Rigidity Percolation* (RP) is introduced.

1.2.2 Phenomena of rigidity percolation

In 1983, Thorpe studied the rigidity in random networks and proposed a picture of rigid regions percolation related to the coordination number [5], so a rigidity transition is characterized. Following this work, Feng and coworkers [10] did numerical simulations to study the central-force RP in lattices and discovered a new universality class for this transition. To further understand the central-force RP, Feng, Thorpe and Garboczi developed an effective-medium theory to describe elastic networks in 1985 [11]. Their results indicate that RP is a continuous phase transition. To study the universality class of RP, the “pebble game” algorithm, which is an efficient algorithm for detecting RP, is proposed and the critical phenomena near the RP threshold is examined [1, 2]. The details of the “pebble game” algorithm will be illustrated in Section. 2.1, and in this section we will focus on looking at the physical phenomena for RP.

The nature of RP is related to connectivity percolation, which is a second-order phase transition and is described by critical exponents for its critical phenomena. Critical exponents, which describe the fractal properties of the percolating medium at large scales close to the transition, are universal in the sense that they only depend on the space dimension and the type of percolation model. Critical exponents of the same universality class do not depend on microscopic details like lattice structures, or whether site or bond percolation is considered. Some typical critical exponents of connectivity percolation, like the fractal dimension and correlation length, can also be characterized in RP with different values. Connectivity percolation describes the percolation of a scalar field - whether two elements are connected, with one degree of freedom. On the other hand, RP describes the percola-

tion of a vector field, which determines the rigidity between two elements by looking at the vector floppy modes, with more degrees of freedom when space dimension $d > 2$. The consequence of this difference is that RP and connectivity percolation belong to different universality classes.

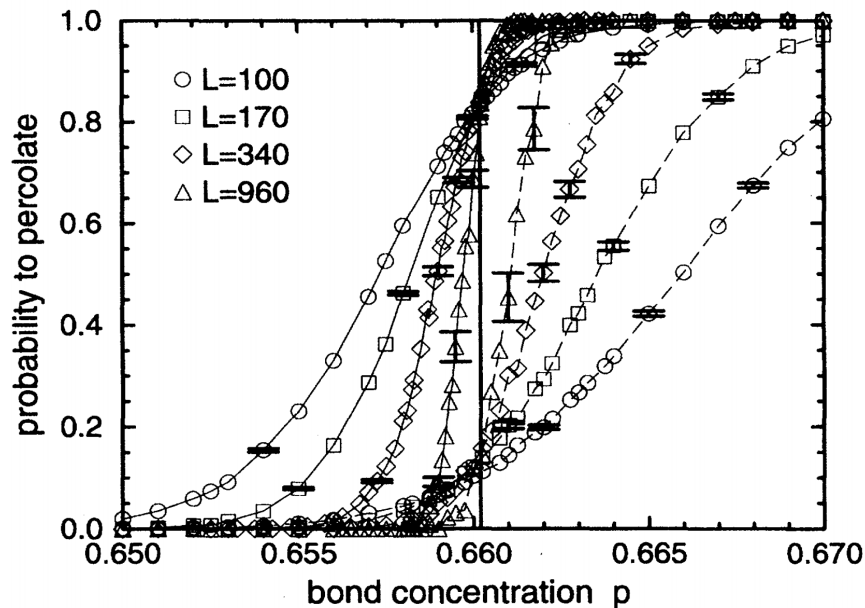


Figure 1.6: The probability for a bond-diluted generic network to have a spanning rigid cluster with respect to bond concentration p . Periodic (free) boundary conditions with various system sizes are shown with solid (dashed) line segments drawn between data points.

RP is studied for random central-force networks on both bond- and site-diluted generic triangular lattices [1]. The critical thresholds for bond and site diluted RP are respectively $p_c = 0.66020 \pm 0.0003$ and $p_c = 0.69755 \pm 0.0003$. The critical threshold p_c can be obtained from the finite size scaling of $|p_c(L) - p_c(L = \infty)| \sim L^{-1/\nu}$ with the exponent ν extracted from the critical fluctuation $\Delta = \sqrt{\langle p_c(L)^2 \rangle - \langle p_c(L) \rangle^2} \sim L^{-1/\nu}$, where $p_c(L)$ is the measured RP threshold with the occurrence of spanning rigid cluster in system size L , and $p_c(L = \infty) = p_c$ is the critical threshold for RP in the generic lattices. The critical exponent ν , is actually the exponent describing the divergence of correlation length ξ when

approaching to the RP transition as

$$\xi \sim |p - p_c|^{-\nu}.$$

The infinite rigid cluster becomes homogeneous at length scales beyond the correlation length ξ ; furthermore, ξ is a measure for the linear extent of the largest finite rigid cluster.

Another important critical exponent to describe RP is the fractal dimension d_f , which describes how the mass of the incipient infinite rigid cluster depends on the linear size of the system as

$$\mathcal{M} \sim L^{d_f}.$$

\mathcal{M} is the mass (number of sites) of the spanning rigid cluster at RP transition point, and L is the system linear size.

Critical exponents are essential features to describe the scale invariance properties near the transition point, so those exponents also indicate that for generic triangular lattices, RP is a second-order phase transition. The measured exponents are $\nu = 1.21 \pm 0.06$ and $d_f = 1.86 \pm 0.02$, compared with the different universality class of connectivity percolation with $\nu = 1.896$ and $d_f = 1.333$ on same lattices.

1.3 Linear elasticity in discrete models

For the previous discussions about isostaticity and beyond, mechanical properties of disordered systems are described by constraints and degrees of freedom counting, with the underlying assumption than the building blocks of such systems, like repulsive spheres in jammed systems, are considered discretely connected by bonds as the constraints. Discrete models are good approximant for soft matter systems. In this section, we will discuss the linear response of one simplest discrete model - the spring-mass model, which describes a

mechanical frame consisting of N point masses connected by N_b central-force springs in d dimensions.

1.3.1 The equilibrium matrix and the compatibility matrix

The linear response of an elastic network with N point masses connected by N_b central-force springs in d dimensions can be fully described by the equilibrium matrix \mathbb{Q} and the compatibility matrix \mathbb{C} as

$$\mathbb{Q} \cdot |t\rangle = |f\rangle,$$

where $|t\rangle$ represents the tensions on each bond, which is a N_b dimensional vector; $|f\rangle$ represents the forces on each site, which is a $N \cdot d$ dimensional vector. As a result, the equilibrium matrix \mathbb{Q} has the dimension $Nd \times N_b$.

As for the compatibility matrix \mathbb{C} ,

$$\mathbb{C} \cdot |u\rangle = |e\rangle,$$

where $|u\rangle$ represents the displacements of each site, which is a $N \cdot d$ dimensional vector; $|e\rangle$ represents the extensions of each bond, which is a N_b dimensional vector. As a result, the compatibility matrix \mathbb{C} has the dimension $N_b \times Nd$.

The compatibility matrix \mathbb{C} is constructed from the bond elongation relations as:

$$e_{\langle ij \rangle} = \hat{b}_{\langle ij \rangle} \cdot (\vec{u}_i - \vec{u}_j), \quad (1.3)$$

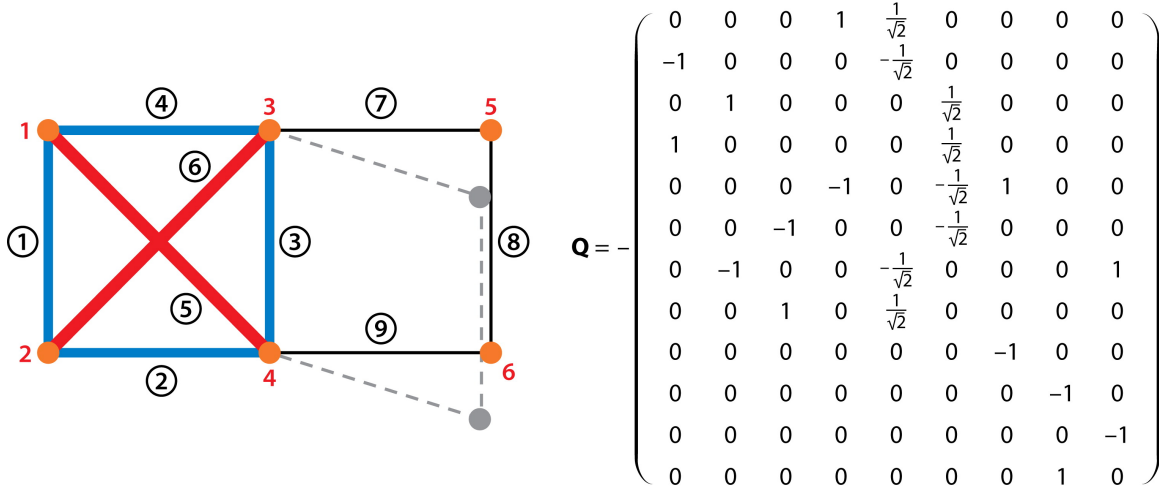
with $\hat{b}_{\langle ij \rangle}$ as the unit vector pointing from site j to site i , \vec{u}_i as the displacement vector for

site i . And the equilibrium matrix \mathbb{Q} is constructed from the site force equations as

$$\vec{f}_i = \sum_{\beta} \text{sign}(\beta) \vec{t}_{\beta}, \quad (1.4)$$

with β as the bond site i shares with its neighbors and $\text{sign}(\beta) = +1(-1)$ if the direction of bond β points away from (toward) site i . If we choose the direction of bond β as $\hat{b}_{\langle ij \rangle}$, which points from site j to site i , then $\vec{f}_i = - \sum_{\langle ij \rangle} \vec{t}_{\langle ij \rangle}$ where $\mathcal{N}(i)$ is the set of all neighbors for site i .

Let's go with an instructive example to carry out the explicit calculation of \mathbb{Q} and \mathbb{C} for a simple frame from the review paper by Mao and Lubensky [34]. It is also straightforward to see from this example that the compatibility matrix and equilibrium matrix are transposes of each other $\mathbb{C} = \mathbb{Q}^T$.




 Mao X, Lubensky TC. 2018. *Annu. Rev. Condens. Matter Phys.* 9:413–33

Figure 1.7: A frame of six sites (red numbers) and nine springs (circled black numbers) and its 12×9 equilibrium matrix \mathbb{Q} with rows ordered according to the sites degrees of freedom, $\{x_1, y_1, x_2, y_2, \dots, x_6, y_6\}$, and columns ordered according to the springs.

We consider the frame shown in Fig. 1.7 with $N = 6$ and $N_b = 9$ on 2D plane $d = 2$. The figure labels sites ($s = 1, \dots, 6$) and bonds ($\beta = \textcircled{1}, \dots, \textcircled{9}$). The displacement-

elongation equations are

$$\begin{aligned}
e_{\textcircled{1}} &= \hat{b}_{\langle 12 \rangle} \cdot (\vec{u}_1 - \vec{u}_2), & e_{\textcircled{2}} &= \hat{b}_{\langle 24 \rangle} \cdot (\vec{u}_2 - \vec{u}_4), & e_{\textcircled{3}} &= \hat{b}_{\langle 34 \rangle} \cdot (\vec{u}_3 - \vec{u}_4) \\
e_{\textcircled{4}} &= \hat{b}_{\langle 13 \rangle} \cdot (\vec{u}_1 - \vec{u}_3), & e_{\textcircled{5}} &= \hat{b}_{\langle 14 \rangle} \cdot (\vec{u}_1 - \vec{u}_4), & e_{\textcircled{6}} &= \hat{b}_{\langle 23 \rangle} \cdot (\vec{u}_2 - \vec{u}_3) \\
e_{\textcircled{7}} &= \hat{b}_{\langle 35 \rangle} \cdot (\vec{u}_3 - \vec{u}_5), & e_{\textcircled{8}} &= \hat{b}_{\langle 56 \rangle} \cdot (\vec{u}_5 - \vec{u}_6), & e_{\textcircled{9}} &= \hat{b}_{\langle 46 \rangle} \cdot (\vec{u}_4 - \vec{u}_6),
\end{aligned}$$

and the vector forces equations are

$$\begin{aligned}
\vec{f}_1 &= -\vec{t}_{\langle 12 \rangle} - \vec{t}_{\langle 13 \rangle} - \vec{t}_{\langle 14 \rangle}, & \vec{f}_2 &= \vec{t}_{\langle 12 \rangle} - \vec{t}_{\langle 23 \rangle} - \vec{t}_{\langle 24 \rangle} \\
\vec{f}_3 &= \vec{t}_{\langle 13 \rangle} + \vec{t}_{\langle 23 \rangle} - \vec{t}_{\langle 34 \rangle}, & \vec{f}_4 &= \vec{t}_{\langle 14 \rangle} + \vec{t}_{\langle 24 \rangle} + \vec{t}_{\langle 34 \rangle} \\
\vec{f}_5 &= \vec{t}_{\langle 35 \rangle} - \vec{t}_{\langle 56 \rangle}, & \vec{f}_6 &= \vec{t}_{\langle 46 \rangle} + \vec{t}_{\langle 56 \rangle}.
\end{aligned}$$

One needs to note that it is arbitrary to choose the bond direction \hat{b}_β as $\hat{b}_{\langle ij \rangle}$ or $\hat{b}_{\langle ji \rangle}$, as long as following the sign conventions in Eq. 1.3 and Eq. 1.4. Those two equations also lock the positive convention for $|e\rangle$ as bond elongations instead of bond shrinking.

The matrix \mathbb{Q} for the frame thus constructed is shown in Fig. 1.7 as well. The matrix \mathbb{C} constructed following the above formulations is the transpose of \mathbb{Q} .

1.3.2 States of self-stress (SSS) and zero modes (ZM)

The null space of \mathbb{Q} is the set of tensions, defined as SSSs in the Maxwell Calladine index theorem from Eq. 1.2, that produce no forces at any site.

$$0 = \mathbb{Q} \cdot |t_{\text{SSS}}\rangle$$

The null space of \mathbb{C} is the set of site displacements, defined as ZMs in the Maxwell

Calladine index theorem from Eq. 1.2, that produce no changes in bond lengths.

$$0 = \mathbb{C} \cdot |u_{ZM}\rangle$$

Now let's look back to the example frame in Fig. 1.7. Solving for the null space of \mathbb{Q} gives the SSS of the system, that the frame contains one SSS with

$$|t_{SSS}^1\rangle = \left\{ -\frac{1}{\sqrt{2}}, -\frac{1}{\sqrt{2}}, -\frac{1}{\sqrt{2}}, -\frac{1}{\sqrt{2}}, 1, 1, 0, 0, 0 \right\};$$

This SSS is shown in Fig. 1.7 with the way that blue bonds are under tension with magnitude proportional to line thickness, and red bonds are under compression. The null space of \mathbb{C} contains four ZMs, including three trivial translations and rotations and one nontrivial floppy mode (springs shown as dashed gray lines and sites as solid gray dots in Fig. 1.7).

1.3.3 The dynamical matrix

The dynamical matrix \mathbb{D} is defined as the Hessian given by the second derivative of elastic energy with respect to particle displacements as

$$\delta V = \frac{1}{2} \langle u | \mathbb{D} | u \rangle$$

The elastic energy can be written from summing up the energy of all single springs $\langle ij \rangle$ as

$$\begin{aligned} \delta V &= \sum_i \frac{k_{\langle ij \rangle}}{2} e_{\langle ij \rangle}^2 \\ &= \sum_i \frac{k_{\langle ij \rangle}}{2} \left(\sum_j \mathbb{C}_{\langle ij \rangle, j} u_j \right)^2 \\ &= \frac{1}{2} \langle u | \mathbb{C}^T \cdot \mathbb{K} \cdot \mathbb{C} | u \rangle \end{aligned}$$

As a result, one can have the dynamical matrix as

$$\mathbb{D} = \mathbb{C}^T \mathbb{K} \mathbb{C} = \mathbb{Q} \mathbb{K} \mathbb{Q}^T$$

where \mathbb{K} is the diagonal matrix of spring constants of all the springs in system.

1.4 Outline

The remainder of this dissertation focuses on two primary parts: 1) emergence of rigidity in low-density amorphous solids; 2) elasticity in high-density glasses. It is organized as follows.

Chapter 2 gives significant details of numerical techniques used for the study in later chapters. The purpose of this chapter is to make the results in later chapters reproducible and share precise numerical protocols for related study.

Chapter 3 discusses rigidity percolation with structural correlations. We use two models - the correlated lattice model and the attractive gel model to study the effect of correlation on rigidity. In both of those two models, the RP transition threshold is shifted to lower density with the increasing of structural correlations, and we are able to show in the lattice model that the introduction of positional correlation doesn't change the critical exponents thus it is an irrelevant perturbation to RP in general. This chapter is based on the published work in Physical Review Letters by Zhang *et al.* [45].

Chapter 4 studies rigidity percolation in a fractal network, where intrinsic correlations in particle positions are controlled by the fractal iteration. Specifically, we calculate the critical packing fractions of site-diluted lattices of *Sierpiński Gasket* (SG)'s with varying degrees of fractal iteration. Our results suggest that although the critical exponents of the RP of these lattices are identical to that of the regular triangular lattice, the critical volume fraction is dramatically lower due to the fractal nature of the network. Furthermore, we develop a simplified model based on the fragility analysis of a single SG, and this simplified

model provides an upper bound for the critical packing fractions of the full fractal lattice. Our results characterize rigidity in ultra-low-density fractal networks. This chapter is based on the published work in Physical Review E by Machlus *et al.* [46].

Chapter 5 presents a systematic method based on states of self-stress to investigate how prestress affects elastic response of amorphous solids, especially in high-density disordered systems. Using simulated colloidal glasses, we show how prestress determines the response of the glass to both macroscopic shear strain and local dipole forces, where they display qualitatively different behaviors from un-stressed random networks with the same geometry. This chapter is based on the work in manuscript by Zhang *et al.*.

Finally in Chapter 6, I will make a summary of the results presented. To conclude, I will end up with a discussion on future directions of rigidity and elasticity in low-density/high-density mechanical systems.

CHAPTER 2

General Computational Techniques

This chapter provides significant details of those numerical methods I used throughout this dissertation. The purpose of such chapter is to make results in this dissertation as reproducible as possible, and also to share the efforts and non-trivial techniques to pave the way for related study. The main sections in this chapter include the numerical details of the “pebble-game” algorithm, which is used to identify rigidity percolation properties, and the matrix-related calculations of *Zero Mode* (ZM) and *State of Self Stress* (SSS) in discrete networks.

2.1 The “pebble game” algorithm

To identify *Rigidity Percolation* (RP), there is a purely combinatorial algorithm called the *pebble game* algorithm [47], which allows for efficient ways of calculating the number of internal degrees of freedom, identifying all rigid clusters and locating overconstrained regions in 2D generic bar-joint networks. The crux of this algorithm is based on a theorem by Laman [48] from graph theory followed as:

Theorem: A generic network in two dimensions with N sites and B bonds (defining a graph) does not have a redundant bond if no subset of the network containing n sites and b bonds (defining a subgraph) violated $b \leq 2n - 3$.

To identify graph rigidity for a network, one has to apply the Laman condition recursively on all possible subgraphs, which is computational costly. In order to identify RP,

one also needs to build or dilute the network unit by unit (the unit can be bond or site), and perform rigid cluster decomposition for each step of the new generated configuration. This will lead to an extreme increase of the computational cost.

However, because of the recursion of checking all subgraphs, only the subgraphs that contain the newly added bond need to be checked. If each of these subgraphs satisfies the Laman condition $b \leq 2n - 3$, the last bond placed is independent; otherwise it is redundant. This trick can reduce the cost a bit when building or diluting the network to study its RP, and then the *pebble game* algorithm is introduced to solve for such problem efficiently.

A very nice feature for the *pebble game* algorithm is that it is directly correspondent to a physical picture: A free pebble at a site represents an independent motion (degree of freedom), and each free site has d pebbles as its translational degrees of freedom, where $d = 2$ is the dimension for most of the cases in this dissertation. A bond placed between free sites introduces an independent constraint which consumes a pebble (or say, constrains a degree of freedom), then this bond is covered with a pebble. Once a bond is covered by a pebble, it must remain covered as pebbles are rearranged throughout the entire graph. Such requirements in the movement of pebbles give the property that a rigid cluster cannot have more than three free pebbles. The three free pebbles physically correspond to the three degrees of freedom required to specify the position of a rigid body in two dimensions.

2.1.1 The pebble search

The pebble search is key part of the *pebble game* algorithm, which sets a couple of graph search rules according to the Laman condition to search for graph rigidity.

The information of the network connectivity is stored in the graph G , which could be an undirected graph if one only cares about the network configuration. However, the graph G in the *pebble game* algorithm is a **directed** graph, with the graph direction information indicating the arrangement of pebbles in the configuration. An edge is included in the graph when there is a pebble covering the bond, and the direction of that edge is marked as

pointing from the site which gives the pebble for covering that bond.

Here are some details of methods for the pebble search:

- `Find_Pebble` is implemented in a depth first search in the graph of covered edges to find a free pebble all over the graph G , in order to move that pebble to site v . Similarly, one can also have breadth first search version of `Find_Pebble` method¹.
- `Rearrange_Pebbles` is a method which moves the found free pebble throughout the entire graph G and move the pebble to site v . It is usually followed by the `Find_Pebble` method.

Algorithm 1: Algorithm for `Find_Pebble`

```
Function Find_Pebble ( $G, v, seen, path$ ) :  
    seen( $v$ ) = True;  
    path( $v$ ) = -1;  
    if pebbles( $v$ ) > 0 then  
        | return True;  
    else  
        | for  $x \in$  out neighbors of  $v$  in the directed graph  $G$  do  
            | | if not seen( $x$ ) then  
                | | | path( $v$ ) =  $x$ ;  
                | | | found = Find_Pebble( $G, x, seen, path$ );  
                | | | if found then  
                    | | | | return True;  
        | return False;
```

With the combination of `Find_Pebble` and `Rearrange_Pebbles` methods, the *pebble game* algorithm can search for free pebbles over the entire graph and move the found pebble to the site as desired. If such free pebble is not available, the pebble search will also return a signal to indicate the failure of such pebble search.

The `Load_Pebbles` method can be implemented using `Find_Pebble` and `Rearrange_Pebbles` methods, and it tries to load *two* free pebbles for arbitrary site v in the graph. This turns

¹To reach a better practical performance, the `Find_Pebble` algorithm is implemented using an iterative strategy instead of recursive like shown in Algorithm. 1.

Algorithm 2: Algorithm for Rearrange_Pebbles

```
Function Rearrange_Pebbles ( $G, v, path$ ):  
  while  $path(v) \neq -1$  do  
     $w = path(v)$ ;  
    if  $path(w) = -1$  then  
      pebbles( $v, w$ ) += 1;  
      pebbles( $w$ ) -= 1;  
    else  
      pebbles( $v, w$ ) += 1;  
      pebbles( $w, path(w)$ ) -= 1;  
    if pebbles( $v, w$ ) > 1 then  
      pebbles( $v, w$ ) -= 1;  
      pebbles( $v$ ) += 1;  
    Reverse the edge direction from  $(v, w)$  to  $(w, v)$  in  $G$ ;  
     $v = w$ ;
```

out to be a very powerful method, since if one can find two free pebbles for both of sites connecting to a bond, this bond is an independent constraint according to the Laman condition. To determine whether a bond is independent or redundant is one of the key goals when utilizing the *pebble game* algorithm.

When building the directed graph G for the network, the pebble is either free or it covers a bond connecting to the site that the directed edge points from. Uncovered bonds play no role. This means that if a bond is redundant, it will *not* be included in graph G . All bonds which connect pairs of sites belonging to the Laman subgraph associated to such redundant bonds are *overconstrained*. This information must be *explicitly* recorded when it is of interest because it will be lost once the next pebble search is completed.

2.1.2 Rigid cluster decomposition

A systematic search to map out all rigid clusters is made after building up the network with the pebble search routine. To identify rigid clusters in the network, one can start from the method of identifying redundant bonds from the pebble search. The rigidity between a pair of sites is checked using a dummy test bond connecting them. If the test bond is redundant,

Algorithm 3: Algorithm for Load_Pebbles

```
Function Load_Pebbles( $G, v$ ):  
  Initialize path = -1, seen = False;  
  while pebbles( $v$ ) < 2 and Find_Pebble( $G, v, \text{seen}, \text{path}$ ) do  
    % find the first pebble;  
    Rearrange_Pebbles( $G, v, \text{path}$ );  
    % find the second pebble;  
    if path( $v$ ) == -1 then  
      for  $x \in$  out neighbors of  $v$  in the directed graph  $G$  do  
        if not seen( $x$ ) then  
          path( $v$ ) =  $x$ ;  
          found = Find_Pebble( $G, x, \text{seen}, \text{path}$ );  
          if found then  
            Rearrange_Pebbles( $G, v, \text{path}$ );  
    if pebbles( $v$ ) == 2 then  
      return True;  
    else  
      return False;
```

the pair sites are mutually rigid. Sites are defined as in the same rigid cluster if they are mutually rigid to each other. A site can be shared by more than one rigid clusters and in this situation such site acts as a pivot site. Multiple rigid clusters can be connected together in a network through pivots forming macroscopic floppy regions that are governed by collective motions. As a result, sites can be shared with multiple rigid clusters while bonds fall into their specific rigid clusters.

To perform the rigid cluster decomposition:

- Introduce a new rigid cluster label for an unlabeled bond e .
- Loop through all unlabeled bonds e_i in the graph to check its rigidity with respect to e . In order to see if those two bonds are mutually rigid, build four *dummy* test bonds connecting the sites of e_i and e , and check if all of those four dummy bonds are redundant. If all dummy bonds are redundant, bond e_i is in the same rigid cluster with e , so e_i is labeled as the same rigid cluster index to e . Note that the four dummy

test bonds will not be built into the graph no matter they are redundant or not.

- Go back to Step 1 until all bonds are labeled with a rigid cluster index.

The rigid cluster decomposition can be done through an incremental graph search strategy when filling the spring-mass network with adding sites one-by-one. The rigid cluster information from previous snapshot can be used to determine rigidity of new-added bonds, due to the fact that a new bond can only merge rather than split rigid clusters.

There are two kinds of bonds in a rigid cluster: *isostatic* and *overconstrained* bonds. Isostatic bonds are essential bonds which build the minimal rigid structure of a rigid component and cannot be removed when maintaining the rigidity. However, overconstrained regions contain bonds which are redundant when running the pebble game algorithm, and those bonds can be removed without changing the overall rigidity. The overconstrained regions are identified from failed pebble search.

2.1.3 Emergence of the spanning rigid cluster

One can identify the spanning rigid cluster by testing whether the largest rigid cluster wraps around the periodic boundary of the lattice. When considering periodic boundary conditions, it is somewhat more difficult to detect the spanning, while it is also important since in percolation problems one has to detect the spanning percolating cluster to measure the critical threshold p_c . Here I introduce a technique for detecting cluster wrapping which is widely used in connectivity percolation problems [49, 50].

The method for detecting cluster wrapping on periodic boundary conditions is shown in Fig. 2.1 [50].

- After running rigid cluster decomposition, pick out the rigid cluster which contains the most number of sites as the giant rigid cluster.
- Pick one site from the giant rigid cluster as the root site of the cluster (shaded).

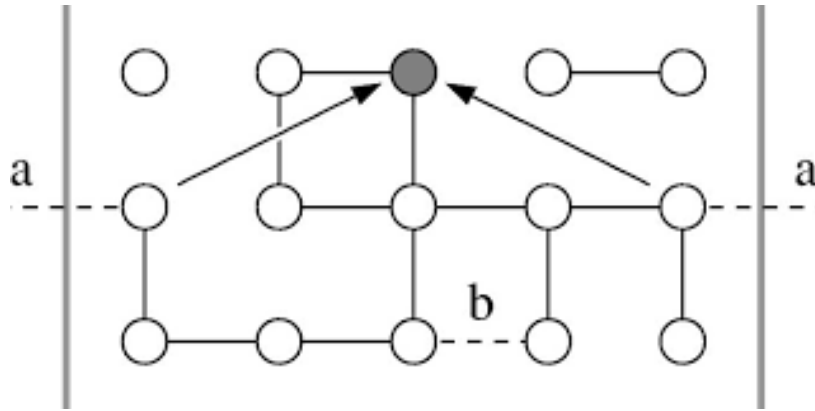


Figure 2.1: Method for detecting cluster wrapping for connectivity percolation on periodic boundary conditions. In RP problem, all the sites in the connected cluster represent sites in the giant rigid cluster.

- Starting from the root site, run graph search (can be either breadth first search or depth first search) in the giant rigid cluster. For each site the graph search reaches, calculate its displacement to the root site (arrows).
- At every step of such graph search, compare the site displacements to the root site, and there will be two cases:
 - Graph search along bond (a) in Fig. 2.1: the difference between these displacements is not equal to a single lattice spacing, instead the difference can be the system size or even multiple times of the system size. In this case, the cluster wraps around the system. If the cluster wrapping is found, terminate the graph search and return *true*.
 - Graph search along bond (b) in Fig. 2.1: the difference between these displacements is equal to a single lattice spacing. This case indicates that the cluster wrapping has not taken place yet.
- After the graph search of the entire giant rigid cluster, if cluster wrapping is still not found, return *false*.

The emergence of spanning rigid cluster in 2D systems can be determined in either x

direction or y direction, or it can also be determined as spanning in both x and y directions. Any case can be used as the measurement of the critical threshold for RP. There are a number of possible methods for determining the position of connectivity percolation threshold numerically on a regular lattice [44], and similarly there are also various measurements for determining the location of RP threshold.

2.2 Matrix decomposition in linear elasticity

As illustrated in Section 1.3, the dynamical matrix \mathbb{D} is defined as the Hessian given by the second derivative of the energy with respect to particle positions, so the linearized equations of motion are

$$|\ddot{u}\rangle = -\mathbb{D}|u\rangle$$

Thus the eigenvectors of the dynamical matrix \mathbb{D} are the normal vibrational modes of the system with the eigenvalues indicating the squared corresponding frequencies. It is of great interest for finding out the normal modes for the system, which is to diagonalize the dynamical matrix \mathbb{D} and solve for its eigenvalues as well as eigenspaces.

The high performance computing package ARPACK [51] is designed to compute a few eigenvalues and corresponding eigenvectors of large sparse or structured matrices, and is suitable for solving normal modes of disordered systems, but with some difficulty in highly degenerate eigenvalue conditions [52]. However, when considering the systems with a large amount of SSSs or ZMs, it is usually the case of having high degeneracy in \mathbb{D} .

Here I'm introducing the tool I used for calculating the SSS or ZM in large systems, and in the scope of this dissertation, it is the following routine that is used in the SSS study for Chapter 5.

2.2.1 Numerical orthonormal null space bases

To solve for SSSs or ZMs in large disordered systems is to solve for orthonormal null space bases for \mathbb{Q} and \mathbb{C} matrices. In the meantime, the counting of SSSs or ZMs is to determine the numerical ranks of those elastic matrices. The most widely used and accurate method for determining the numerical rank and null space is the *Singular Value Decomposition* (SVD). However, SVD is expensive for large sparse matrices, which are usually the cases when dealing with complicated disordered systems.

QR decomposition is an efficient and reliable alternative to SVD for finding out null space bases and numerical ranks of large matrices. In order to get the numerical orthonormal null space bases of matrix $A \in \mathbb{R}^{m \times n}$, rank-revealing QR decomposition to its transpose is performed as $A^T \Pi = QR$, where Π is a permutation matrix, $Q \in \mathbb{R}^{n \times n}$ satisfying $Q^T Q = \mathbb{I}_n$ and the upper triangular matrix R is defined as

$$R = \begin{bmatrix} R_{11} & R_{12} \\ 0 & R_{22} \approx 0 \end{bmatrix},$$

where $R_{11} \in \mathbb{R}^{r \times r}$ and $R_{22} \in \mathbb{R}^{(n-r) \times (m-r)}$ has a very small norm. The numerical rank of A , which is r , can be determined by calculating the number of entries on the main diagonals of R whose magnitude exceeds a numerical tolerance, so R_{22} is picked out from R_{11} . As a result, the last $n - r$ columns of Q after column pivoting from Π make up the null space of A , giving its numerical orthonormal null space bases.

There are different ways of implementing the above QR decomposition routine in order to solve for the null space of large matrices. I predominantly use the package SPQR_RANK [53] which contains routines that calculate the numerical rank of large, sparse, numerically rank-deficient matrices, and it has a method called SPQR_NULL which solves the orthonormal null space bases for the matrix. This algorithm along with other algorithms in the SPQR_RANK package, are all based on the SPQR routine from SuiteS-

parseQR [54], which is a high performance sparse QR factorization from SuiteSparse [55].

When solving for SSSs in large overconstrained systems, the null space for the equilibrium matrix \mathbb{Q} has very high dimensions (See Chapter 5). A great advantage of SPQR_NULL is that it can provide a reliable determination of null space base vectors for large sparse matrices, providing a stable tool to solve for SSSs when there are lots of degeneracies for \mathbb{Q} diagonalization. Similarly, SPQR_NULL is also reliable when solving for the null space of \mathbb{Q}^T to get ZMs in large and floppy systems.

CHAPTER 3

Correlated Rigidity Percolation and Colloidal Gels

This chapter summarizes the published work “*Correlated rigidity percolation and colloidal gels*” *Physical review letters* 123, no.5 (2019): 058001 co-authored by Shang Zhang, Leyou Zhang, Mehdi Bouzid, D. Zeb Rocklin, Emanuela Del Gado, and Xiaoming Mao.

3.1 Introduction

The emergence of mechanical rigidity in soft amorphous solids is central to many material technology developments from 3D printing with soft, biocompatible inks [56] to designing food texture [57, 58], but it is poorly understood and controlled. The main theoretical framework is based on the idea that locally rigid structures, due to mechanical constraints such as chemical bonds or steric repulsion, percolate through the material. Hence the problem translates into the onset of rigidity in a disordered network of springs, an abstraction of the actual solid, whose RP transition has been intensively studied especially in relation with molecular glasses [2, 59–63]. With respect to percolation phenomena controlled by the geometric connectivity [44], the onset of rigidity requires a mechanically stable spanning cluster able to transmit stresses, a problem intrinsically vectorial and long-range [2]. As a result, compared to geometric percolation, RPs display different critical exponents and occur at *higher* volume fractions (e.g., 63% for site RP on a two-dimensional triangu-

lar lattice [1] and 36% for site RP on a three-dimensional face-centered-cubic lattice [64]). It is therefore surprising that soft amorphous solids such as colloidal gels—formed in suspensions of colloidal particles with prevalently attractive interactions (due to dispersion or depletion forces)—can be mechanically rigid at low volume fractions, and even as low as a few percent [41, 65, 66].

Basic formulations of RP ignore any structural correlation: bonds or sites are randomly removed from a lattice, with no correlation between them, until the structure loses its rigidity. While this approach provided well-tested predictions for glasses [59], the nature of the rigidity transition can significantly depend on how the final structure is assembled [61, 63, 67]. For example, when rigidity emerges as frictionless spheres jam due to compression, a spanning rigid cluster that includes nearly all particles suddenly appears and, with one more contact, the whole system is stressed [18, 32, 68, 69]. This scenario differs from basic RP where the spanning rigid cluster is fractal at the transition, although both transitions (jamming and RP) occur near the isostatic point [6, 12, 13, 18, 20], where the mean coordination number equals two times the spatial dimensions, $\langle z \rangle = 2d$. The emergence of rigidity in jamming is so different from the classical RP because the self-organization of the structure, accommodating the repulsive interactions among the particles as they are pushed together, dictates the nature of the rigidity transition. It has been recently suggested that the presence of attractive interactions may further change the nature of the rigidity transition at jamming [70], but the emergence of rigidity when the self-organization of the structure is due to aggregation and gelation in a thermodynamic system [41, 65, 71–73] is a much less explored question and remains fundamentally not understood.

Here we propose and demonstrate that spatial correlations can shift the RP to low volume fractions and are therefore crucial to the onset of rigidity in materials like colloidal gels. Using a lattice model in which sites are occupied with local density correlations, we show that the RP threshold shifts to lower volume fraction as correlation strength increases,

albeit with the same critical exponents as the classical RP (Fig. 3.1ab). Our *Molecular Dynamics* (MD) simulations of a colloidal-gel model where particles aggregate due to short-range attractions confirm that increasing interaction strength can lead to RP at progressively lower volume fractions by increasing the correlation strength (Fig. 3.1cd). A simple way to illustrate how structural correlations move the RP to lower volume fractions is that correlations may organize particles into “smart” thin structures that transmit stress. When particles are arranged on a Warren truss which is rigid (Fig. 3.1a inset), the volume fraction of this one-dimensional structure on a two-dimensional plane vanishes in the thermodynamic limit. As we show below, spatial correlations originating from short-range attractive interactions naturally prepare particles into such types of structures, giving rise to rigidity at low volume fractions.

For suspensions of attractive colloidal particles, structural correlations are often accessible in experiments and well rationalized via statistical mechanics: fractal aggregation models, cluster theories and density functional theories provide good understanding of structural correlations resulting from short-range attractive interactions [74–76]. While for polymer gels it has been long understood that not all sub-parts of a gel are necessarily rigid [77], for colloidal gels most of existing studies simply assume that all persistent clusters or sub-structures are rigid, in spite of floppy, non-rigid clusters being observed [78]. Hence gelation has been mainly discussed in terms of the geometric percolation of such structures and of the related particle localization [79–85]. Only recent work has started to address specifically the rigidity rather than just the connectivity [78, 86–91]. A clear view of how the interplay between RP and particle localization in the gel structure gives rise to colloidal gelation has been therefore so far lacking. Our findings provide a novel concept and rigorous theoretical framework for understanding the emergence of rigidity in colloidal gels: the rigidity of aggregates comes from the coordinated organization of many interacting particles rather than from the fact that each single cluster is rigid.

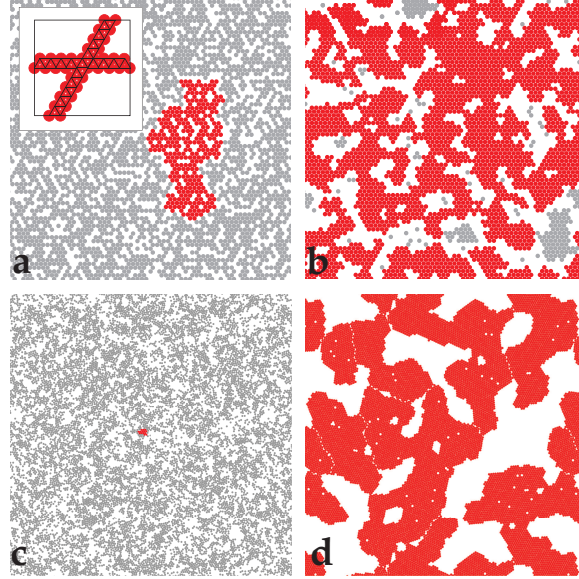


Figure 3.1: Examples of rigid cluster decomposition of the correlated lattice model ($\phi_l = 0.6$) at different correlation strengths [$c = 0$ in (a) and $c = 0.6$ in (b)], and the attractive gel model ($\phi_g = 0.6$) at $k_B T/\epsilon = 0.4$ in (c) and 0.1 in (d). Red particles belong to the largest rigid cluster, and other particles are colored in gray. In both models, correlation/attraction induces rigidity at volume fractions below the rigidity transition in the uncorrelated/repulsive limit. The rigid clusters percolate in (b) and (d) where there is strong correlation/attraction, but not in (a) and (c). The inset in (a) shows an extreme example where particles are perfectly correlated (on a Warren truss) and exhibit rigidity at $\phi = 0$ in thermodynamic limit.

3.2 Models and Methods

We use two models to investigate the effect of correlation on rigidity. We work in 2D, to be able to use a very efficient method for identifying rigid clusters, the “pebble game” algorithm [2, 47], to obtain the large numerical samples needed to analyze the RP critical behavior. Nevertheless, all arguments (theoretical and phenomenological) extend to 3D. The first model, the *correlated lattice model*, is a modified version of the site-diluted triangular lattice model for RP [1]. Instead of randomly populating lattice sites with a uniform probability, we put particles on a triangular lattice according to the following protocol. At each step, an empty site is randomly chosen, and a particle is put on this site with probabil-

ity

$$p = (1 - c)^{6 - N_{nn}} \quad (3.1)$$

where N_{nn} is the number of its nearest-neighbor sites which are already occupied ($0 \leq N_{nn} \leq 6$) and c is a dimensionless constant controlling the correlation strength ($0 \leq c < 1$). We start with an empty triangular lattice and repeat this process until a target volume fraction ϕ_l is reached (subscript l denotes “lattice”), which relates to the fraction of occupied sites f through $\phi_l \equiv \pi f / (2\sqrt{3})$. We then obtain a spring network where all nearest neighbor pairs, if both exist, are connected. The limit of $c = 0$ corresponds to the classical RP with no structural correlation (all sites occupied with the same probability).

The second model, the *attractive gel model*, is an assembly of interacting colloidal particles, studied via MD in 2D. The particles interact through a pairwise Lennard-Jones-like potential which displays a short range attraction (of depth ϵ) and a repulsive core [92, 93]. We generate configurations at different volume fraction ϕ_g (subscript g denotes “gel”), and different ratios between the thermal energy and the attractive well depth $k_B T / \epsilon$, by solving the many-body Newton’s equations of motion in a square simulation box with periodic boundary conditions. In spite of its simplicity, our simulations include the essential ingredients of thermodynamics and dynamics in colloidal gels. For each particle configuration, we obtain the corresponding spring network by assigning bonds between pairs of particles of center-to-center distance 1.03σ (the inflection point of the potential) or less. In both models we consider purely central forces, which have been used successfully to understand experiments on colloidal gels in a large part of the literature [41, 85, 87, 92, 94, 95]. Non-central forces may also be important [96–100] and can be included in our approach through bond-bending rigidity [28, 101, 102]. Further details of our simulation protocol are included in the appendix at Section 3.4. We analyze the rigidity of all the spring networks from the two models using the pebble game algorithm [2, 47], which decomposes the networks into rigid

clusters. RP occurs when the largest rigid cluster percolates in both directions, leading to macroscopic rigidity [38, 63].

3.3 Results

In both models, we find that with correlation/attraction, rigidity emerges at volume fractions lower than in uncorrelated cases (Fig. 3.1). In the correlated lattice model, we measure two quantities, the probability of having a percolating rigid cluster $P(\phi_l, c, L)$, and the average mass of the largest rigid cluster $\mathcal{M}(\phi_l, c, L)$, where L is the linear size of the lattice. Following the notion of percolation, \mathcal{M} is the order parameter of the transition. As shown in Fig. 3.2, when the correlation strength c increases, both P and \mathcal{M} curves shift to the left, confirming that RP occurs at a lower ϕ_l in the presence of correlation. Moreover, the gradual increase of \mathcal{M} at the transition suggests that the correlated rigidity transition is still continuous, as the classical RP. The fact that P and \mathcal{M} for different L intersect at the same scale-free point confirms this.

We analyze critical scaling relations near the correlated rigidity transition using finite-size scaling (details in appendices). We first determine the transition point $\phi_{l,c}(c, L)$ where the spanning rigid cluster first appears, averaging over disordered samples. For each c , the transition point shifts as a function of L following standard finite-size scaling relations with correlation length exponent $\nu = 1.21$ (agreeing with classical RP [2]), towards the infinite volume limit, $\phi_{l,c}(c, L = \infty)$. We find that the transition point decreases with c

$$\phi_{l,c}(c = 0, L = \infty) - \phi_{l,c}(c, L = \infty) = a c^{1/\zeta}, \quad (3.2)$$

at small c , where $\zeta \simeq 0.76$, the coefficient $a \simeq 0.19$, and the $c \rightarrow 0$ limit transition point is $\phi_{l,c}(0, \infty) \simeq 0.63$ agreeing with the classical RP result (note the extra factor of $\pi/(2\sqrt{3})$ converting from site occupancy probability to volume fraction).

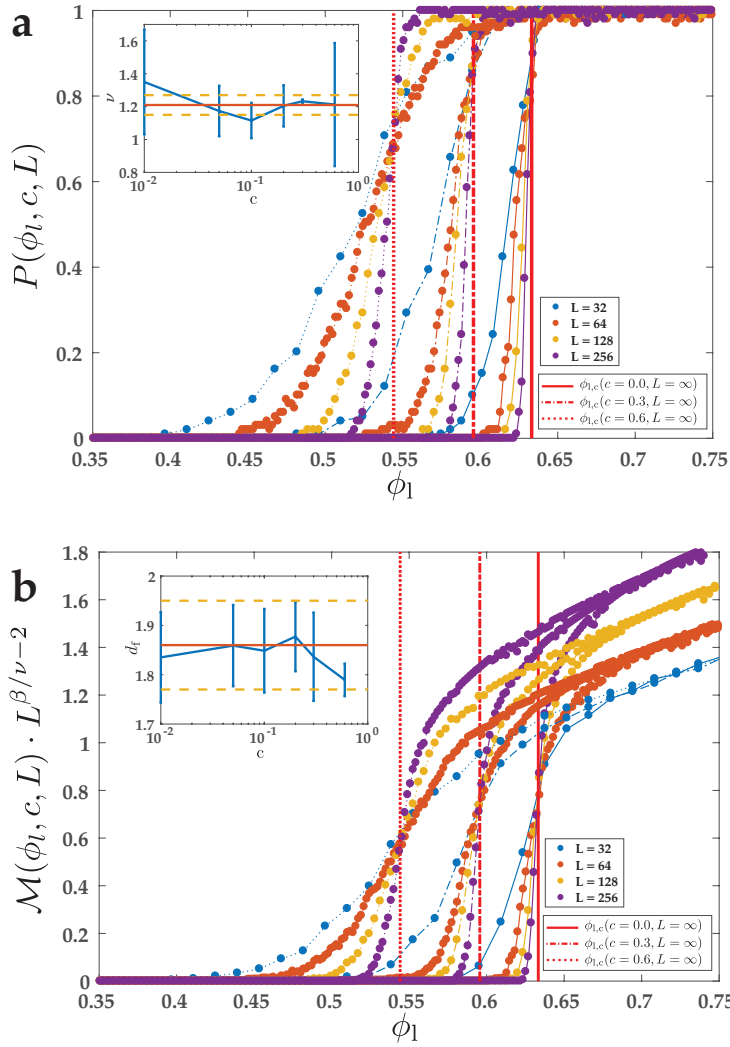


Figure 3.2: (a) $P(\phi_l, c, L)$ at different L and c (symbols and line styles defined in legends). Inset: ν for different c (blue with error bars), in comparison with average (red line) and standard error (yellow dashed line) of ν in the classical RP (from Ref. [1]). (b) $\mathcal{M}(\phi_l, c, L)$ at different L and c . Inset: d_f for different c (blue with error bars), in comparison with average (red line) and standard error (yellow dashed line) of ν in the classical RP (from Ref. [1]). In both (a) and (b), curves for different L cross at the same point (marked by red lines), indicating continuous transitions at every c at different $\phi_{l,c}(c, L = \infty)$.

The data for P and \mathcal{M} can then be collapsed using the following scaling forms

$$P(\phi_l, c, L) \sim \tilde{P}[(\phi_l - \phi_{l,c}(c, L = \infty))L^{1/\nu}], \quad (3.3)$$

$$\mathcal{M}(\phi_l, c, L) \sim L^{d-\beta/\nu} \tilde{\mathcal{M}}[(\phi_l - \phi_{l,c}(c, L = \infty))L^{1/\nu}], \quad (3.4)$$

where ν and β are the critical exponents for the correlation length and the growth of the order parameter (figures in appendices). These scaling relations share the same form as ones used in classical RP with the same exponents ($\nu = 1.21$ and $\beta = 0.18$) [2], but with correlation dependent transition points $\phi_{l,c}(c, L = \infty)$ which we determine above.

Our results suggest that correlations play the role of an irrelevant perturbation at the RP transition. They shift the transition point $\phi_{l,c}(c, L = \infty)$ while leaving critical exponents the same as in the uncorrelated case. Thus, with correlation, the RP still belongs to the same universality class, as also found in other percolation problems [108, 109]. One way to interpret this result is that the structural correlations we introduce in the model are a short range feature. Although they shift the transition, the critical scaling is controlled largely by the physics at large length scales and is not sensitive to microscopic modifications. We confirm this by measuring the critical exponents at different c . In particular, we measure ν via fluctuations of $\phi_{l,c}(c, L)$ over samples, $\Delta_\phi \equiv \sqrt{\langle \phi_{l,c}(c, L)^2 \rangle - \langle \phi_{l,c}(c, L) \rangle^2}$, as well as the fractal dimension of the giant rigid cluster at the transition $\mathcal{M}_c = \langle \mathcal{M}(\phi_{l,c}, c, L) \rangle$. We fit these quantities to their finite-size scaling relations,

$$\Delta_\phi \sim L^{-1/\nu}, \quad (3.5)$$

$$\mathcal{M}_c \sim L^{d_f}, \quad (3.6)$$

where the fractal dimension relates to β by $d_f = d - \beta/\nu$ (here $d = 2$ is the spatial dimension). Within error bars, ν and β agree with those of the classical RP for every c (Fig. 3.2 insets).

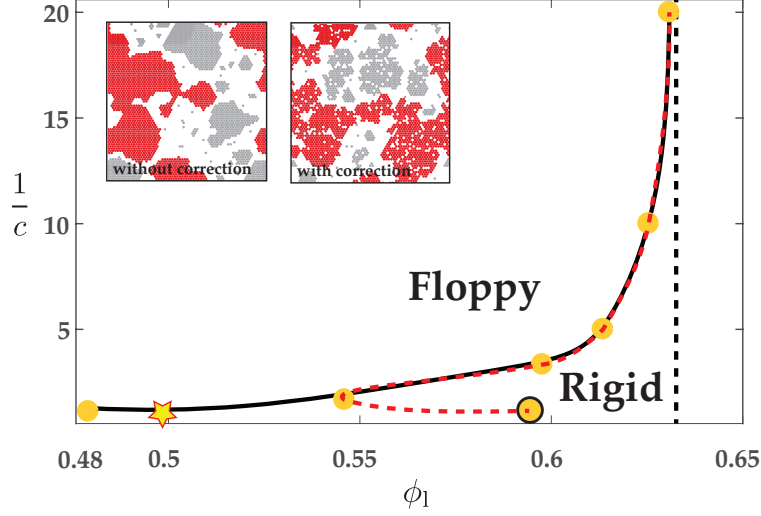


Figure 3.3: Phase diagram of the correlated lattice model (without and with the strong correlation correction). Calculated phase boundary $\phi_{l,c}(c, L = \infty)$ are shown as yellow dots (before correction: with black circles around the dots, after correction: without circles; They overlap at small c). The red dashed line and the black solid line show the phase boundaries before and after the correction by connecting the dots, respectively. The $c \rightarrow 0$ limit (classical RP) is shown as the black dashed line. The insets are configurations taken at $c = 0.9, \phi_l = 0.5$ (the yellow star) with and without the strong correlation correction, which avoids the formation of disconnected dense blobs and leads to a percolating rigid cluster.

The resulting phase diagram is shown in Fig. 3.3, with the phase boundary determined from $\phi_{l,c}(c, L = \infty)$. We plot the phase diagram in the ϕ_l vs $1/c$ plane for convenient comparison with the attractive gel model, where we identify the rigid gel states in the ϕ_g vs $k_B T/\epsilon$ plane, since correlations decrease as both $1/c$ and $k_B T/\epsilon$ increase. In the limit of $1/c \rightarrow \infty$ the transition reduces to the classical RP, while the boundary shifts to lower ϕ_l as c increases (as discussed above). However, when c is large (> 0.6) the phase boundary bends back to higher ϕ_l (dashed line in Fig. 3.3). The reason for this reentrant behavior is that very strong correlations force the particles to aggregate into densely packed blobs that do not percolate. This high c limit would correspond to a separation of the colloid-dense phase in an attractive colloidal suspension, rather than to the colloidal gelation that takes place through dynamical arrest and prevents the formation of disconnected droplets [94, 99, 101]. To better capture gelation, we add a correction for strong correlation: a site

can not be occupied if 4 or more of its neighboring sites are already occupied [$p = 0$ when $N_{nn} \geq 4$ and p still obeys Eq. (3.1) for $N_{nn} < 4$]. With the modified model, the RP transition volume fraction becomes monotonically decreasing as c increases, in better agreement with experiments and our attractive gel simulation described below.

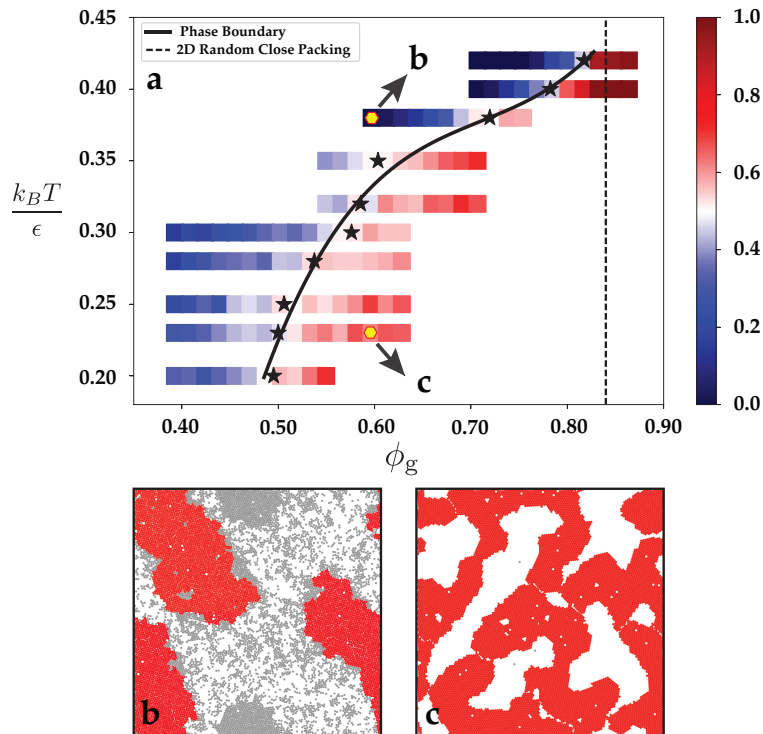


Figure 3.4: (a) Phase diagram of the attractive gel model. Simulated parameters $(\phi_g, k_B T/\epsilon)$ are shown as squares colored according to their measured $P_g(\phi_g, k_B T/\epsilon)$ (color scale shown in legend). Black stars show fitted phase boundary at each $k_B T/\epsilon$ and the black line is the phase boundary from fitting these transition points to third order polynomial. The hard sphere limit of the transition is shown as a black dashed line. (b,c) show two example configurations with their rigid cluster decomposition, chosen at the two marked points on the phase diagram. The largest rigid cluster percolates in (c) but not in (b), agreeing with the phase boundary.

Results from rigidity analysis of the attractive gel model are shown in Fig. 3.4. We simulate gels of 10^4 particles in $2D$ at various ϕ_g and $k_B T/\epsilon$, and obtain the mean probability for the emergence of a percolating rigid cluster $P_g(\phi_g, k_B T/\epsilon)$. At each $k_B T/\epsilon$ we identify the transition point $\phi_{g,c}(k_B T/\epsilon)$ by fitting $P_g(\phi_g, k_B T/\epsilon)$ as a quadratic function of ϕ_g and find the point where $P_g = 0.5$. These transition points are then fitted to a smooth curve to

construct the phase boundary of rigidity in the ϕ_g vs. $k_B T/\epsilon$ plane. In Fig. 3.4ab we show two sample configurations (with rigid cluster decomposition) at the same volume fraction $\phi_g = 0.6$ but for two distinct values $k_B T/\epsilon = 0.23$ and 0.38 . Large thermal fluctuations can frequently break bonds, and the resulting structure is either a homogeneous gas of particles (Fig. 3.1c) or displays phase separation but the large clusters do not show rigidity percolation yet (as shown in Fig. 3.4b). In contrast, decreasing $k_B T/\epsilon$, the attraction is so strong that the particle-rich regions not only percolate through the whole system, but also exhibit rigidity (Fig. 3.4c). The phase boundary bends down again at very strong attraction, where the system goes out of equilibrium and the rigidity is dominated by the physics of diffusion limited aggregation [110]. The similarity between the phase boundaries in the correlated lattice model and the attractive gel model indicates that the rigidity onset in dilute systems is favored by the structural correlations induced by the attractive interactions. Hence, the emergence of rigidity at colloidal gelation can be understood as a RP transition in which structural correlations help optimize mechanically stable structures [87, 90].

To summarize, we have studied the rigidity transition in a diluted triangular lattice model where particles populate sites with positional correlation, and a colloidal gel model with short range attraction using MD simulation. The two models show similar structural heterogeneities where particles clusters, forming stress-bearing networks that percolate through the system at low volume fractions. We analyze critical scaling exponents in the correlated lattice model, and find that the rigidity transition belongs to the same universality class as the classical RP, but the transition threshold moves to lower volume fractions as correlation increases. The attractive gel model further demonstrates that such structural correlations and heterogeneities can naturally arise as a result of short range attractive interactions in a thermal system. Deeper understandings of how this structural heterogeneity develops in the incipient phase separation and how it depends on the preparation protocol used for the gel (for example, the cooling rate or the gelation kinetics in the simulations) [111], as well as connecting correlated RP scenario obtained here to the

hard sphere limit where no attraction is present and rigidity emerges at the random close packing volume fraction (84% in 2D) or to the case in which different types of topological constraints may be present [112], will be intriguing topics to explore in future studies.

3.4 Appendices

3.4.1 The “pebble game” method: rigid cluster decomposition

To study the rigidity of the contact networks we obtained, we perform rigidity analysis by decomposing the networks into rigid clusters. The “pebble game”[2, 47] method is applied.

The “pebble game” method is a combinatorial algorithm based on Laman’s theorem [48], which states that a graph with N vertices and $2N - 3$ edges is minimally rigid if and only if no subgraph of n vertices has more than $2n - 3$ edges. Laman’s theorem counts constraints beyond the mean-field theory in two dimensions. The “pebble game” method is an efficient way to apply Laman’s theorem to networks and is able to perform tests such as (i) calculating the number of floppy modes, (ii) identifying over-constrained regions and (iii) locating rigid clusters.

For a given contact network obtained from the correlated lattice model or the attractive gel model, we assign each particle d pebbles that match its d degrees of freedom, where $d = 2$ is the dimension. We then use the “pebble game” method to classify each contact as either an independent constraint that absorbs one pebble, or a redundant constraint that absorbs no pebble. Rigid clusters, subsets of the system where contacts absorb all degrees of freedom except the $d(d + 1)/2$ rigid body motions, are then identified.

We can determine whether the largest rigid cluster spans around the system by testing whether the cluster wraps around the periodic boundary of the lattice [49, 50]. Fig. 3.1 shows example configurations of our correlated model as well as attractive gel model, with rigid clusters identified by the “pebble game” algorithm marked.

3.4.2 Colloidal gel simulation

Our model for the colloidal system is a $2D$ assembly of $N = 10^4$ particles (monodisperse in size) interacting through a Lennard-Jones-like potential

$$U(\mathbf{r}_1, \dots, \mathbf{r}_N) = \epsilon \sum_{i>j} u\left(\frac{\mathbf{r}_i - \mathbf{r}_j}{\sigma}\right) \quad (3.7)$$

where ϵ is the potential energy scale (setting the unit energy in our simulations) and σ is the diameter of particles (setting the unit length). $u(\mathbf{r})$ is a potential well obtained by combining, in the spirit of Lennard-Jones potential, an attractive term with a short range repulsive core, and, for computational convenience, is written as

$$u(\mathbf{r}) = A(a r^{-18} - r^{-16}), \quad (3.8)$$

where \mathbf{r} is the interparticle distance rescaled by the particle diameter and A and a are dimensionless constants. In particular we have fixed $A = 6.27$, $a = 0.85$ to obtain a short-ranged attractive well of depth ϵ and range $\simeq 0.3\sigma$ [102, 103]. We adopt periodic boundary conditions and, using the particle diameter σ , we define an approximate volume (surface) fraction $\phi_g = \pi(\sigma/2)^2 N/L^2$, where L is the side length of the square simulation box (in units of σ). We then set the box length according to the target volume fraction ϕ_g . The gel configurations are obtained using MD and a Nosé-Hoover thermostat to control the temperature [104], to mimic different interaction strengths $k_B T/\epsilon$ as usually done when simulating interacting colloidal particles [92, 105]. For the gel preparation we solve Newton's equations of motion for computational efficiency, having checked that the gel configurations obtained through the procedure described below do not meaningfully vary with varying the microscopic dynamics (i.e. Newton's *vs.* Langevin overdamped dynamics). For the MD simulations we use a time step $\delta t = 0.005\tau_0$, where $\tau_0 = \sqrt{m\sigma^2/\epsilon}$ is the usual MD unit time (m is the particle mass). All simulations reported here have been

performed with LAMMPS [106], suitably modified by us to include the interactions above.

The particles are initially equilibrated at a high temperature ($T \simeq 1$ in units of ϵ/k_B) and then slowly quenched to different target temperatures, corresponding to different $k_B T/\epsilon$ values, for $2 \cdot 10^6$ MD steps. For the lowest target temperatures, $T \leq 0.32\epsilon/k_B$, we make sure the system has reached a local minimum of the potential energy by solving the damped equations of motion

$$m \frac{d^2 \mathbf{r}_i}{dt^2} = -\xi \frac{d\mathbf{r}_i}{dt} - \Delta_{\mathbf{r}_i} U, \quad (3.9)$$

where ξ is the damping coefficient and has units of m/τ_0 , for $2 \cdot 10^5$ MD steps, within which the kinetic energy of the system drops to $\simeq 10^{-10}\epsilon$. All data discussed here have been averaged over 200 independently generated samples.

3.4.3 Finite-size scaling for lattice model

3.4.3.1 Identifying the position of phase transition boundary

We randomly generate 100 realizations of the correlated lattice model for each correlation strength c and system size L and identify the critical volume fractions for each configuration. The average critical volume fractions of the ensembles are measured by fitting a Gaussian distribution $\mathcal{N}(\mu, \sigma^2)$ to the probability distribution of the critical volume fractions, i.e. $\phi_{1,c}(c, L) = \mu$.

We then linearly extrapolate these finite critical volume fractions $\phi_{1,c}(c, L)$ for each c as a function of $L^{-1/\nu}$ to obtain the infinite-size limit $\phi_{1,c}(c, L = \infty)$ from the y-intersects of the linear fits, as shown in Fig. 3.5¹. Here, we adopt $\nu = 1.21$ from the uncorrelated RP. We also directly measure the critical exponents in the correlated RP (section 3.4.3.3), which are shown to be the same within error bars as those in the uncorrelated RP .

¹The error bar in small system size is rather wide compared to large system sizes, since in lattice model the discrete filling/diluting of sites leads to larger gap in density ϕ , which introduces more fluctuation for $\phi_{1,c}$.

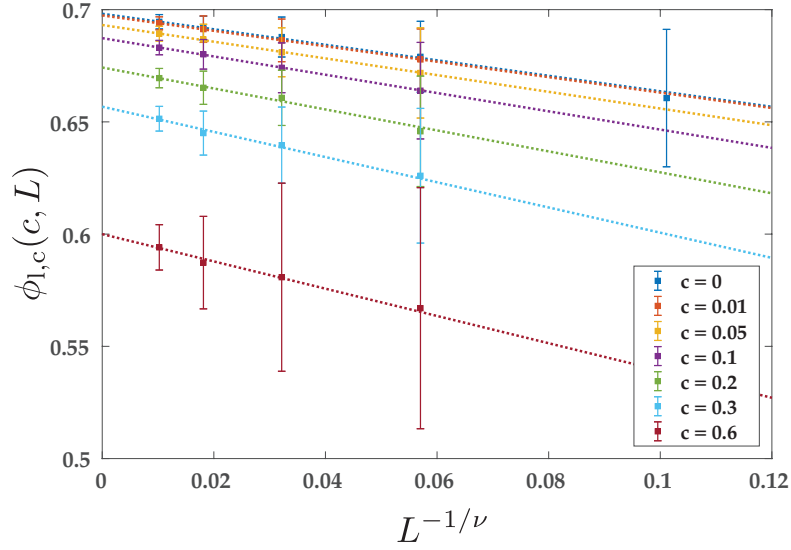


Figure 3.5: Linear extrapolation of the finite-size critical volume fractions as a function of $L^{-1/\nu}$ ($\nu = 1.21$ [2]). The dashed lines are linear fits, and the y-intercepts of these dashed lines represent the infinite-size limit of the critical volume fractions $\phi_{1,c}(c, L = \infty)$.

Using the extrapolated infinite-size critical volume fractions, we obtain the phase boundary for the correlated RP, as shown in Fig. 3.6. As a comparison, we also show the phase boundary of the modified model that is introduced in the main text (Fig. 3.6). In this phase diagram, all the critical volume fractions are also in the infinite-size limit. The only visible difference of the two phase boundaries is at $c = 0.9$.

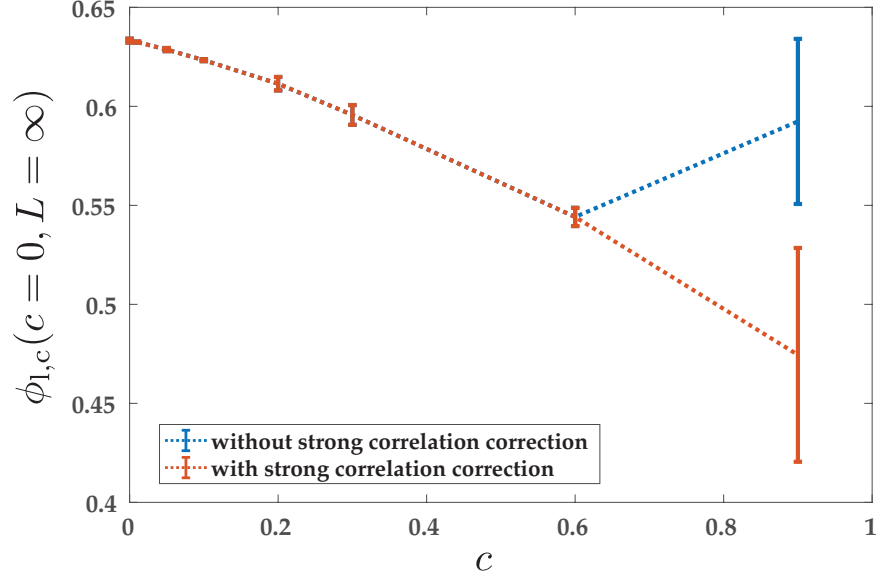


Figure 3.6: Transition point $\phi_{1,c}(c = 0, L = \infty)$ as a function of c for the correlated lattice model, without and with the strong correlation correction.

Scaling behavior of $\phi_{1,c}(c = 0, L = \infty)$ as a function of c at small c is shown as

$$|\phi_{1,c}(c = 0, L = \infty) - \phi_{1,c}(c, L = \infty)| = a c^{1/\zeta}. \quad (3.10)$$

The fitted parameters are $\zeta \approx 0.76$ and $a \simeq 0.19$. This fitting provides a quantitative measurement for the magnitude of the critical volume fraction shift as correlation strength c increases.

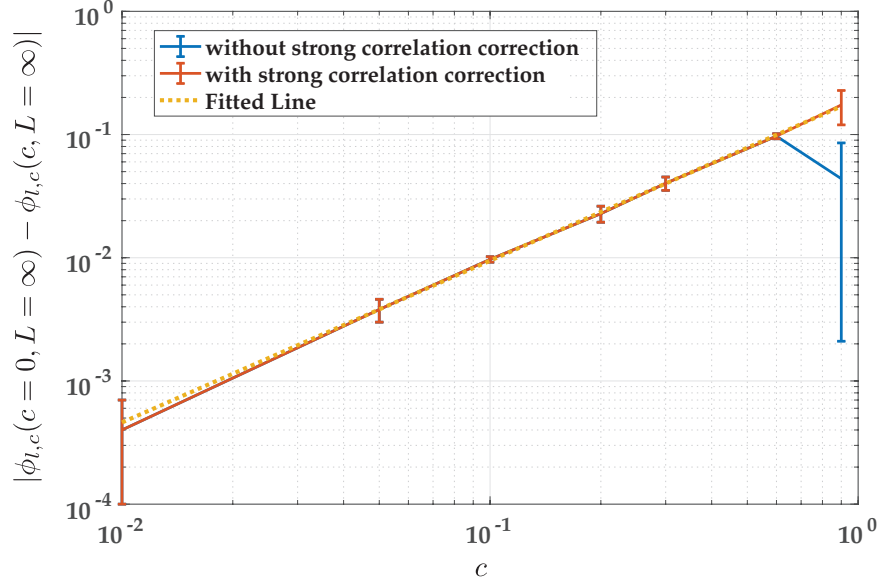


Figure 3.7: The fitting of the phase boundary as a function of the correlation strength c , as described in Eq. (3.10), without and with the strong correlation correction.

3.4.3.2 Scaling forms and data collapse

The scaling functions of the rigidity percolation are described as:

$$P(\phi_l, c, L) \sim \tilde{P}[(\phi_l - \phi_{l,c}(c, L = \infty))L^{1/\nu}], \quad (3.11)$$

and

$$\mathcal{M}(\phi_l, c, L) \sim L^{d-\beta/\nu} \tilde{\mathcal{M}}[(\phi_l - \phi_{l,c}(c, L = \infty))L^{1/\nu}]. \quad (3.12)$$

Here, we show that using the extrapolated infinite-size critical volume fractions and the critical exponents ν and β adopted from the uncorrelated RP, we are able to collapse the data of P and \mathcal{M} . (Fig. 3.8 and Fig. 3.9).

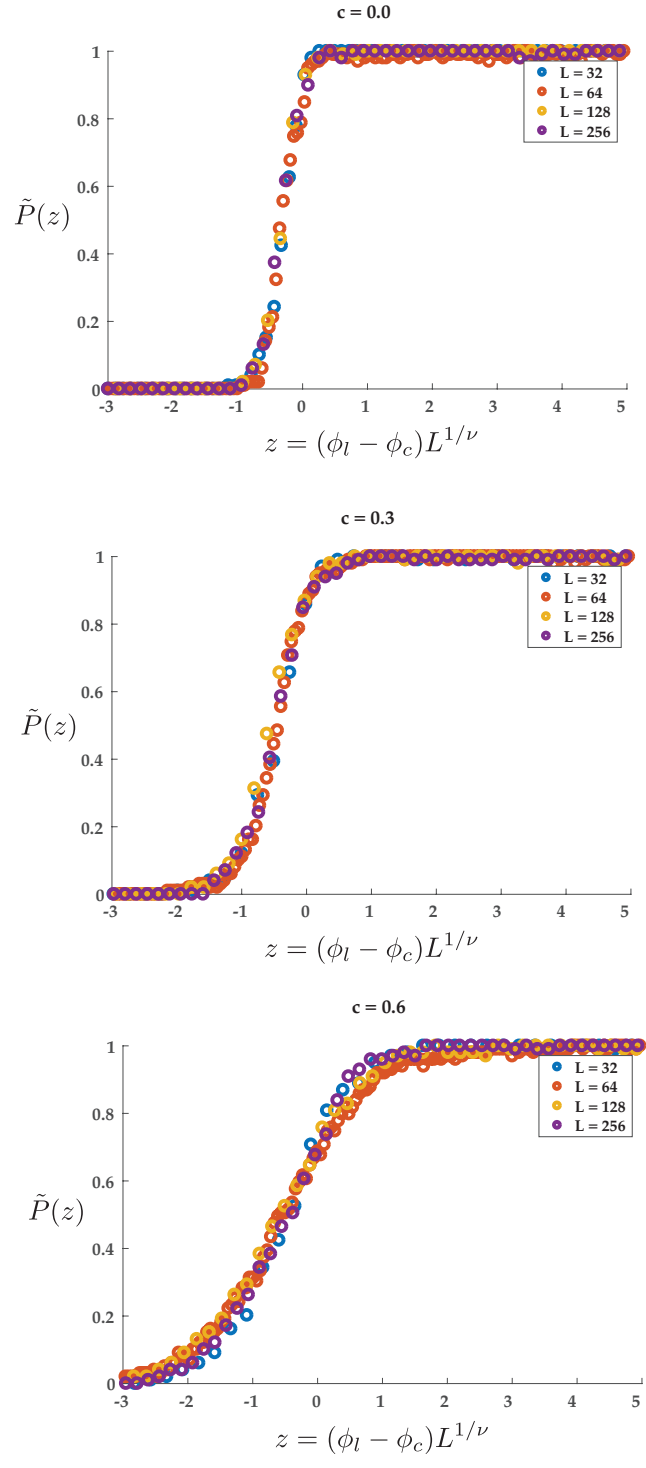


Figure 3.8: Collapsing of data for P , the probability of having a spanning rigid cluster, for the correlated RP, showing the master curve $\tilde{P}(z)$, where $z = [\phi_l - \phi_{l,c}(c, L = \infty)]L^{1/\nu}$ and $\nu = 1.21$. The exponent is from the uncorrelated RP[2].

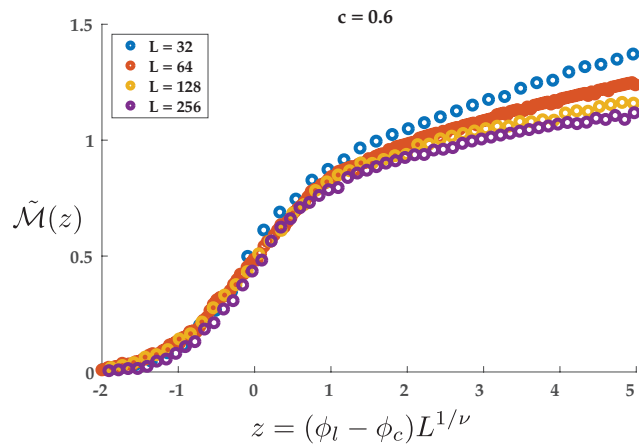
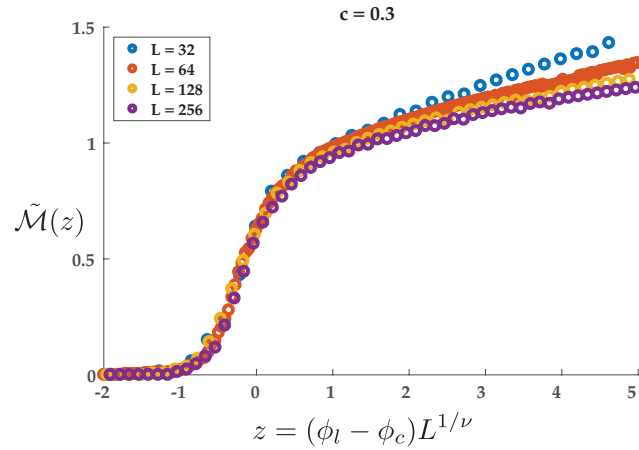
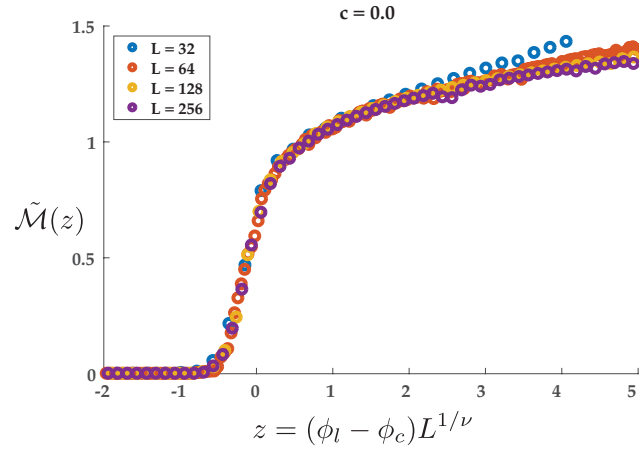


Figure 3.9: Collapsing of data for \mathcal{M} , the mass of rigid cluster in the correlated RP, showing the master curve $\tilde{\mathcal{M}}(z)$, where $z = (\phi_l - \phi_{l,c}(c, L = \infty))L^{1/\nu}$ and $\beta = 0.18, \nu = 1.21$. The exponents are from the uncorrelated RP [2].

3.4.3.3 Direct measurement of critical exponents

To further verify that the correlated RP is in the same universality class as the uncorrelated RP, we also directly measure the critical exponents in the correlated RP from the following scaling relations

$$\Delta_\phi \sim L^{-1/\nu}, \quad (3.13)$$

and

$$\mathcal{M}_c \sim L^{d_f}, \quad (3.14)$$

where $d_f = 2 - \beta/\nu$.

The critical fluctuation Δ_ϕ of critical volume fraction is measured as the standard deviation σ of the Gaussian distribution $\mathcal{N}(\mu, \sigma^2)$ fitted from the probability distribution of $P(\phi_l, c, L)$ for each c and L . The critical exponent ν is then fitted using Eq. (3.13). The fractal dimension for the spanning rigid cluster d_f is fitted from the finite-size scaling of $\mathcal{M}_c(\phi_l, c, L)$ for each c and L using Eq. (3.14). The exponent β are then obtained using $d_f = 2 - \beta/\nu$.

3.4.4 The rigidity diagram for gelation of colloidal particles

3.4.4.1 Defining contact networks

To construct the rigidity phase diagram of the colloidal particles, we need to define the spring network in the configurations generated through the MD simulations and then perform the “pebble game” algorithm to identify rigid clusters. We assume that a spring can be placed between two particles that are separated within a distance close to the minimum of the potential well. In our case, we choose $\simeq 1.03\sigma$, which is the inflection point of the interaction potential, defined as the distance where the second derivative of the potential is

zero, i.e.

$$U''(r) = 0. \quad (3.15)$$

At the inflection point, the attractive force starts to decrease with distance. At such distance two particles can be considered as bonded and the interactions can be approximated as a spring and hence 1.03σ is considered as the bond length in our analysis.

At low temperatures, bonded particles are indeed separated within this range in the vast majority of cases and hence using different lengths to identify the contact, or the bonded state (e.g. the inflection point or the total range of the attractive well) does not affect the results obtained. At high temperatures, instead, particles distances can vary significantly even when they are persistently within the well range, due to their kinetic energy, and they don't necessarily sit in the potential minimum. Nevertheless, the overall analysis of the rigidity boundary does not significantly change when we consider different bond lengths within the well range, due to the fact that we average the results of the rigidity analysis over several different MD initial configurations: either particles are instantaneously interacting but the bond between them is not persistent (and hence not relevant for the rigidity analysis) or the particles are actually interacting over a finite time and the potential minimum is indeed the most probable interparticle distance. For one specific target temperature, we generate 200 different initial configurations, and for each initial configuration we can extract the spring network using the bond length range 1.03σ . Then we can average over these results of the rigidity analysis to get the probability of having a spanning rigid cluster.

We also test the persistence of the clusters of bonded particles using the damping procedure described above. The local structures have been characterized in terms of the local *Bond Orientational Order Parameter* (BOP) characterizing local crystalline order in

2D [107]. The BOP of a particle k is defined as:

$$\psi_6(k) = \frac{1}{N} \sum_l^N \exp(i \cdot 6\theta_l), \quad (3.16)$$

where N is the number nearest neighbors for particle k and θ_l is the direction of neighboring particle l . Dense clusters of particles tend to be locally crystalline since the particles have the same size. (Fig. 3.10ab) shows, as expected, that for low temperatures ($k_B T/\epsilon \leq 0.32$ in our simulation), the damping tends to preserve the local structures of rigid clusters, and the obtained contact networks reflect the rigidity of the low temperature systems. For high temperatures ($k_B T/\epsilon > 0.32$ in our simulation), instead, the damping modifies the aggregates local structure, since those aggregates tend not to persist over time (Fig. 3.10cd).

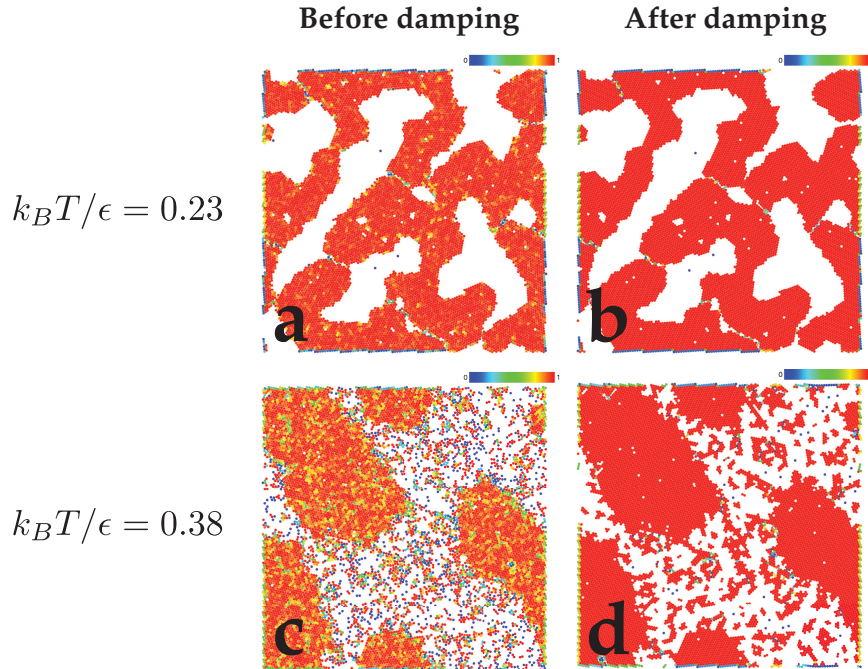


Figure 3.10: *Bond Orientational Order Parameter* (BOP) in sample configurations. (a,b) $k_B T/\epsilon = 0.23$, $\phi = 0.6$. (c,d) $k_B T/\epsilon = 0.38$, $\phi = 0.6$. (a,c) BOPs without the damping process. (b,d) BOPs with the damping process.

3.4.4.2 Rigidity boundary for the colloidal gel model

To find the transition point for RP of colloidal particles, we fit the mean probability for the emergence of a percolating rigid cluster $P_g(\phi_g, k_B T/\epsilon)$ to quadratic functions and interpolate for $P_g(\phi_{g,c}, k_B T/\epsilon) = 0.5$. These transition points at each $k_B T/\epsilon$ are shown in Fig. 3.4 and used to fit the phase boundary.

In Fig. 3.11 we show two examples $P_g(\phi_g, k_B T/\epsilon)$ fitted to second order polynomial functions. The interpolated transition points $\phi_{g,c}$ are also marked.

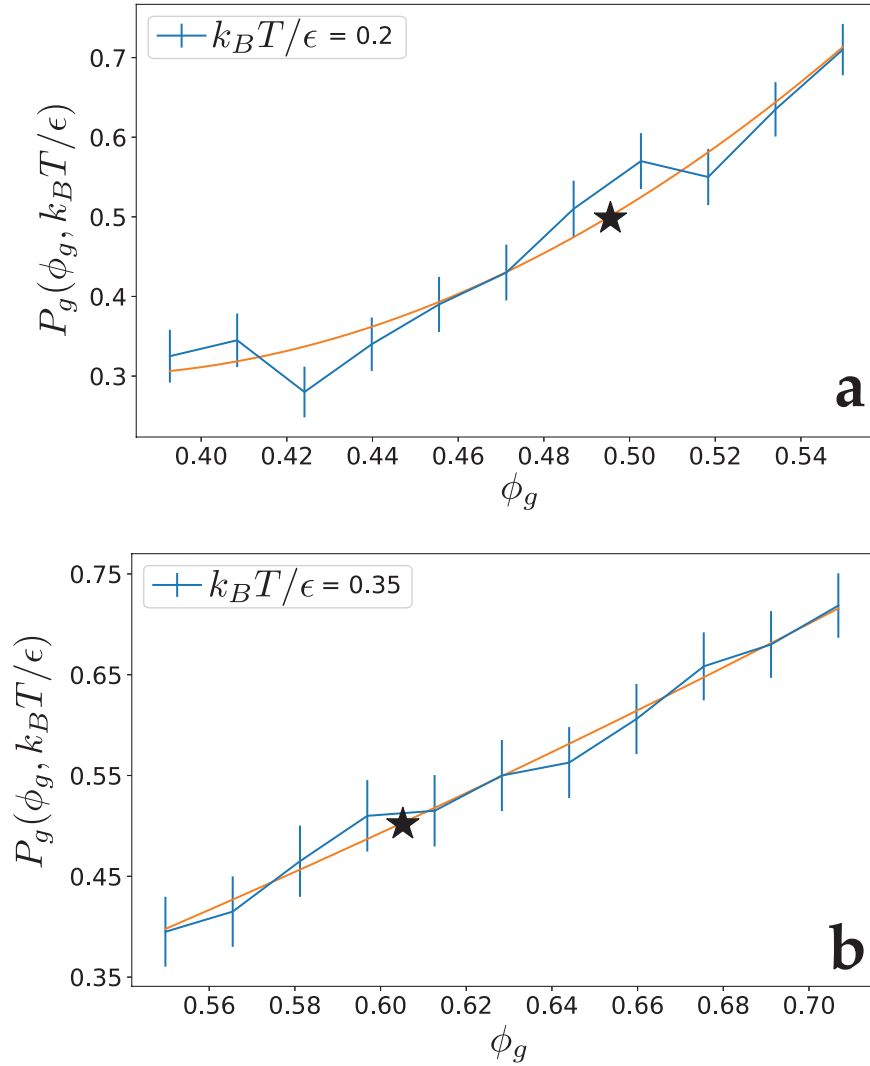


Figure 3.11: Fitting of $P_g(\phi_g, k_B T/\epsilon)$ to second order polynomial in two example cases, 9a) $k_B T/\epsilon = 0.2$ and (b) $k_B T/\epsilon = 0.35$, where the black stars indicate the extrapolated transition point defined as $P_g(\phi_g, k_B T/\epsilon) = 0.5$.

CHAPTER 4

Correlated Rigidity Percolation in Fractal Lattices

This chapter summarizes the published work “*Correlated rigidity percolation in fractal lattices*” *Physical Review E* 103, no.1 (2021): 012104 co-authored by Shae Machlus, Shang Zhang, and Xiaoming Mao.

4.1 Introduction

Soft disordered solids are ubiquitous; they exist in many forms such as colloidal gels, fiber networks, colloidal glasses, emulsions, aerogels, polymer melts, and foams. These classes of materials make up biological tissues, food products, cosmetic products, and materials like paper and nonwoven fabric. Some of these soft materials need only a very low density of solid particles to become rigid. In particular, colloidal gels can exhibit nonzero shear rigidity at a wide range of volume fractions [65, 89, 102, 113–117], which can be below 1% in the case of blood clots [115].

Classical RP problems are concerned with the emergence of rigidity in discrete mechanical networks. They have been studied in a number of lattices as models of rigidity transitions in soft matter. In these models one typically starts with an empty lattice and populates bonds or sites randomly while observing the emergence of a percolating cluster that *can carry stress*. In comparison with percolation (sometimes called “geometric per-

colation”), rigidity percolation not only requires the emergence of an infinite cluster, but also requires that stress can be transmitted from edge to edge of the whole lattice via this infinite cluster. For example, on a two-dimensional site-diluted triangular lattice, the percolation threshold is $1/2$, and the rigidity percolation threshold is about 69.8% in terms of the fraction of site occupancy [1].

Classical RP transitions are associated with high values of critical volume fractions ϕ_c for a material to be rigid (typically much greater than 10%) [1, 12, 13, 45, 64], so how can these ultra-low-density materials exhibit rigidity? Previous work suggested that the answer to this question lies in how the particles are spatially correlated to each other—the Warren truss, for example, transmits stress very efficiently and can achieve rigidity at $\phi_c = 0$ when viewed as a two or three dimensional structure [45]. While colloids will not spontaneously form in Warren trusses (as that involves an unrealistic amount of correlation), moderate correlation strength is still successful in lowering ϕ_c . While the type of correlation used in [45] was not enough for describing rigidity in ultra-low-density solids, it suggested that there may be another sort of spatial correlation that is both physically realistic and allows the system to achieve an arbitrarily low value of ϕ_c . We conjecture that a recursive correlation (which generates a fractal network) would be a promising candidate for describing rigidity at ultra-low-densities because (i) fractals are low density while still being connected, and they can be rigid, and (ii) experimental evidence suggests that low density disordered solids (coagulated blood, for example) can indeed be fractal as a result of the non-equilibrium process in which the material is assembled [65, 80, 117–121].

In this paper, we show that a model fractal network, the *Sierpiński Gasket Lattice* (SGL), does indeed achieve rigidity at arbitrarily low volume fractions. The SGL exhibits intrinsic positional correlation between the particles which increases with its number of fractal iterations n . This result is supported analytically by simple calculation on the undiluted SGL and numerically on the randomly diluted SGL by using the pebble game algorithm. We also calculate the correlation length and fractal dimension critical exponents for

RP in this lattice and find that the universality class of the rigidity phase transition in the lattice is the same as that for the regular triangular lattice. We further propose a simple non-fractal model, the RP of which yields a strict upper bound to the disorder-averaged critical volume fraction of the SGL.

4.2 Model

We use a lattice that achieves an arbitrarily low volume fraction while still exhibiting rigidity at full site occupancy. Motivated by the experimentally observed fractal structure of fiber networks and colloidal gels [80, 110, 117], we consider a triangular lattice where the upwards pointing triangles are replaced by *Sierpiński Gasket* (SG)'s, as shown in Fig. 4.1. The unit cell of this lattice is an upwards pointing SG with an adjoining vacant downwards pointing triangle, which forms a rhombus. Vibrational modes and spin phase transitions have been studied on this lattice [122–128]. This is a rich lattice to study since there are three length scales: (i) the size of the smallest triangle in an SG which we always set as 1, (ii) the length of the edge of an SG 2^n , and (iii) the length of the lattice $L = s2^n$. s is the number of SG's on one side of the lattice, and n is the number of times the SG pattern repeats on itself, what we call the fractal iteration number. We emphasize that L is measured in units of the smallest triangle of an SG since the length of the smallest triangle is always 1, independent of n . Also note that $n = 0$ corresponds to a regular triangular lattice.

The volume fraction of the SGL, at full site occupancy, is

$$\phi_{\text{SGL}_{\text{undiluted}}} = A \frac{3^{n+1} - 1}{2^{2n}}, \quad (4.1)$$

where the constant A is the area of the particle. In the SGL we consider here, $A = \pi/4\sqrt{3}$. This result is derived in Appendix 4.6.1, and it is obtained by assuming that each site is occupied by a disk whose diameter equals the bond length between neighboring sites,

pictured in Fig. 4.1(c). It follows that

$$\lim_{n \rightarrow \infty} \phi_{\text{SGL}_{\text{undiluted}}}(n) = 0. \quad (4.2)$$

An arbitrarily large n corresponds to an arbitrarily small $\phi_{\text{SGL}_{\text{undiluted}}}$, so the SGL is indeed a suitable model to study the emergence of rigidity in ultra-low-density networks. A single SG, of any n , is isostatic—it has 3 trivial zero modes and no states of self stress [6]. The coordination number of the undiluted lattice under periodic boundary conditions $\langle z \rangle_{\text{undiluted}}$ can be calculated as a function of n .

$$\langle z \rangle_{\text{undiluted}} = \frac{6 + 4(x - 1)}{x}, \quad (4.3)$$

where $x = (3^{n+1} - 1)/2$ is the number of sites present in a single n -level SG where $n \geq 1$. At $n = 0$, the lattice is a regular triangular lattice, so $\langle z \rangle_{\text{undiluted}} = 6$. The coordination number decreases from 6 to 4 as n goes from 0 to ∞ .

We dilute the SGL by removing randomly chosen sites. If a site is removed, all of the bonds attached to that site are also removed. The occupancy fraction p_{SGL} is the ratio of the number of occupied sites to the number of sites present in a completely filled SGL. As shown in Appendix 4.6.1, the volume fraction of the diluted SGL is then

$$\phi_{\text{SGL}} = p_{\text{SGL}} \phi_{\text{SGL}_{\text{undiluted}}}. \quad (4.4)$$

We emphasize that while the occupancy fraction p_{SGL} is the ratio of the number of occupied sites to total number of sites (unoccupied and occupied), the volume fraction ϕ_{SGL} is the ratio of the occupied space to the total space covered by the lattice. Because the volume fraction of the undiluted SGL $\phi_{\text{SGL}_{\text{undiluted}}}$ vanishes in the $n \rightarrow \infty$ limit, ϕ_{SGL} can approach 0 even when p_{SGL} is of $\mathcal{O}(1)$.

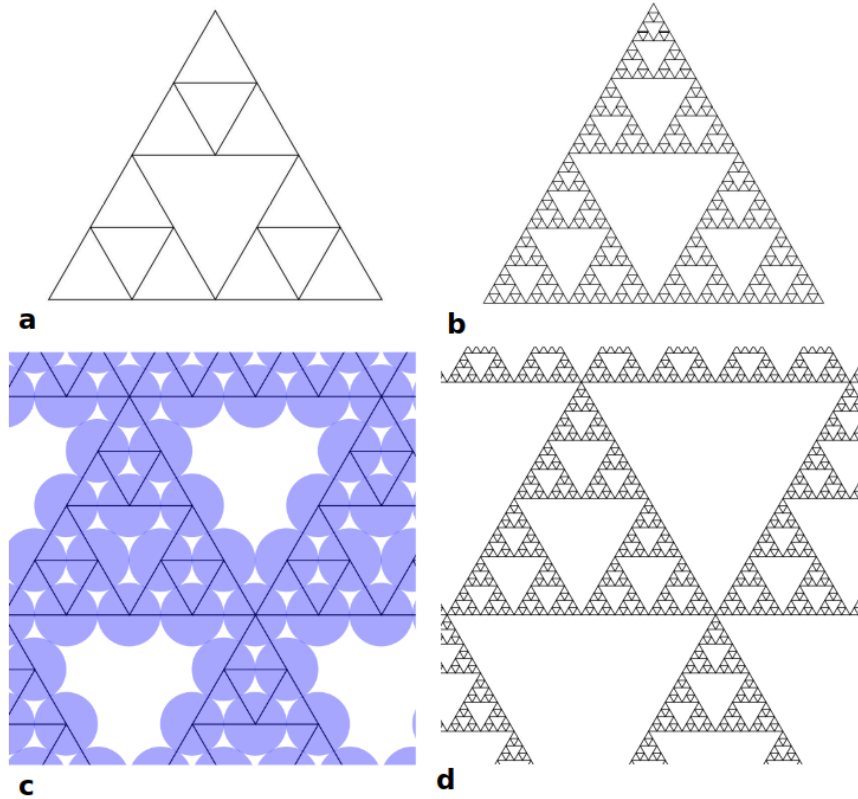


Figure 4.1: (a,b) Sierpiński gasket (SG) of fractal iteration $n = 2, 5$. (c,d) Lattices of SG's are models for ultra-low-density networks at $n = 2, 5$. In (c) semi-transparent purple disks represent the physical particles we are modeling. The diameter of each particle is equal to the bond length, which we set to 1.

4.3 Method & Results

A rigid cluster in a mechanical network is a collection of sites and bonds without any floppy modes. The only zero energy normal modes of a rigid cluster are trivial rigid-body degrees of freedom of the whole cluster. If a rigid cluster spans the whole network, the system must exhibit at least one positive elastic modulus. The emergence of such an infinite rigid cluster is called RP. It is worth mentioning that when rigidity percolates, floppy modes may still exist in other parts of the network which are not in an infinite rigid cluster. The pebble game is an efficient algorithm that can be used to examine rigidity in two dimensions [2, 47].

In order to study the RP in the diluted SGL, we execute the pebble game algorithm on

SGL's at $n = 1, 2, 3, 4, 5$ with periodic boundary conditions. For each value of n , we consider 4 different system sizes L which were chosen so that the lattices have approximately 250, 1000, 4000, and 16,000 particles (sites) (although at $n = 5$ we consider only the 3 larger system sizes because each SG at $n = 5$ already contains a large number of sites, and we need to keep the number of SG's large in the lattice). To keep the number of sites roughly constant across varying n , we reference

$$L = 2^{\frac{2n+1}{2}} \sqrt{\frac{N}{3^{n+1} - 1}}, \quad (4.5)$$

which is immediate from Eqs. (4.14) and (4.15) (Appendix 4.6.1), to choose an integer valued side length L for each target system size (in terms of the total number of sites) and fractal iteration n .

For each n and L , we generate 200 samples of SGL's. Each one represents a realization of disordered dilution. For each SGL, initially empty, we add new sites randomly to the lattice one by one. Each new site added increases p_{SGL} . We run the pebble game algorithm at regular intervals of p_{SGL} on this lattice to determine when a spanning rigid cluster appears. The occupancy fraction at which this occurs is the critical occupancy fraction $p_{c,\text{SGL}}$. We record the mass of the spanning rigid cluster $M_{c,\text{SGL}}$ when it first occurs in each sample. The code used to produce this data is contained in a GitHub repository [129]. We then average over the 200 samples to obtain the averaged quantities, $\langle M_{c,\text{SGL}}(n, L) \rangle$ and $\langle p_{c,\text{SGL}}(n, L) \rangle$, for each n and L . We also measure the fluctuation of the transition point

$$\Delta_{p_{c,\text{SGL}}} = \sqrt{\langle p_{c,\text{SGL}}(n, L)^2 \rangle - \langle p_{c,\text{SGL}}(n, L) \rangle^2}. \quad (4.6)$$

Our previous study of correlated RP on the triangular lattice [45] showed that the short-range spatial correlation only shifts the transition point and does not change the universality class of RP in the triangular lattice. Following this result, we make the assumption that RP in the SGL is also a continuous transition, with the mass of the infinite rigid cluster being

the order parameter. This assumption is verified by our scaling results below.

We invoke finite-size scaling relations [44, 45] to calculate the critical exponents associated with the rigidity phase transition. The correlation length exponent ν_{SGL} and the fractal dimension $d_{f,\text{SGL}}$ are calculated as the slopes of linear fits of log-log plots of $\langle M_{c,\text{SGL}} \rangle$ and $\Delta_{p_c,\text{SGL}}$ versus L , according to the finite size scaling relations

$$\langle M_{c,\text{SGL}}(n, L) \rangle \propto L^{d_{f,\text{SGL}}}, \quad (4.7)$$

$$\Delta_{p_c,\text{SGL}} \propto L^{-1/\nu_{\text{SGL}}} \quad (4.8)$$

(Appendix 4.6.2). Note that these relations give a calculation of $d_{f,\text{SGL}}$ and ν_{SGL} for each n .

We find ν_{SGL} and $d_{f,\text{SGL}}$ for the SGL rigidity phase transition are the same as for the rigidity phase transition in the regular triangular lattice [1] as shown in Fig. 4.2. This observation is consistent with results on RP in lattices with spatial correlations [45], where the critical exponents remain the same as in classical RP, and the short-ranged spatial correlation can be viewed as an irrelevant perturbation. Here, the fractals in each unit cell can also be viewed as a short range feature, which do not change the divergent length scale at the transition.

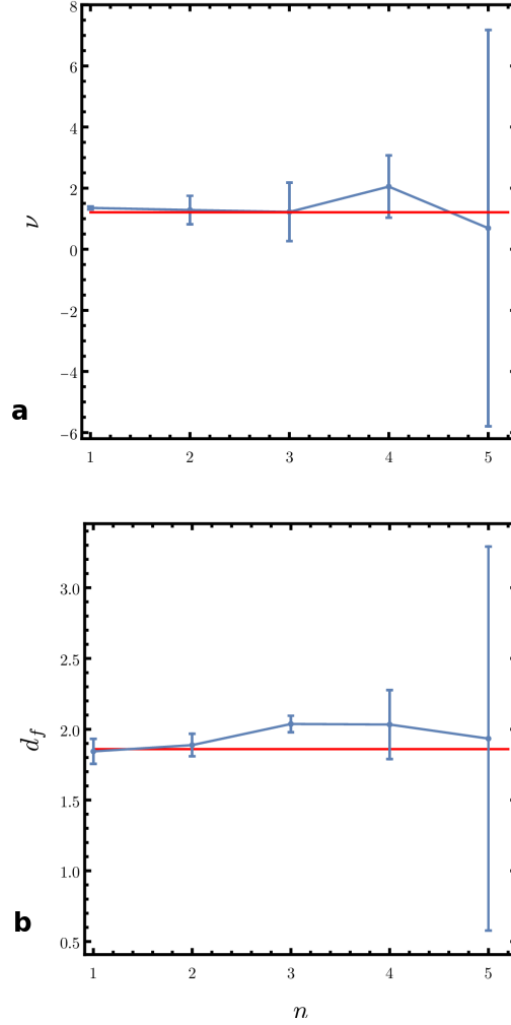


Figure 4.2: (a) The correlation length exponent ν_{SGL} at $n = 1, 2, 3, 4, 5$. (b) The spanning rigid cluster fractal dimension $d_{f,\text{SGL}}$ for the five values of n . The red lines show these exponents for classical RP in the regular triangular lattice ($\nu = 1.21 \pm 0.06$ and $d_f = 1.86 \pm 0.02$) [1]. The error bars are 95% confidence intervals.

We assert that the large-scale fractal structure of the spanning rigid cluster in the infinite system size limit overwhelms the local fractal structure of the SG's, so $d_{f,\text{SGL}}$ is the same as in the regular triangular lattice case instead of being the fractal dimension of the SG. We also verify that our assumption (the phase transition is continuous) is well justified since the phase transition belongs to the same universality class as [45].

We extract the critical occupancy fraction at the infinite system size limit $p_{c,\text{SGL}}(n, L = \infty)$ by linearly extrapolating the finite critical occupancy fractions $p_{c,\text{SGL}}(n, L)$ for each n

as a function of $L^{-1/\nu}$. The $p_{c,\text{SGL}}(n, L = \infty)$ are simply the y-intercepts of these linear fits which are displayed in Fig. 4.3¹. Further information about this process can be found in Appendix of [45].

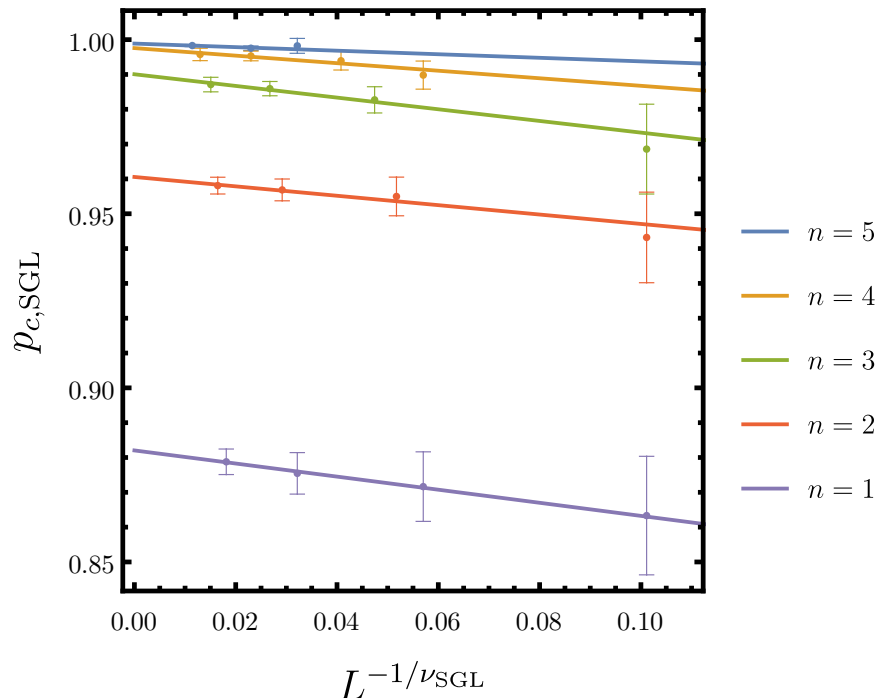


Figure 4.3: Extracting $p_{c,\text{SGL}}(n, L = \infty)$ from the linear extrapolation of the finite-size critical occupancy fractions $p_{c,\text{SGL}}(n, L)$ as a function of $L^{-1/\nu_{\text{SGL}}}$ where $\nu_{\text{SGL}} = 1.21$. The lines are linear fits, and the y-intercepts are the infinite-size limit of the critical occupancy fractions $p_{c,\text{SGL}}(n, L = \infty)$. The error bars are 95% confidence intervals.

We find that the critical occupancy fraction $p_{c,\text{SGL}}(n, L = \infty)$ approaches 1 as n increases while the critical volume fraction $\phi_{c,\text{SGL}}(n, L = \infty)$ approaches 0 [following the relation in Eq. (4.4)], indicating that these disordered fractal structures exhibit rigidity at vanishing volume fractions. These results are shown in Table 4.1.

¹The error bar in small system size is rather wide compared to large system sizes, since in lattice model the discrete filling/diluting of sites leads to larger gap in occupation fraction p , which introduces more fluctuation for $p_{c,\text{SGL}}$.

n	$p_{c,\text{SGL}}(n, L = \infty)$	$\phi_{c,\text{SGL}}(n, L = \infty)$
1	0.882 ± 0.002	0.800 ± 0.002
2	0.961 ± 0.004	0.708 ± 0.003
3	0.990 ± 0.004	0.561 ± 0.002
4	0.998 ± 0.004	0.428 ± 0.002
5	0.999 ± 0.005	0.322 ± 0.002

Table 4.1: The critical occupancy and volume fractions for the SGL’s for $n = 1, 2, 3, 4, 5$ in the infinite system size limit, $p_{c,\text{SGL}}(n, L = \infty)$ and $\phi_{c,\text{SGL}}(n, L = \infty)$. As n increases, $p_{c,\text{SGL}}(n, L = \infty) \rightarrow 1$ and $\phi_{c,\text{SGL}}(n, L = \infty) \rightarrow 0$. The error values are 95% confidence intervals.

4.4 Interpretation

The fact that the $p_{c,\text{SGL}}(n, L = \infty)$ ’s approach 1 as n increases is a reflection of both the fragility of a single SG—for any value of n , removing any non-corner site of an SG segregates the three corners of the SG into three separate rigid clusters (Appendix 4.6.3), and the result [Eq. 4.3] that $\langle z \rangle$ approaches the critical value of 4 as n increases. The latter point reveals that the SGL is asymptotically a Maxwell lattice (i.e., lattices that satisfy $\langle z \rangle = 2d$ and are thus at the verge of mechanical instability [6, 34]) as $n \rightarrow \infty$.

These observations motivate a simplified model of the SGL—the *Triangle Plate Lattice* (TPL). The TPL is a regular triangular lattice consisting of upwards-pointing rigid triangles hinged at their tips. In other words, if we view it as a regular bond-dilution RP in a triangular lattice, the items which are being diluted are groups of three bonds which together form an upwards pointing triangle. Figure 4.4 is an example of what a diluted TPL can look like.

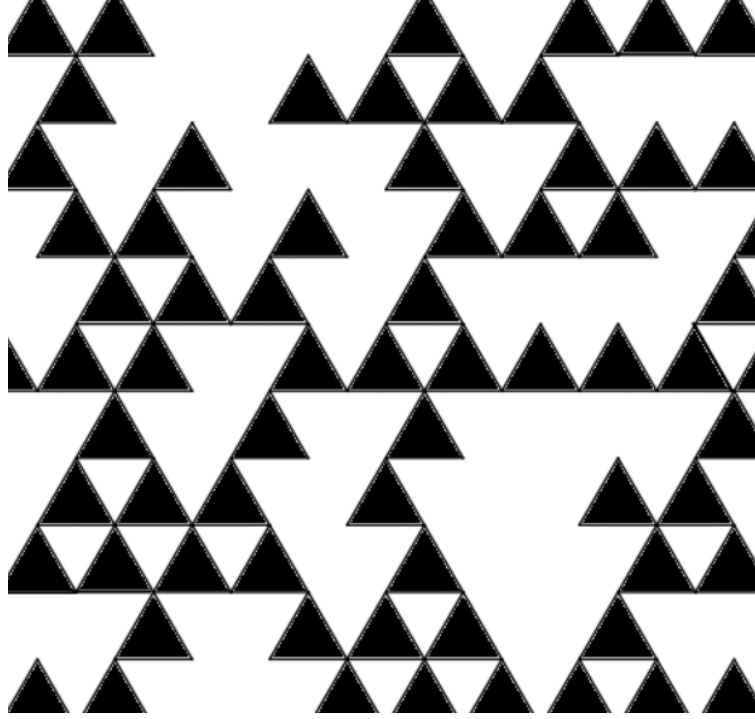


Figure 4.4: The triangular plate model (TPL) is a regular triangular lattice which has been diluted in units of upwards pointing equilateral triangles (black).

There is one main feature that separates the TPL from the SGL: in the SGL an SG with a site removed may still be an essential part of the spanning rigid cluster. In the TPL, a vacant triangle cannot transmit rigidity. Because of this difference the critical packing fraction of the TPL is used to calculate *a strict upper bound* on that of the SGL.

All p 's that follow in this section should be taken to be in the infinite system size limit. The relationship between $p_{c,\text{SGL}}$ and the critical packing fraction for the TPL $p_{c,\text{TPL}}$ is as follows: consider an SGL and a TPL, where the SG's in the SGL and the triangle plates in the TPL are the same size. Let the two lattices also be of equal size. A removed upwards pointing triangle from the TPL corresponds to *at least* one removed site from the SGL. Letting the number of triangles/SG's present in either lattice be N_Δ and the number of sites present in a single SG be $x = (3^{n+1} - 1)/2$, the critical occupancy fractions for the two lattices are related by

$$xN_\Delta(1 - p_{c,\text{SGL}}) \geq N_\Delta(1 - p_{c,\text{TPL}}). \quad (4.9)$$

The number of removed sites at the critical point in the SGL is at least the number of removed triangles at the critical point in the TPL. The “=” sign is only satisfied if removing each site from the SGL corresponds to removing a distinct triangle plate from the TPL. This is not always the case because (i) multiple removed sites in the SGL can belong to the same SG, and, as we discussed above, (ii) a “broken” SG can still contribute to the rigidity of the lattice. As a result, the TPL provides an upper bound of the critical occupancy in the SGL, $P_{c,\text{SGL}}$. Explicitly,

$$p_{c,\text{SGL}} \leq 1 - \frac{1 - p_{c,\text{TPL}}}{x} \equiv P_{c,\text{SGL}}. \quad (4.10)$$

We perform the pebble game routine on the TPL and execute the same finite scaling procedures that we did for the SGL. We find that $p_{c,\text{TPL}} = 0.656 \pm 0.005$ and $\nu_{\text{TPL}} = 1.4 \pm 0.1$. The errors given are 95% confidence intervals. $p_{c,\text{TPL}}$ and ν_{TPL} both lie within error bars of the corresponding variables for the regular triangular lattice in the case of bond dilution [1]. The upper bounds on the $p_{c,\text{SGL}}$'s predicted by the TPL are obeyed for all tested values of n and tightly obeyed for larger values of n (Fig. 4.5). It is worth pointing out that this is a strict upper bound in the sense of disorder averaged critical occupancy. It does not necessarily hold for individual samples.

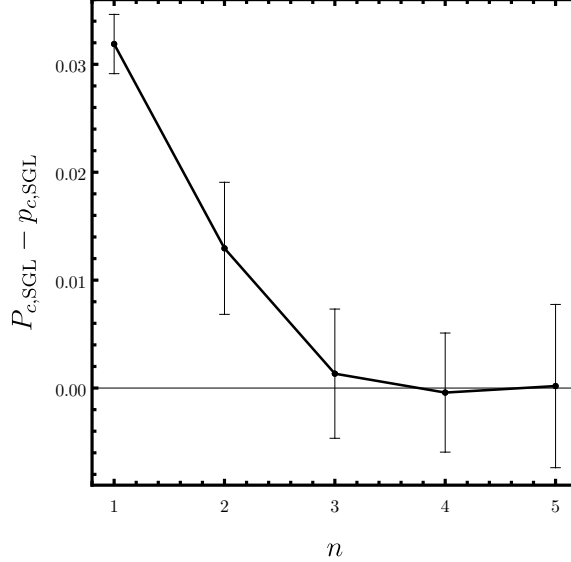


Figure 4.5: The difference between the upper bound on $p_{c,SGL}$ given by the TPL, $P_{c,SGL}$, and the measured $p_{c,SGL}$ becomes smaller as n increases. The error bars are 95% confidence intervals.

4.5 Conclusions, discussions, & extensions

In this paper we show that by introducing fractal local structures, rigidity can exist at an arbitrarily low volume fraction of solid particles. Using a periodic lattice model consisting of Sierpiński gaskets, we find that as the fractal iteration increases, the critical site occupancy fraction for rigidity increases, while the critical volume fraction decreases, allowing rigidity at progressively lower volume fractions. We also show that the RP transition in this fractal lattice remains in the same universality class as the classical RP transition when length is measured in units of the sides of the smallest triangles. We interpret this result by mapping the RP on this fractal lattice into the RP of a simple triangle plate model, based on the fragility of a single SG. This mapping gives a strict upper bound of the critical volume fraction of the fractal lattice.

Our results may shed light on the origin of rigidity in ultra-low volume fraction soft solids, such as hydrogels and aerogels. A simple way to understand this phenomena is to re-

alize that, even in a dense disordered solid such as granular matter or colloidal glass, stress is often carried by a very small fraction of the solid content, i.e., *force chains* [35, 130, 131], while other components do not significantly contribute to the elasticity. Thus, by introducing appropriate spatial correlation between the solid particles, a material can be constructed without filling the space which is not needed for rigidity. Interestingly, interactions and non-equilibrium processes (such as hydrodynamics of the solvent) occurring during the formation of these ultra-low volume fraction solids appear to naturally achieve this goal of arranging particles in very efficient ways of transmitting stress. It is of our interest to understand how this occurs in these experimental systems in the future.

The model we discuss here is a two-dimensional lattice. A curious question that immediately arises is what happens in three dimensions. The SG has a direct three-dimensional generalization: the *Sierpiński Tetrahedron* (ST), which is constructed by iteratively hinging tips of four tetrahedra together to form a bigger tetrahedra (which has an octahedron of empty space in the middle). Each face of an ST is an SG. Interestingly, there is a mechanical analogy between the SG and the ST: each internal node in the ST has six bonds, satisfying the Maxwell condition $\langle z \rangle = 2d$, while the four tip nodes each have three bonds ($z = 3$), giving rise to exactly the six trivial rigid body motions of the whole ST. Thus, each ST is isostatic in three dimensions.

These ST's can be used to construct a face-centered-cubic lattice in the same way the SG's are used to construct the SGL. This three-dimensional lattice also has a volume fraction that approaches zero as its fractal iteration increases. Analogously, in the undiluted face-centered-cubic lattice, each node at the tip of an ST has $z = 12$, taking the whole structure to $\langle z \rangle > 6$. It is straightforward to see that the undiluted ST lattice has rigidity from the rigidity of the single ST's and from the stress-bearing structures (states of self-stress along straight lines of bonds) [6, 34, 132]. Therefore, a similar RP problem can be formulated for this three-dimensional ST lattice. The nature of the RP transition may be more complicated because it is a three-dimensional problem [64], but this lattice at least

provides an example of a three-dimensional lattice where rigidity exists at an arbitrarily low volume fraction. It is also of our interest to study the RP transition in this three-dimensional lattice in the future.

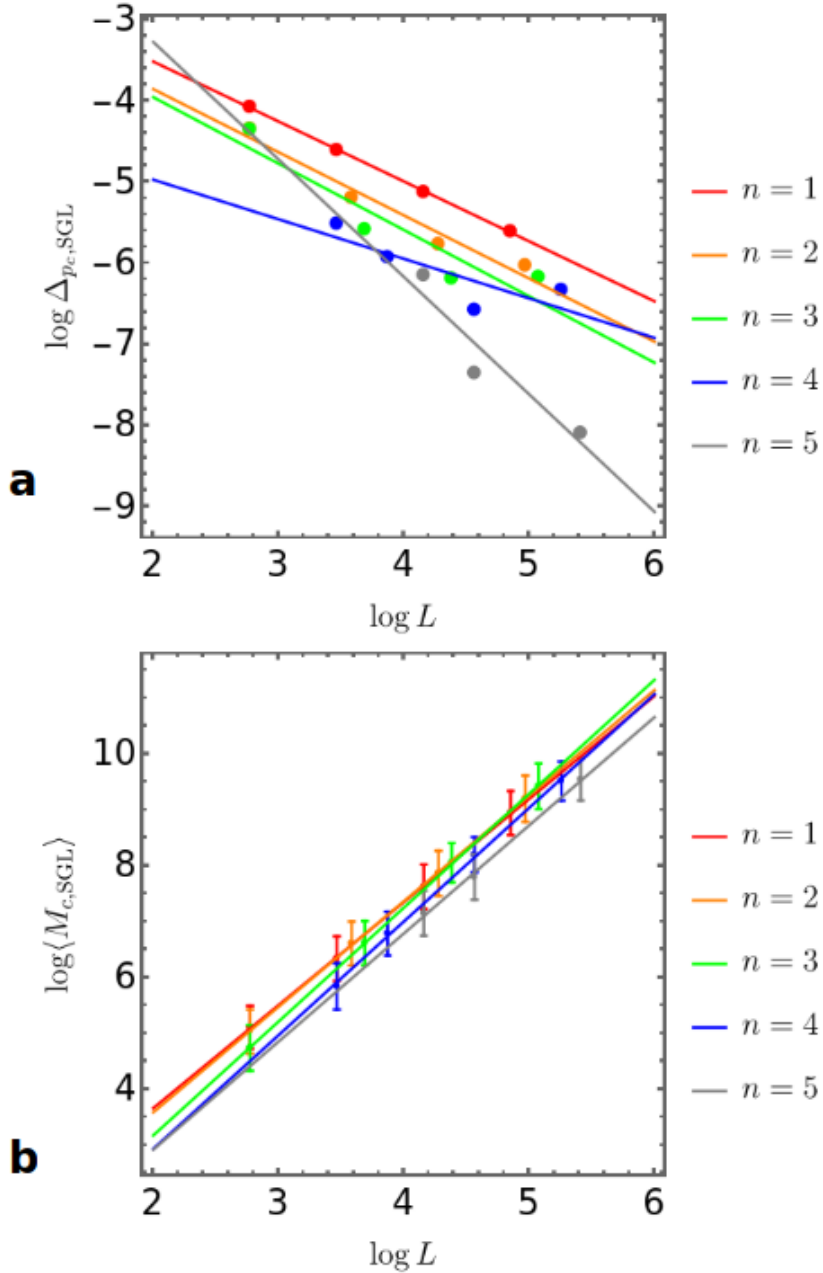


Figure 4.6: (a) The correlation length exponent ν_{SGL} and (b) the fractal dimension $d_{f, \text{SGL}}$ for the SGL are both obtained from the slopes of the linear fits for each n according to Eqs. (4.7) and (4.8). The error bars are 95% confidence intervals.

4.6 Appendices

4.6.1 Calculating ϕ_{SGL}

The volume fraction, an area fraction for $d = 2$, is the ratio of space taken up by the occupied sites to the space enclosed within the unit cell. ϕ_{SGL} is the volume fraction of the lattice, N_{occ} is the number of occupied sites in the lattice, A_v is the area covered by a single site, and A_l is the total area covered by the lattice.

$$\phi_{\text{SGL}} \equiv \frac{N_{\text{occ}} A_v}{A_l}. \quad (4.11)$$

The lattice is a rhombus with side length L , so

$$A_l = \frac{\sqrt{3}}{2} L^2. \quad (4.12)$$

Additionally, we define the occupancy fraction p_{SGL} as

$$p_{\text{SGL}} \equiv \frac{N_{\text{occ}}}{N_{\text{total}}}, \quad (4.13)$$

where N_{total} is the total number of sites (occupied and unoccupied) in the lattice. For an SGL with periodic boundary conditions, N_{total} is given by

$$N_{\text{total}} = s^2 \left(\frac{3^{n+1} - 1}{2} \right), \quad (4.14)$$

where n is the number of fractal iterations, and s is the length of the lattice in units of SG's. We set the distance between neighboring sites on the lattice to be 1. Due to the fractal structure of an SG,

$$L = s2^n. \quad (4.15)$$

Since the length between sites is 1, we also know that

$$A_v = \pi \left(\frac{1}{2} \right)^2. \quad (4.16)$$

Putting everything together,

$$\phi_{\text{SGL}} = A \frac{3^{n+1} - 1}{2^{2n}} p_{\text{SGL}}. \quad (4.17)$$

where the constant $A = \pi/4\sqrt{3}$ is specific to the geometry of the system.

4.6.2 Calculating Critical Exponents

Given the finite size scaling relations Eqs. (4.7) and (4.8), we can calculate the correlation length exponent ν_{SGL} and the fractal dimension $d_{f,\text{SGL}}$ for the SGL, as shown in Fig. 4.6.

4.6.3 Fragility of an SG

We use induction to prove that removing any non-corner site in an SG will segregate the 3 corner sites into different rigid clusters. If a corner site is removed in a free SG, the rigidity of the SG is unaffected. If a corner site is removed in an SGL, the SG's are disconnected, and may not be rigid with respect to one another.

Consider an $n = 1$ SG. It is immediate from Fig. 4.7 that our desired result holds in this case. Suppose this result holds for an n -level SG.

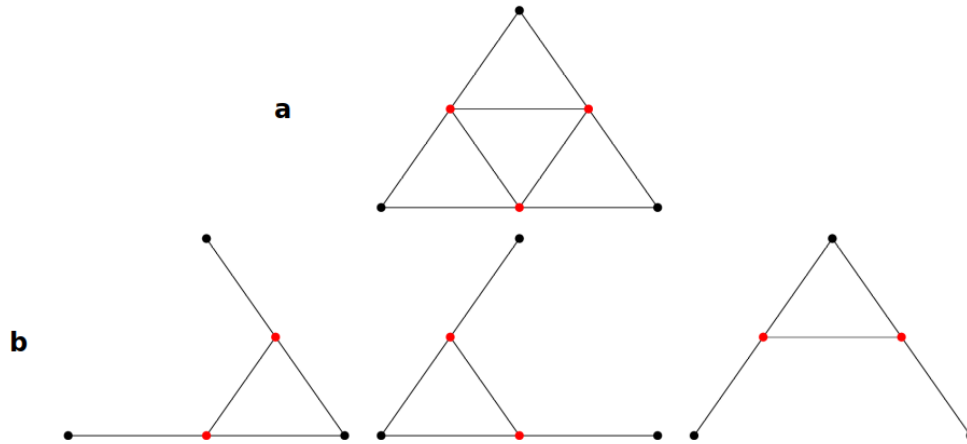


Figure 4.7: (a) An $n = 1$ SG. (b) Removing any non-corner site (red) from an $n = 1$ SG leaves two rotors attached to a rigid triangle. The triangle and both rotors (particles with only one bond) each have a corner site (black), so all three corner sites belong to distinct rigid clusters.

Consider now an SG of fractal iteration $n+1$, displayed in Fig. 4.8(a). It is composed of 3 SG's each of fractal iteration n . When any internal site of the $(n+1)$ -level SG is removed, there are two possible cases: (i) the site is a shared corner site between two n -level SG's, shown in Fig. 4.8(b), or (ii) the site is a non-corner site which belongs to a single n -level SG, shown in Fig. 4.8(c).

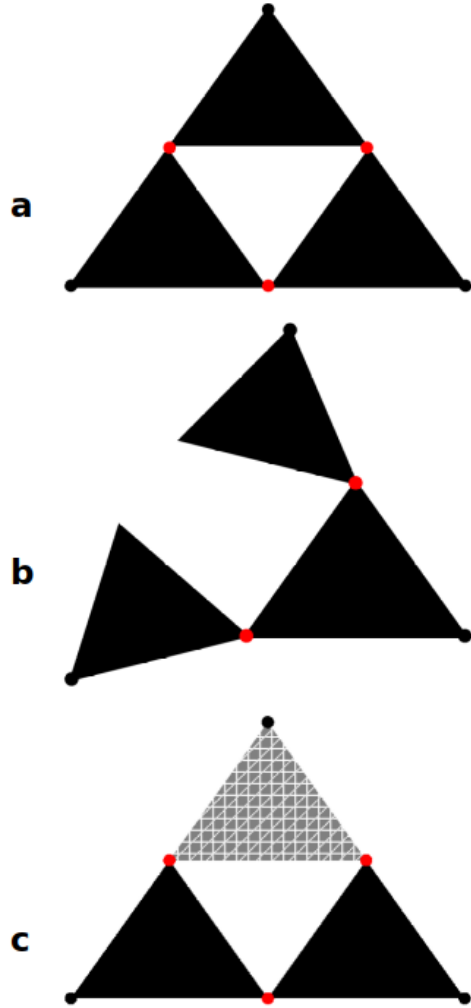


Figure 4.8: (a) An $(n + 1)$ -level SG, composed of three n -level SG's (black). (b) Case (i), a site connecting two n level SG's (red) is removed, allowing independent motion of the three corner sites (black). (c) Case (ii), a non-corner site is removed from an n -level SG (gray with white hatching). If the three corners of the n -level SG are in separate rigid clusters, the three corners of the $(n + 1)$ -level SG can move independently and are thus also in separate rigid clusters.

If (i), the two n -level SG's which were previously connected are now free to rotate about the hinges they each share with the third unaltered n -level SG. The 3 corners of the $(n + 1)$ -level SG are now in separate rigid clusters. If (ii), then the 3 corners of the n -level SG from which a site was removed are now in different rigid clusters, so they can move freely relative to each other. Since the two unaltered SG's are independently rigid, the node connecting the two unaltered SG's is a free hinge, so the three corners of the $(n + 1)$ -level

SG must be in separate rigid clusters. Since assuming our claim is true for an n -level SG implies our claim is true for an $(n + 1)$ -level SG, and the $n = 1$ case is manifestly true, for an SG of an arbitrary number of fractal iterations, removing any non-corner site will segregate the 3 corner sites of that SG into different rigid clusters. An SG is “fragile” in the sense that it has this property.

CHAPTER 5

Prestressed Elasticity of Amorphous Solids

This chapter summarizes the manuscript “*Prestressed elasticity of amorphous solids*” in preparation co-authored by Shang Zhang, Vishwas Vasisht, Ethan Stanifer, Leyou Zhang, Emanuela Del Gado and Xiaoming Mao. It is worth noting that this work is under the procedure of finalizing to publication, so it will appear to public soon with a bit more modifications and updates compared to the context in this Chapter.

5.1 Introduction

Almost all solid materials are stressed. Amorphous solids exhibit quenched residual stress from their preparation process, crystalline solids are stressed by defects and grain-boundaries, and living matter experience active stress from biological processes. The ubiquity of stressed solids is encapsulated in the fact that the stress tensor σ , as a $d \times d$ symmetrical matrix in d dimensions, has $d(d + 1)/2$ independent degrees of freedom, but the force balance equation,

$$\partial_j \sigma_{ij} = 0, \tag{5.1}$$

only poses d constraints, leaving $d(d - 1)/2$ unconstrained components in the stress field. In absence of external load, all components have to vanish if the material, and the stress field, have to be homogeneous, but they can be nonzero at lengthscales over which heterogeneities or excess constraints are present, giving rise to *prestress*, (also known as “residual

stress”, “initial stress” or “eigenstress” in different contexts) [133].

In structural engineering, prestress is proactively used to modify both stability and load bearing capability of structures, from prestressed reinforced concrete to tensegrity architectures (Fig. 5.1). In materials, instead, prestresses can emerge spontaneously during solidification, as the direct consequence of out-of-equilibrium processes through which they form, or of the external load applied during processing. Prominent examples include isotropic compressive prestress in jammed packings, shear prestress in shear jammed granular matter and shear thickened dense suspensions, isotropic prestresses in glasses, and rich varieties of anisotropic prestress fields in prestressed/tensegrity metamaterials [134–138] and biological systems [139, 140]. Remarkably, very much in the same way as for buildings and large scale structures, microscopic residual stresses in amorphous solids may strongly affect their strength—stiffen or soften them, and direct how they fail [133]. In addition, prestress stores elastic energy in materials, featuring a different energy landscape when compared to stress-free materials.

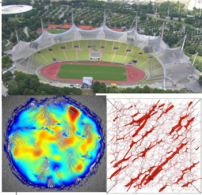
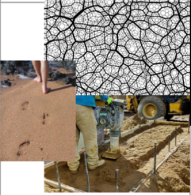
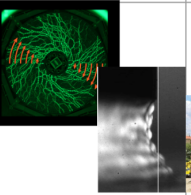

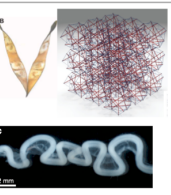
Mode of stress	Tensile	Compression	Shear	Competing tension and compression	Complex anisotropic
Examples	Tensile architectural structures Gel networks under tension Tissue	Jamming of repulsive particles Compressed soil or sand	Shear jamming of granular matter, shear thickening of dense suspensions	Prestressed concrete, Rupert's drop Gorilla glass	Morphogenesis, Prestressed metamaterials
Figure					
Effects	Stiffening	Stabilizing/destabilizing	Stabilizing/destabilizing	Fracture resistance	Morphology and functions

Figure 5.1: Prestress in structural engineering and materials science.

A deep understanding of the consequences of prestress is therefore key to predict elas-

ticity and material properties in general, but microscopic prestresses can be very elusive, since it is difficult to directly access them in experiments and in most cases only their indirect consequences can be detected. It has been shown that in jamming of frictionless particles, compressive prestress both stabilizes the packing by maintaining particle contacts, and destabilizes it by shifting frequencies of vibrational modes [141, 142], as well as controlling the response to external forces [143]. In biological systems such as biopolymer gels and epithelial cell sheets, tensile stress has been shown to provide stability [144–147], and active stress generated by molecular motors has been shown to give rise to sophisticated effects on rigidity [148] and mechanical signal transmission [149].

However, a general theoretical framework to disentangle effects of microstructure and prestress, and map how external load is carried by prestressed amorphous solids, is still missing. Current studies of elasticity of amorphous solids have mainly focused on determining how the disorder in their microstructure affects elasticity, whereas the role of prestress is far less understood, so that there is a gap in the theoretical approaches that can rationalize the mechanics of amorphous solids when it comes to prestress.

In particular, it was pointed out in the seminal work of Edwards [150] and further characterized in Refs [151–155], that prestress in disordered solids exhibit degenerate states given the same configuration, comprising a “force network ensemble”, which evolves under external load, and in turn affects the evolution of configurations. Interesting statistical relations of prestress distributions within this type of ensembles have been recently studied, where force-balance constraints [Eq. (5.1)] led to intriguing long-range correlations [156–161]. However, unraveling the role of disordered configurations and disordered prestress on the mechanical properties of amorphous solids has been difficult both conceptually and computationally.

Here we present a systematic method based on the concept of *states of self stress* (SSSs) to investigate how prestress affects the mechanical response of amorphous solids, where the configuration and the prestress are allowed to change *independently*, while force-balance

is always maintained. The concept of states of self stress [4, 162] captures eigenstates of stress distributions that leave all components of a solid structure in force balance. In discrete mechanical networks, SSSs originate from redundant constraints. SSSs were first introduced in the mechanical engineering community to describe load bearing abilities of structures, and more recently introduced to the condensed matter community for their special role in characterizing mechanical topological edge states [6, 33, 34, 163]. Because SSSs span the linear space of all possible ways a system can carry load, mapping out, and further programming this SSSs linear space, offers a convenient handle to control the mechanical response of materials. Interesting examples of this type include recent work on programming SSSs using topological mechanics to direct buckling and fracturing of metamaterials [132, 164]. Intriguingly, SSSs in jammed packings have been shown to exhibit rich spatial structures and a divergent length scale near jamming [69].

The general method we introduce here is applicable to a wide range of systems, both ordered and disordered, where prestress affects elasticity. It provides an efficient computational algorithm for finding the stress distribution when the system is under any load, as well as offering a platform to develop field-theoretic treatment of prestressed elasticity of amorphous solids. Because this method allows the microstructure and the prestress field to vary separately, it offers a pathway to investigate how amorphous solids *evolve as well as develop memory under stress without changing their configuration*.

We demonstrate this method using a triangular lattice model with varying prestress, and also test this method in amorphous configuration of compressed repulsive particles, as a model for a colloidal soft solid, obtained through numerical simulations. We show how prestress determines the response of such model solid to both macroscopic shear strain and local dipole forces, where they display qualitatively different behaviors from un-stressed spring networks with the same geometry. We also use this method to study the dependence of the stress-bearing ability of the system on the preparation protocol, which changes the microscopic prestress distribution, as well as signatures of the spatial evolution of stress

under strain.

Overall, the new method proposed here is an ideal candidate to investigate the nature of rigidity transitions in prestressed systems, and furthermore, yielding and shear thickening/thinning systems such as granular matter, jammed and dense suspensions, to potentially shed new light on the dynamical interplay between stress and geometry in these complex materials.

5.2 Prestressed mechanical networks

In this section we briefly review mechanics of prestressed networks and their continuum elasticity limit.

5.2.1 Prestressed networks

We consider a discrete network of point-like particles connected by pairwise central-force potentials (bonds). When this network is deformed, particle ℓ , which was originally at $\vec{R}_{\ell,0}$ in the reference state, undergoes a displacement \vec{u}_ℓ to a new position

$$\vec{R}_\ell = \vec{R}_{\ell,0} + \vec{u}_\ell. \quad (5.2)$$

The change of the elastic energy V_b of a bond b connecting particles ℓ, ℓ' is

$$\delta V_b = V_b(|\vec{R}_b|) - V_b(|\vec{R}_{b,0}|), \quad (5.3)$$

where $\vec{R}_{b,0} \equiv \vec{R}_{\ell,0} - \vec{R}_{\ell',0}$, $\vec{R}_b \equiv \vec{R}_\ell - \vec{R}_{\ell'}$ are the vectors along the bond in the reference state and the deformed state respectively.

This change in energy can be expanded to quadratic order in u [using Eq. (5.2) in (5.3)]

as

$$\delta V_b = \frac{V_b''}{2} |e_b^\parallel|^2 + \frac{V_b'}{2|\vec{R}_{b,0}|} |e_b^\perp|^2, \quad (5.4)$$

where the derivatives are taken at $|\vec{R}_{b,0}|$,

$$\vec{e}_b \equiv \vec{u}_\ell - \vec{u}_{\ell'} \quad (5.5)$$

is the difference of displacement vectors of the two particles connected by bond b , and

$$e_b^\parallel \equiv \hat{R}_{b,0} \hat{R}_{b,0} \cdot \vec{e}_b, \quad e_b^\perp \equiv (\mathbb{I} - \hat{R}_{b,0} \hat{R}_{b,0}) \cdot \vec{e}_b \quad (5.6)$$

are its components parallel and perpendicular to the original bond direction $\hat{R}_{b,0} \equiv \vec{R}_{b,0}/|\vec{R}_{b,0}|$, respectively.

The derivatives of this potential,

$$\begin{aligned} V_b''(|\vec{R}_b|) &\equiv \frac{d^2 V_b(|\vec{R}_b|)}{d|\vec{R}_b|^2} = k_b, \\ V_b'(|\vec{R}_b|) &\equiv \frac{dV_b(|\vec{R}_b|)}{d|\vec{R}_b|} = t_{b,p}, \end{aligned} \quad (5.7)$$

correspond to the spring constant k_b and the pre-tension $t_{b,p}$ (tension of the bond in the reference state) of bond b . In this paper we consider the case when the bonds are simple harmonic springs,

$$V_b(|\vec{R}_b|) = \frac{k_b}{2} (|\vec{R}_b| - R_{b,R})^2, \quad (5.8)$$

where $R_{b,R}$ is the rest length of bond b . In this case, k_b is a constant, and

$$t_{b,p} = k_b (|\vec{R}_{b,0}| - R_{b,R}). \quad (5.9)$$

In a stress-free network, all bonds are at their rest length $R_{b,R}$ and thus $V_b'(|\vec{R}_{b,0}|) = 0$, leaving only the V_b'' term in Eq. (5.4). Vibrational modes of disordered networks of this

type have been extensively studied, yielding a rich set of interesting phenomena including quasilocalized modes, anomalies of density of states at low frequencies, etc.

When a network is stressed, $V'_b(|\vec{R}_{b,0}|) \neq 0$, and both terms contribute to the elastic energy, increasing the number of constraints, as we discuss in detail in Sec. 5.3. Interestingly, the sign of t_b can be either positive (tension) or negative (compression). In the case of $t_b > 0$, the prestress term contribute another complete square term in the elastic energy, clearly stabilizing the system. In the case of $t_b < 0$, naively, the prestress term appears to be unstable. However, because e_b^\perp are not variables independent of e_b^\parallel , the stability of the network need to be analyzed for the collective modes, which we discuss more in Sec. 5.2.3.

Here we assumed that the network is in *force balance*, i.e., the total force on each particle vanishes. As a result there is no $\mathcal{O}(e)$ terms in the expansion. Note that *the force-balance condition and the stress-free condition are two distinct conditions*, where the later means $V'_b(|\vec{R}_{b,0}|) = 0$ on all bonds, and is a much more stringent requirement than the force-balance condition. We will revisit this distinction in continuum elasticity in Sec. 5.2.2.

5.2.2 Continuum elasticity with prestress

The discrete theory discussed above can be rigorously linked to continuum elasticity using the relation between the discrete nonlinear strain v_b of bond b defined as [165, 166]

$$v_b \equiv \frac{1}{2} \left(|\vec{R}_b|^2 - |\vec{R}_{b,0}|^2 \right) \quad (5.10)$$

and the (continuum) nonlinear strain tensor (repeated indices are summed over)

$$\epsilon_{ij}(\vec{x}) \equiv \frac{1}{2} (\partial_i u_j + \partial_j u_i + \partial_i u_l \partial_l u_j) \quad (5.11)$$

where the relation reads

$$v_b = \vec{R}_{b,0} \cdot \epsilon_{ij}(\vec{x}) \cdot \vec{R}_{b,0}. \quad (5.12)$$

This follows from the definition of the nonlinear strain tensor, and we have taken the continuum limit by assuming the spatial variation of the strain field is slow compared to the scale of the particles and bonds, so the deformation of bond b is determined by the strain at its location \vec{x} .

Using the expansion of bond length in terms of v_b ,

$$|\vec{R}_b| = |\vec{R}_{b,0}| \left[1 + \frac{v_b}{|\vec{R}_{b,0}|^2} - \frac{v_b^2}{2|\vec{R}_{b,0}|^4} + \mathcal{O}\left(\frac{v_b}{|\vec{R}_{b,0}|^2}\right)^3 \right] \quad (5.13)$$

we can rewrite the expansion of elastic energy of bond b as

$$\delta V_b = V'_b \frac{v_b}{|\vec{R}_{b,0}|} + \frac{1}{2} \left(V''_b - \frac{V'_b}{|\vec{R}_{b,0}|} \right) \left(\frac{v_b}{|\vec{R}_{b,0}|} \right)^2. \quad (5.14)$$

This is equivalent to the expansion in Eq. (5.4), by recognizing that

$$v_b = \vec{R}_{b,0} \cdot \vec{e}_b + \frac{1}{2} \vec{e}_b \cdot \vec{e}_b = |\vec{R}_{b,0}| e_b^\parallel + \frac{(e_b^\parallel)^2 + (e_b^\perp)^2}{2}. \quad (5.15)$$

The combination of Eqs. (5.12) and (5.14) allows us to write the bond energy change in terms of the strain tensor.

The elastic energy of the whole system can be taken to the continuum limit by converting the sum over all bonds to an integral over space

$$E = \frac{1}{2} \sum_{\ell} \sum_{\ell'} V_{b=\langle \ell, \ell' \rangle} = \frac{1}{2} \int d^d \vec{x} \frac{1}{v(\vec{x})} \sum_{\ell'} V_{b=\langle \ell, \ell' \rangle} \quad (5.16)$$

where the space is Voronoi tessellated according to the particles, and $v(\vec{x})$ is the volume of the Voronoi cell at \vec{x} , and the overall factor of $1/2$ comes from the fact that every bond is counted twice. The sum $\sum_{\ell'}$ in the continuum limit represent the sum over the bonded neighbors of the particle at \vec{x} . Using this formulation, the elastic energy of the system can

be written in the conventional form

$$E = \int d^d \vec{x} \left[\frac{1}{2} K_{ijkl}(\vec{x}) \epsilon_{ij}(\vec{x}) \epsilon_{ij}(\vec{x}) + \sigma_{p,ij}(\vec{x}) \epsilon_{ij}(\vec{x}) \right] \quad (5.17)$$

where the local elastic-modulus tensor $K_{ijkl}(\vec{x})$ and prestress field $\sigma_{p,ij}(\vec{x})$ are determined from the discrete network by

$$\begin{aligned} K_{ijkl}(\vec{x}) &= \frac{1}{2v(\vec{x})} \sum_{\ell'} \left(V_b'' |\vec{R}_{b,0}|^2 - V_b' |\vec{R}_{b,0}| \right) \\ &\quad \cdot \hat{R}_{b,0,i} \hat{R}_{b,0,j} \hat{R}_{b,0,k} \hat{R}_{b,0,l}, \\ \sigma_{ij}(\vec{x}) &= \frac{1}{2v(\vec{x})} \sum_{\ell'} (V_b' |\vec{R}_{b,0}|) \hat{R}_{b,0,i} \hat{R}_{b,0,j}. \end{aligned} \quad (5.18)$$

From this relation, it is clear that the prestress field $\sigma_p(\vec{x})$ in the continuum theory comes from pretensions on bonds which are not at their rest length in the discrete network, whereas the elastic-modulus tensor depends on both the spring constants and the tensions.

The body-force in this continuum theory

$$f_i(\vec{x}) = \partial_j \sigma_{p,ij}(\vec{x}) = \frac{1}{2v(\vec{x})} \sum_{\ell'} (V_b' |\vec{R}_{b,0}|) \hat{R}_{b,0,i} \quad (5.19)$$

corresponds to the total force on each particle (normalized by the volume of the Voronoi cell) in the discrete network. Thus, the force-balance conditions in the discrete network and the continuum theory are indeed the same condition.

It is often useful to write this continuum theory in a quadratic expansion in terms of the displacement field $\vec{u}(\vec{x})$,

$$\begin{aligned} E &= \int d^d \vec{x} \left[\frac{1}{2} K_{ijkl}(\vec{x}) \partial_i u_j(\vec{x}) \partial_j u_i(\vec{x}) \right. \\ &\quad \left. + \sigma_{p,ij}(\vec{x}) \partial_i u_l(\vec{x}) \partial_j u_l(\vec{x}) \right] \end{aligned} \quad (5.20)$$

where we have used the symmetry of K_{ijkl} and the force balance condition which eliminates $\mathcal{O}(u)$ terms in this elastic energy.

5.2.3 Prestressed rigidity

The concept of “rigidity” has been a central theme in the discussion of mechanics of soft materials. In general, rigidity can be interpreted from two viewpoints, (i) a microscopic view point, where rigidity is attributed to the vanishing of floppy modes (i.e. modes of deformation that cost to elastic energy), and (ii) a macroscopic viewpoint, where rigidity is attributed to the emergence of a spanning rigid cluster that can transmit stress. Remarkably, these two rigidity criteria coincide for the jamming transition of frictionless repulsive particles.

In this section we focus on the first viewpoint and discuss how prestress changes floppy modes. In Sec. 5.3 we discuss how prestress affects the ability of the system to carry additional load (second point of view).

Rigidity of stress-free discrete mechanical networks is often analyzed via the comparison between the numbers of constraints and degrees of freedom [2]. This is well summarized by the Maxwell-Callandine index theorem [4, 163]. Rigorously speaking, when this theorem determines that the number of floppy modes of a system vanishes, it implies that the system is “first-order rigid”, where the energy increases quadratically for all deformations. By contrast, in a “second-order rigid” system the the leading order expansion of the energy with respect to some deformations is of higher order such as cubic or quartic [167, 168].

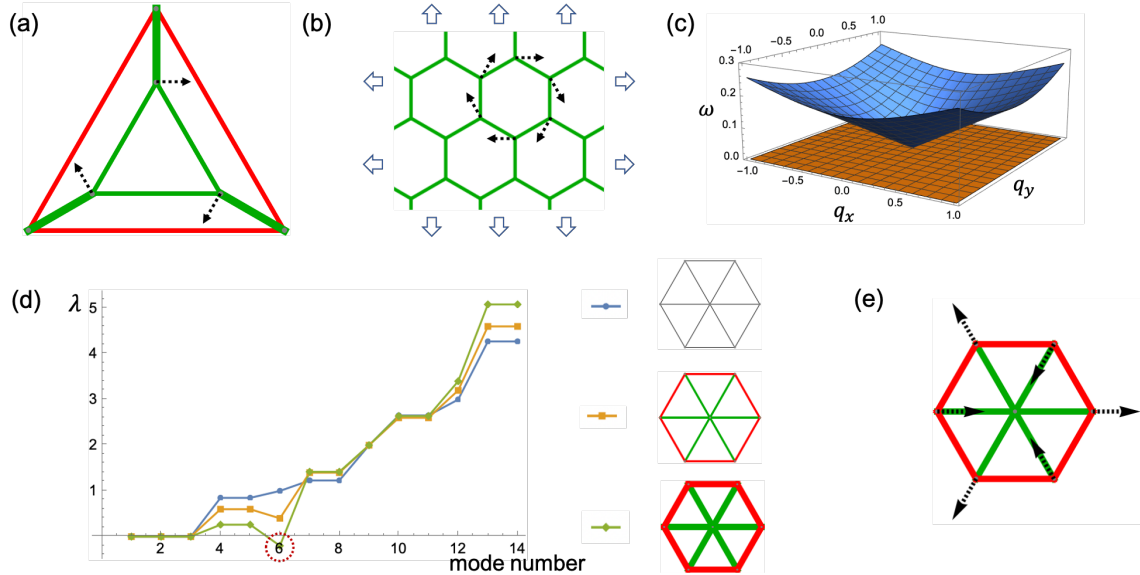


Figure 5.2: Prestressed rigidity. (a) A mechanical network of concentric similar triangles. When stress-free, this network has one floppy mode. When prestressed, this floppy mode is eliminated. Black dashed arrows denote the floppy mode. Green (red) bonds are under tension (compression). The thickness of the bond is proportional to the magnitude of the prestress. (b) A honeycomb lattice exhibits an extensive number of floppy modes. When prestressed (equal tension on all bonds), these floppy modes are eliminated. (c) Phonon dispersion relation of the honeycomb lattice when stress-free (orange) and when stretched with tensile prestress (blue). (d) Eigenvalues of the dynamical matrix of a mechanical network (right). When prestress on the network increase beyond a threshold, one normal mode (e) becomes unstable.

How does prestress change this paradigm of rigidity? It was pointed out in Ref. [167, 168] that prestress can rigidify second-order rigid systems and make all their modes first-order rigid. Interestingly, this prestress stabilization effect can even take place in systems which are underconstrained by (stress-free) Maxwell counting. One simple example is the honeycomb lattice, which has coordination number $z = 3$ and thus significantly below the Maxwell point of $z = 2d$ (here d is the spatial dimension) where degrees of freedom and constraints balance. When a honeycomb lattice is under tension, all modes are lifted to finite frequency (except for trivial translations). It is worth noting that this example does not violate the theorems in Ref. [168]: although underconstrained, floppy modes of the honeycomb lattice under periodic boundary conditions are in fact second order rigid. In

Fig. 5.2 we show examples of how networks become rigid by prestress.

This effect has studied in various disordered mechanical networks from polymer gels to jamming of particles and biological tissues [144, 146, 169–171]. In these models, the underconstrained network typically exhibit an extensive number of floppy modes before the application of stress. When certain types of strain (tensile or shear) is applied to the network, a system spanning SSS emerges and becomes stressed, providing (macroscopic) rigidity and thus elastic moduli. This prestress also rigidifies floppy modes in the network, as the geometry of the network evolves and these modes become second order rigid.

Interestingly, by increasing the magnitude of the prestress, a stable network can also destabilize. This happens when the negative terms in Eq. (5.4) due to compressed bonds compete with the positive terms and creates negative eigenvalues in the dynamical matrix. Some examples of this effect is also shown in Fig. 5.2. We discuss this effect in more detail in Sec. 5.3.2.

5.3 States of self-stress in stressed elasticity

In this section we introduce a new $\mathbb{Q} \cdot \mathbb{C}$ (equilibrium and compatibility) decomposition for the mechanics of prestressed systems, that can be used to analyze their SSSs and zero modes (ZMs). We first briefly review this decomposition for stress-free systems, and then discuss the more general case of prestressed systems. We also develop general formulation of using these SSSs to compute mechanical response of a system to external load, including both macroscopic strain and local forces.

5.3.1 States of self-stress in stress-free systems

The elastic energy of a stress-free network of N point-like particles connected by N_b central-force springs in d dimensions can be written to quadratic order in u using the dy-

dynamical matrix \mathbb{D}^{\parallel} as

$$E = \sum_{b=1}^{N_b} \delta V_b = \sum_{b=1}^{N_b} \frac{k_b}{2} (e_b^{\parallel})^2 = \frac{1}{2} \langle u | \mathbb{D}^{\parallel} | u \rangle \quad (5.21)$$

where the inner product is taken in the $N \cdot d$ dimensional space for particle displacements u , and the superscript “ \parallel ” on the dynamical matrix signifies that this dynamical matrix describes a stress-free system where only e^{\parallel} enters the elastic energy. The more general form for prestressed systems will be discussed in Sec. 5.3.2. This quadratic form can be decomposed into two steps using the equilibrium and compatibility matrices, defined as

$$\mathbb{C}^{\parallel} |u\rangle = |e^{\parallel}\rangle \quad (5.22)$$

$$\mathbb{Q}^{\parallel} |t^{\parallel}\rangle = |f\rangle. \quad (5.23)$$

Here $|e^{\parallel}\rangle$ and $|t^{\parallel}\rangle$ represent the extension and tension of every bond (where the superscript “ \parallel ” on means that they are along the bond direction), which are both N_b dimensional vectors. $|u\rangle$ and $|f\rangle$ represent the displacement and total force on every site, which are both Nd dimensional vector. As a result, the equilibrium matrix \mathbb{Q} has the dimension $Nd \times N_b$, and the compatibility matrix \mathbb{C} has the dimension $N_b \times Nd$.

Using these relations in Eq. (5.21) it is straightforward to see that

$$\mathbb{D}^{\parallel} = \mathbb{Q}^{\parallel} \cdot \mathbb{K}^{\parallel} \cdot \mathbb{C}^{\parallel} \quad (5.24)$$

where \mathbb{K}^{\parallel} is a diagonal matrix that contains all the spring constants k_b .

The null space of the \mathbb{Q}^{\parallel} is the set of tensions, called SSSs, that produce no forces at any site,

$$0 = \mathbb{Q}^{\parallel} |t_{\text{SSS}}^{\parallel}\rangle. \quad (5.25)$$

The null space of the \mathbb{C}^{\parallel} is the set of site displacements, called ZMs, that produce no changes in bond lengths,

$$0 = \mathbb{C}^{\parallel}|u_{\text{ZM}}\rangle. \quad (5.26)$$

ZMs have been extensively studied in soft matter systems, due to their obvious significance as capturing deformations with no cost of elastic energy. SSSs have only recently been explored in soft matter, but also show great potential in characterizing stress-bearing structures in mechanical networks.

Applying rank-nullity theorem on \mathbb{Q}, \mathbb{C} matrices leads to the Maxwell-Calladine index theorem

$$N_0 - N_S = Nd - N_b, \quad (5.27)$$

where N_0, N_S are the numbers of ZMs and SSSs.

These concepts have found wide applications recently in the new field of topological mechanics, as $t_{\text{SSS}}^{\parallel}$ and u_{ZM} can become topologically protected modes in Maxwell lattices and networks.

5.3.2 States of self-stress and zero modes in prestressed systems

Prestress of a mechanical network can always be viewed as “exciting” an existing SSS in a stress-free network (which is generated by turning off stress in the prestressed network but keeping exactly the same geometry). Thus, the “stress-free version” of a prestressed network must exhibit a SSS in the first place.

With prestress, the elastic energy includes both e_b^{\parallel} and e_b^{\perp} terms as we analyzed in

Eq. (5.4),

$$\begin{aligned}
E &= \sum_{b=1}^{N_b} \delta V_b = \sum_{b=1}^{N_b} \left[\frac{k_b}{2} (e_b^{\parallel})^2 + \frac{t_{b,p}}{2|\vec{R}_{b,0}|} |e_b^{\perp}|^2 \right] \\
&= \frac{1}{2} \langle u | (\mathbb{D}^{\parallel} + \mathbb{D}^{\perp}) | u \rangle.
\end{aligned} \tag{5.28}$$

Similar to the stress-free case, using the fact that this elastic energy consist only complete square terms, this dynamical matrix can also be decomposed into \mathbb{Q}, \mathbb{C} matrices,

$$\mathbb{D} = \mathbb{Q} \cdot \mathbb{K} \cdot \mathbb{C}, \tag{5.29}$$

where

$$\mathbb{C} |u\rangle = \begin{pmatrix} e^{\parallel} \\ e^{\perp} \end{pmatrix} \equiv |e\rangle, \tag{5.30}$$

defines the new \mathbb{C} matrix and $\mathbb{Q} = \mathbb{C}^T$. Here we have defined the new $N_b d$ dimensional e vector which contains one component from \parallel and $d - 1$ from \perp for each of the N_b bonds. It is worth noting here that the compatibility matrix \mathbb{C} is now $N_b d \times Nd$ dimensional instead of $N_b \times Nd$ dimensional, because this \mathbb{C} matrix maps the Nd dimensional displacement vector of the network into e_b^{\parallel} and e_b^{\perp} for each bond b . At the same time, the equilibrium matrix \mathbb{Q} is $Nd \times N_b d$ dimensional. The spring constant matrix is a $N_b d \times N_b d$ diagonal matrix with spring constant k_b for the \parallel terms and pre-stress $t_{b,p}$ for the \perp terms,

$$\mathbb{K} = \begin{pmatrix} k_b & 0 \\ 0 & \frac{t_{b,p}}{|\vec{R}_{b,0}|} \end{pmatrix} \tag{5.31}$$

These new \mathbb{Q}, \mathbb{C} still describes the mapping between the (Nd dimensional) degrees of freedom space and the ($N_b d$ dimensional) constraint space. In parallel with Eq. (5.30) we

have

$$\mathbb{Q} \begin{pmatrix} t^{\parallel} \\ t^{\perp} \end{pmatrix} \equiv \mathbb{Q}|t\rangle = |f\rangle \quad (5.32)$$

Correspondingly, t^{\parallel} and t^{\perp} are the parallel and perpendicular components of t .

It might appear confusing how tension t on a central-force spring can have a component perpendicular to the spring. This can be understood by realizing that the \parallel and \perp components are defined with respect to the reference configuration, and t denotes an increment of stress on top of the pre-stress t_p . In the prestressed reference state, $t_{b,p}$ is along bond b in the reference configuration $\vec{R}_{b,0}$. In the state after the (infinitesimal) deformation, the total tension is along bond b in the deformed configuration \vec{R}_b . These two bond directions, $\vec{R}_{b,0}$ and \vec{R}_b , are not parallel in general. The t field in Eq. (5.32) represents the increment from the pre-tension to the tension after the deformation, and thus has components parallel and perpendicular to the original bond direction. In other words, under an (infinitesimal) deformation, both bond (parallel) extension e^{\parallel} and bond rotation e^{\perp} cause increment of stress [Eq. (5.28)], and the two components are t^{\parallel} and t^{\perp} respectively.

SSSs in a prestressed system are thus defined as any vectors that satisfy

$$\mathbb{Q}|t_{\text{SSS}}\rangle = \mathbb{Q} \begin{pmatrix} t_{\text{SSS}}^{\parallel} \\ t_{\text{SSS}}^{\perp} \end{pmatrix} = |f\rangle = 0, \quad (5.33)$$

which parallel and perpendicular change of bond tensions that leave all particles in force balance (SSSs), respectively, for a prestressed network. In Fig. 5.3 we show two examples of mechanical networks where prestress introduces extra SSSs that involve t^{\perp} components. This formulation characterizes the tensegrity phenomena where prestress generates new SSSs for the system to carry other types of load.

For the tensegrity T3 prism structure in Fig. 5.3, (g) corresponds to the SSS which only has non-zero components in \parallel directions, and is also the single SSS in the stress-free

structure. Fig. 5.3(h) is the SSS which has the top and bottom triangle twisted in reverse directions, producing rotational tensions balanced with \parallel bond tensions and induces no net force on sites.

One can also define ZMs in a prestressed network as

$$\mathbb{C}|u_{\text{ZM}}\rangle = \begin{pmatrix} e^{\parallel} \\ e^{\perp} \end{pmatrix} = |e\rangle = 0, \quad (5.34)$$

and further rewrite the Maxwell-Calladine index theorem for a stressed network by applying the rank-nullity theorem on the new \mathbb{Q}, \mathbb{C} matrices, which reads

$$N_0 - N_S = Nd - N_b d. \quad (5.35)$$

Note that the last term is now $N_b d$ for the prestressed network instead of N_b in the stress-free case. More rigorously, if we include the effect that not all bonds are stressed, this index theorem should be written as

$$N_0 - N_S = Nd - N_b^{\text{unstressed}} - N_b^{\text{stressed}} d. \quad (5.36)$$

where each unstressed bonds only provide 1 constraint.

However, actual mechanics of the network is more complicated. Because some spring constants in \mathbb{K} are negative (from compressively prestressed bonds), new ZMs may arise, as we show in the example in Fig. 5.2. Thus, satisfying $\mathbb{C}|u_{\text{ZM}}\rangle = 0$, which guarantees no bonds extend or rotate, is a sufficient but not necessary condition for ZMs.

In other words, there are two types of ZMs in a prestressed system. The first type satisfies Eq. (5.34) and are also ZMs of the stress free network with the same geometry (with the additional no-rotation constraint). The second type are new ‘‘fine-tuning’’ ZMs, where positive and negative terms in the dynamical matrix balance, and these modes are not ZMs of the stress-free network. Interestingly, because $\mathbb{C}|u_{\text{ZM}}\rangle \neq 0$ and $\mathbb{Q}\mathbb{K}\mathbb{C}|u_{\text{ZM}}\rangle = 0$

these ZMs lead to a set of SSSs $|t_{\text{SSS}}\rangle = \mathbb{K}\mathbb{C}|u_{\text{ZM}}\rangle$. One trivial example of this type of ZMs is the rigid rotation of the network if the system is under open boundary conditions: the rotation causes e^\perp and thus not satisfying Eq. (5.34), but it is indeed a ZM of the dynamical matrix. A nontrivial example of such fine tuning ZM is shown in Fig 5.2a where the sum of e^\parallel and e^\perp terms vanish. The Maxwell-Calladine index theorem for prestressed systems [Eq. 5.3.2] works for the case when only the first type of ZMs are counted.

In contrast, the definition of SSSs in Eq. (5.33) is more robust as it relies only on force balance, and is not affected by the positive definiteness of \mathbb{D} . In our discussions below, we mainly focus on these SSSs and show how they form a linear space that efficiently characterizes how load is carried by a prestressed system.

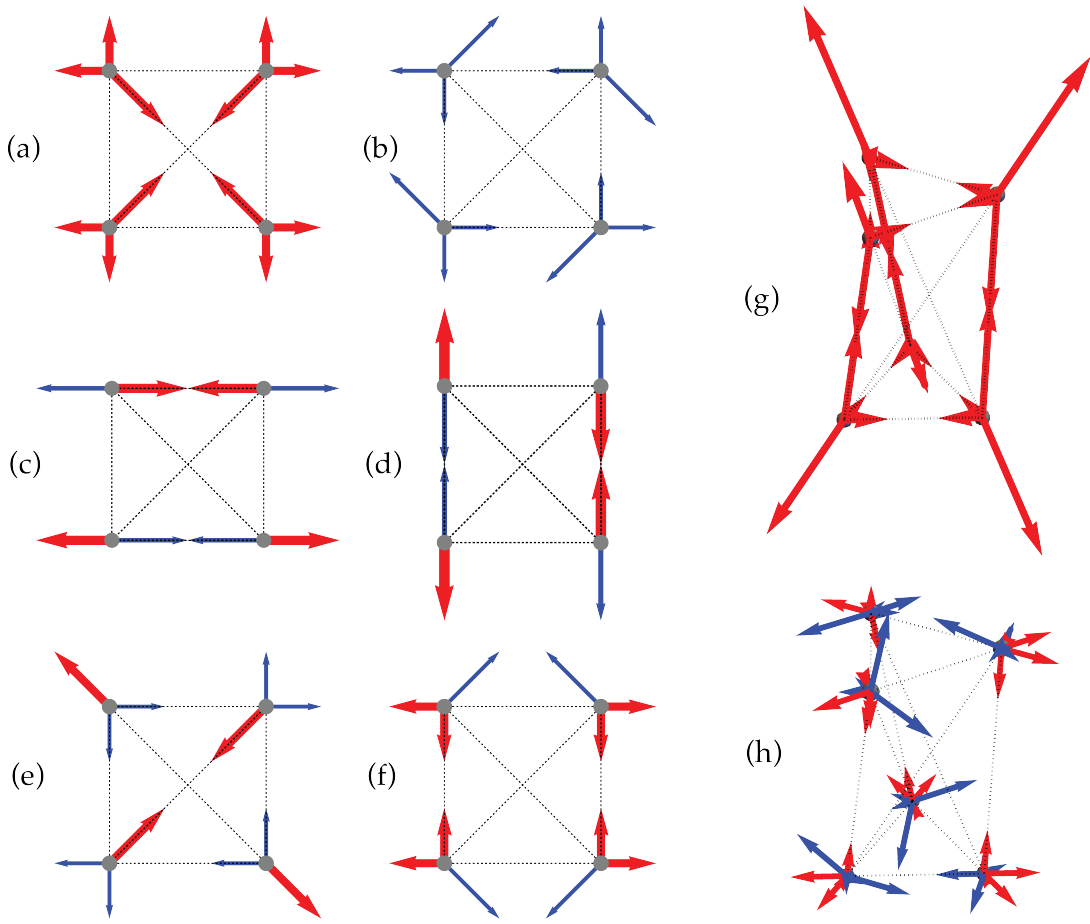


Figure 5.3: Examples of SSSs in prestressed systems. Red and blue arrows denote t^{\parallel}, t^{\perp} respectively. (a) SSS of a stress-free mechanical network. The two mechanical frames are shown as (a) the four grey sites connected by dotted lines as bonds to form a 2D frame; (g) the six grey sites connected in 3D to form a tensegrity T3 prism. When only considering \parallel directions, there is one SSS for the 2D frame, which is the single SSS shown in (a). After taking \perp directions into account, there are six SSSs for the 2D frame in total, which are shown from (a)-(f). With a tensegrity T3 prism structure, (g) indicates the single SSS when only considering \parallel directions. There are 21 SSSs in total when considering \perp directions, including (g)(h) shown as examples.

5.3.3 Stress distribution as linear combinations of states of self-stress

One important property of SSSs is that they form a linear space that contains *all* possible ways a network can carry stress while keeping all particles in force balance. Thus, actual stress distributions when the network is under load must come from linear combinations of SSSs, and the linear space of SSSs characterizes the capability of a system to carry any external load.

Here we first illustrate this formulation using a simple shear. If the network deforms affinely (i.e., homogeneous shear strain), one can write the affine shear as bond extensions $e_{\text{affine}}^{\parallel}$. For a stress-free system with all spring constants being 1 the bond tension in response to this shear can be decomposed in the SSSs linear space as

$$|t^{\parallel}\rangle = \sum_{i=1}^{N_{\text{SSS}}} |t_{\text{SSS},i}^{\parallel}\rangle \langle t_{\text{SSS},i}^{\parallel} | e_{\text{affine}}^{\parallel} \rangle, \quad (5.37)$$

where the sum runs in the N_{SSS} dimensional linear space of all SSSs, and $|t_{\text{SSS},i}^{\parallel}\rangle$ form an orthonormal basis of this linear space. This relation is straightforward to prove as follows: when bond extension $e_{\text{affine}}^{\parallel}$ is externally imposed (e.g., via Lee-Edwards boundary conditions), the system respond by displacements u (e.g., nonaffine deformations, or displacing internal particles) to minimize the elastic energy, so the resulting bond extensions are

$$|e^{\parallel}\rangle = |e_{\text{affine}}^{\parallel}\rangle + \mathbb{C}^{\parallel} |u\rangle. \quad (5.38)$$

If all spring constants are 1, we have $|t^{\parallel}\rangle = |e^{\parallel}\rangle$, and the linear combination coefficients of t^{\parallel} to the SSSs are

$$c_i = \langle t_{\text{SSS},i}^{\parallel} | t^{\parallel} \rangle = \langle t_{\text{SSS},i}^{\parallel} | e_{\text{affine}}^{\parallel} \rangle + \langle t_{\text{SSS},i}^{\parallel} | \mathbb{C}^{\parallel} |u\rangle. \quad (5.39)$$

The second term has to vanish because $\langle t_{\text{SSS},i}^{\parallel} | \mathbb{C}^{\parallel} = (\mathbb{Q}^{\parallel} |t_{\text{SSS},i}^{\parallel}\rangle)^T = 0$. This proves to the decomposition in Eq. (5.37).

Three comments can be made from this result. First, if this shear strain has no overlap with any SSSs in the system, $\langle t_{\text{SSS},i}^{\parallel} | t^{\parallel} \rangle = 0$ for all i , the system can not carry this load. What happens physically would be that the system yields under this load, until a new SSS emerges that can carry this load. Second, this formulation can also be applied to other types of load, such as hydrostatic pressure. It is important to note here that any component in e_{affine} that can be written in terms of $\mathbb{C}^{\parallel} | u \rangle$ will not cause stress—it correspond to strain that will be relaxed by degrees of freedom available to the system. Third, similar formulation can also be developed with loads applied via anchored boundaries, where SSSs are defined as bond tensions leaving internal sites in force balance, and the strain e can be applied from boundary connecting to boundaries.

The relation is slightly more complicated when the spring constants are not all the same,

$$|t^{\parallel}\rangle = \sum_{i,j}^{N_{\text{SSS}}} |t_{\text{SSS},i}^{\parallel}\rangle [(\mathbb{K}^{\parallel})_{ss}^{-1}]^{-1} \langle t_{\text{SSS},j}^{\parallel} | e_{\text{affine}}^{\parallel} \rangle, \quad (5.40)$$

where $(\mathbb{K}^{-1})_{ss}$ is the inverse of the spring constant matrix projected to the SSS linear space.

This relation can readily be generalized to the pre-stressed case, where

$$|t\rangle = \sum_{i,j}^{N_{\text{SSS}}} |t_{\text{SSS},i}\rangle [(\mathbb{K}^{-1})_{ss}]^{-1} \langle t_{\text{SSS},j} | e_{\text{affine}} \rangle. \quad (5.41)$$

A detailed proof of this relation is included in App. 5.8.1. It is worth noting that the response $|t\rangle$ calculated here is the addition to the prestress in response to the load, so the total stress in the system is $|t_p\rangle + |t\rangle$ where t_p only has longitudinal components and t has both longitudinal and transverse components.

5.3.4 Dipole response

Similar projections can also be applied to compute the stress response of a prestressed system to local forces, such as a force dipole.

In particular, when a force dipole acts on a network, all particles are in force balance from tensions within the network, and the two particles the force dipole acts on are not: they are only in force balance when the external dipole forces are included.

When this force dipole acts on a pair of particles that are connected by a bond in the network, the stress distribution that is excited is a SSS of the original network. This concept has been defined as “quasi-localized SSS” [69, 172] for the stress-free case. This can be understood as follows: although the force dipole is external, it could be viewed as carried by the bond in the original network (e.g. by changing its rest length). Thus, the stress distribution is a SSS of the original network. Here we extend this formulation to the prestressed case, where we define a “dipole stiffness” as

$$\kappa \equiv \frac{-2\langle f_{\text{dipole}} | u_{\text{rsp}} \rangle}{|\langle \hat{f}_{\text{dipole}} | u_{\text{rsp}} \rangle|^2} = \frac{-2\langle f_{\text{dipole}} | f_{\text{dipole}} \rangle}{\langle f_{\text{dipole}} | u_{\text{rsp}} \rangle}, \quad (5.42)$$

where $|f_{\text{dipole}}\rangle$ is the force dipole under particle representation, $|\hat{f}_{\text{dipole}}\rangle$ as its normalized vector, and $|u_{\text{rsp}}\rangle$ is the particle displacement response to the force dipole. This definition of dipole stiffness treats the whole system as a black box, and only extract the stiffness from the force-distance relation between the two particles.

Using the SSSs linear space, the dipole stiffness to a local force dipole on bond b is thus given as (details in the App. 5.8.2):

$$\kappa_b = \frac{4k_b^2}{k_b - \sum_{i,j} \langle b | t_{\text{SSS},i} \rangle [(\mathbb{K}^{-1})_{ss}]^{-1} \langle t_{\text{SSS},j} | b \rangle}, \quad (5.43)$$

where k_b is the spring stiffness for bond b and $|b\rangle$ represents a vector in the labeling space of bonds which has zeros in all components except for that the b -th component is set to unity.

In the case when the force dipole acts on a pair of particles that are not connected in the network, the stress distribution is not a SSS of the original network. Instead, it can be

viewed as a SSS of the original network with an “auxiliary bond” which carries exactly the dipole force. In App. 5.8.2 we also derive the stiffness of this case.

5.4 Prestressed triangular lattices

In this section we use prestressed triangular lattices to illustrate the prestressed elasticity we discussed in Secs. 5.2 and 5.3.

In the stress-free case, triangular lattices have a coordination number $z = 6 > 2d$ and thus the number of SSSs per site is $\frac{z}{2} - 2 = 1$. In fact, a localized SSS $|t_\ell\rangle$ can be defined around each site ℓ as shown in Fig. 5.4a. These site-localized SSSs provide a complete basis to decompose any SSSs on the triangular lattice.

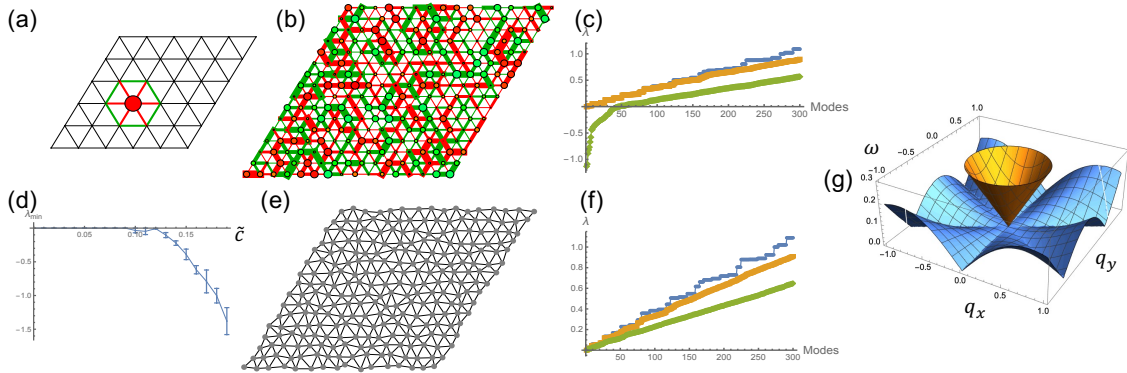


Figure 5.4: Vibrational modes of prestressed triangular lattices. (a) a site-localized SSS $|t_\ell\rangle$ on a triangular lattice, where bonds surrounding the hexagon carry tension, and bonds in the hexagon carry compression. The red disk on the center site represent the strength of this SSS. (b) A prestressed triangular lattice with the prestress generated using a linear combination of site-localized SSSs with independent coefficients on each site. (c) A triangular lattice with positional disorder. (d-f) Dynamical matrix eigenvalue analysis of 32×32 triangular lattices under periodic boundary condition with prestress (d-e) or positional disorder (f). (d) Lowest 300 eigenvalues λ of the dynamical matrix of prestressed triangular lattices in ascending order, at $\tilde{c} = 0$ (blue), $\tilde{c} = 0.1$ (orange), $\tilde{c} = 0.2$ (green), from top to bottom. (e) The lowest eigenvalue λ_{min} as a function of \tilde{c} . (f) Lowest 300 eigenvalues λ of the dynamical matrix of triangular lattices with positional disorder, at $\tilde{u} = 0$ (blue), $\tilde{u} = 0.1$ (orange), $\tilde{u} = 0.2$ (green), from top to bottom. (g) Phonon dispersion relation of the lowest band of triangular lattices with no prestress (yellow, upper), and critical compressive prestress (blue, lower) where modes along ΓM approach instability.

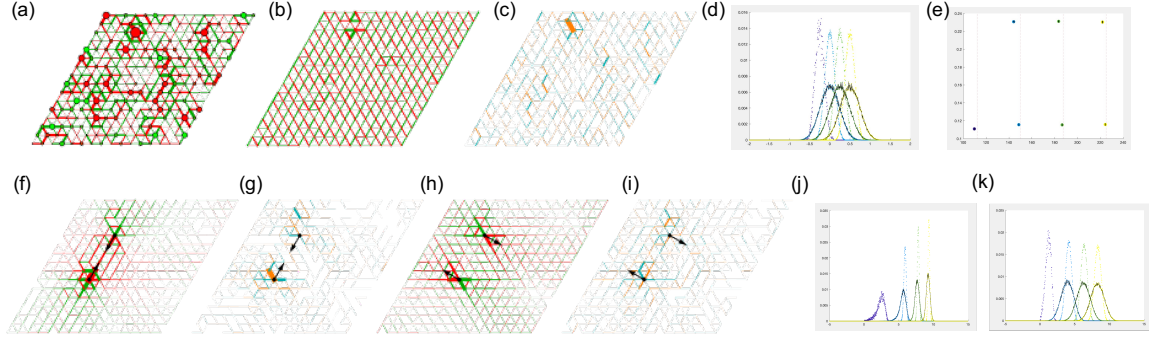


Figure 5.5: Prestressed triangular lattice under load. A triangular lattice with disordered prestress ($\bar{c} = 0, \tilde{c} = 0.12$ and all modes stable) in (a) responds to simple shear σ_{xy} , with longitudinal $|t^{\parallel}\rangle$ and transverse $|t^{\perp}\rangle$ forces shown in (b,c). Red and green denote compression and tension in (b). Orange and cyan denote clockwise and counter clockwise in (c). Note the stress shown in (b,c) is in addition to the prestress in (a). At different \bar{c} and \tilde{c} (d), the lattice exhibit shear modulus shown in (e). (f-i) longitudinal and transverse responses to longitudinal (f,g) and transverse (h,i) force dipoles (black arrows show directions of forces). (j,k) Stiffness against longitudinal and transverse dipoles.

In particular, we can generate an ensemble of prestress on triangular lattices by taking an arbitrary coefficient c_{ℓ} for each site-localized SSS $|t_{\ell}\rangle$ and sum them up. In Fig 5.4b we show an example of such a prestressed state.

These prestressed lattices can be physically constructed by choosing the rest length of each bond b such that when they are at the length in the regular triangular lattice, the tension/compression they carry is exactly the value $t_{b,p}$ in the prescribed SSSs. Because the total force is balanced at each site for any SSS, all bonds will stay at the length in the regular lattice, and thus we obtain a triangular lattice with *regular geometry and a prescribed SSS*.

What are the mechanical properties of such prestressed triangular lattices? Here we study them from two perspectives: vibrational modes and load-bearing capabilities. The vibrational modes can be calculated based on the quadratic expansion in Eq. (5.4) for each bond, which leads to the dynamical matrix defined in Eq. (5.29).

In Fig. 5.4d we show eigenvalues of the dynamical matrix of the triangular lattice at three levels of prestress (by assigning c_{ℓ} from a Gaussian distribution with mean at \bar{c} and standard deviation at \tilde{c}). Prestress significantly affects the vibrational modes especially at

low frequencies. In particular, negative eigenvalues start to appear when the fluctuations of the SSS goes beyond a critical level, $\tilde{c} > \tilde{c}^*$, in the case of $\bar{c} = 0$ (Fig. 5.4e). This indicates that by increasing the fluctuation of prestress (where the mean remains 0), unstable modes appear, although the system remains in force balance. This is in alignment with our discussion on prestressed rigidity in Sec. 5.2.3

To contrast this result, we also consider triangular lattices with positional disorder but no prestress (Fig. 5.4c). In this case, we move site ℓ by a random displacement \vec{u}_ℓ , the x, y components of which being generated from a Gaussian distribution with mean at $\bar{u} = 0$ and standard deviation at \tilde{u} . We also plot the eigenvalues of the dynamical matrix in Fig. 5.4f. Although positional disorder also affects the eigenvalues, it mostly smooths out the regular lattice eigenmodes, and does not lead to qualitative change at low frequencies. Note that to make a fair comparison we chose the same values for \tilde{c} and \tilde{u} , which represents the same level of disorder, under the simple convention we took where the bond length and spring constant on the triangular lattice both being unity.

The load-bearing capabilities of prestressed triangular lattices can be analyzed by the SSSs formalism discussed in Sec. 5.3. In particular, at any given realization of disordered prestress, we can compute the linear space of SSSs, and use Eq. (5.40) to find the stress response of the system to external load.

We apply this method to prestressed triangular lattices with two types of load: simple shear and dipole forces, and the results are shown in Fig. 5.5.

Furthermore, we also measured shear modulus of these prestressed triangular lattices at different values of mean and standard deviation, and the results are shown in Fig. 5.5 too. In general, positive mean stress (tension) leads to increased shear modulus, and negative mean stress (compression) leads to decreased shear modulus.

This can also be seen from the perspective of phonon structures of regular lattices. In Fig. 5.4 we show the lowest phonon bands of triangular and honeycomb lattice at different levels of (force-balanced) prestress. It is straightforward to see that negative prestress (com-

pression) destabilizes the originally stable triangular lattice, and positive prestress (tension) stabilizes the honeycomb lattice, which was originally unstable against shear. Interestingly, the modes that first become unstable in the triangular lattice as negative prestress increase are the modes along the ΓM direction in the first Brillouin zone, indicating that the type of modes that first become unstable are the modes that zig-zag between the straight lines of bonds, agreeing with recent studies of strain-localization in triangular lattices.

5.5 $3D$ numerical simulations of soft repulsive particle assemblies

The new \mathbb{Q}, \mathbb{C} matrix methods described in Sec. 5.3 provide a set of tools to analyze stress-bearing capabilities and mode structures of pre-stressed systems. In this section, we introduce a computational model for an assembly of soft repulsive particles, widely used for soft amorphous solids and glasses, on which this method can be applied. The amorphous solid is formed with pre-stress both from compression and frozen-in structural disorder. In Sec. 5.6 we will present results from applying this new method to this model system.

The numerical model describes a suspension of particles with soft repulsive interactions given by a truncated and shifted Lennard-Jones potential [173], whose strength ϵ is the unit energy in the simulations. The potential energy, for particle i and j , is $U(r_{ij}) = 4\epsilon[(a_{ij}/r_{ij})^{12} - (a_{ij}/r_{ij})^6] + \epsilon$ for $r_{ij} \leq 2^{1/6}a_{ij}$, otherwise $U(r_{ij}) = 0$. Here $a_{ij} = 1/2(a_i + a_j)$ with a_i and a_j being the diameters, and r_{ij} is the center-to-center distance between the two particles. The size poly-dispersity is introduced by drawing the diameter of each particle a_i from a Gaussian distribution with mean of unit length a and variance of 10%. All simulations used here have volume fraction $\phi \approx 70\%$ and consist of $10^4(10976)$ particles in a cubic box of linear size $L = 20.36$, unless otherwise specified. The initial samples are prepared by melting down FCC crystals of particle volume fraction 0.7 at $T = 5.0\epsilon/k_B$, and then they are cooled down to a low temperature $0.001\epsilon/k_B$ through

a NVT molecular dynamics (MD) protocol. The cooling rate Γ varies from 5×10^{-2} to $5 \times 10^{-6} \epsilon / (k_B \tau_0)$, where $\tau_0 = a \sqrt{m / \epsilon}$ is the MD time unit with m the particle mass. Subsequently each sample is quenched to a local energy minimum using a conjugate gradient (CG) algorithm. The resulting amorphous solid is under both a homogeneous compressional stress and disordered local stresses. In Fig. 5.6 we show a typical configuration where (negative) bond tensions are visualized.

We also examine these samples as they are strained using Lees-Edwards boundary conditions (LEBCs) and a shear rate $\dot{\gamma}$, by solving the related equations of motions with a drag force that guarantees minimal inertia effects as discussed in [174]. All simulations are performed using LAMMPS [106], with suitable modifications to include the particle size poly-dispersity and the interactions discussed above. More details of the preparation and shear protocols can be found in [174, 175].

To obtain the contact network for one configuration and define the \mathbb{Q} , \mathbb{C} matrices, we assigned bonds between pairs of particles with center-to-center distance no more than $2^{1/6} a_{ij}$, which is the cutoff range of the repulsive interaction in our model. With the contact network and particle coordinates, we built the compatibility and equilibrium matrices and studied the stressed elasticity using the general formalism proposed in previous sections. When building up the compatibility and equilibrium matrices \mathbb{Q} and \mathbb{C} , transverse directions of every bond need to be indicated and two orthogonal transverse directions besides the longitudinal one (the bond direction) are needed for each bond in a 3D system. In our formulation of the contact network, we defined the first transverse direction as the unit vector of the cross product between the bond vector and z -axis $(0, 0, 1)$, and the second transverse direction as the unit vector of the cross product between the bond vector and the first transverse direction. One needs to note that this selection of transverse directions is arbitrary as long as the two transverse directions and the bond direction vector are orthonormal to each other in the 3-D real space.

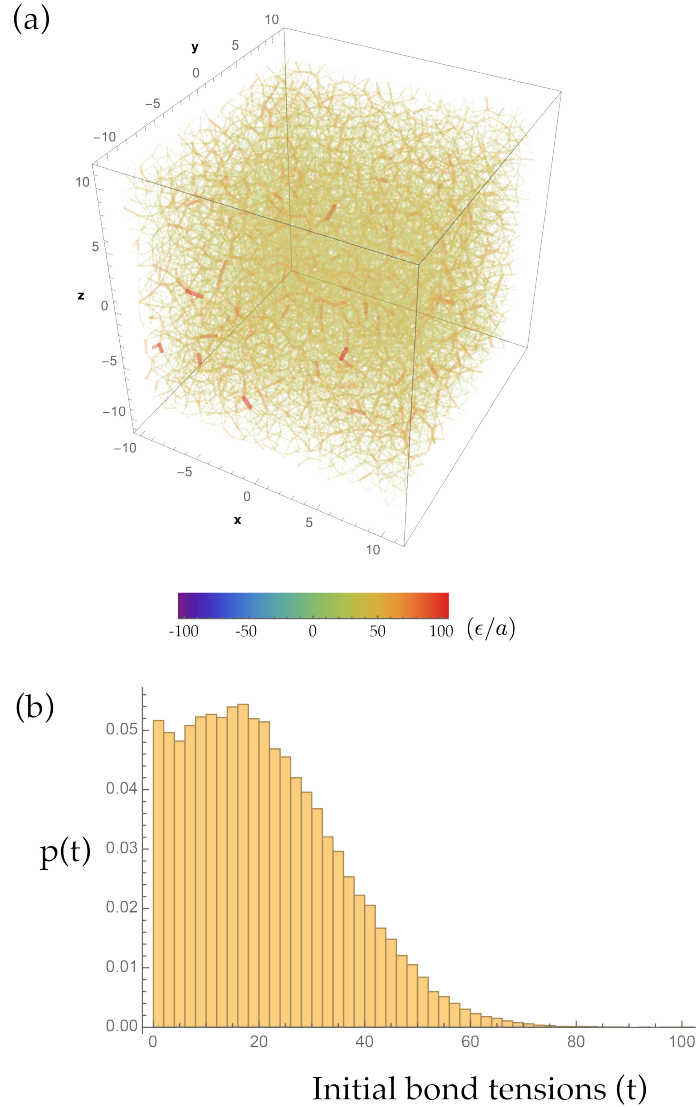


Figure 5.6: (a) Prestress visualization of colloidal glass systems. The system size is $N = 10976$ with preparation cooling rate $\Gamma = 5 \times 10^{-6} \epsilon / (k_B \tau_0)$. (b) Initial bond tension distribution for the configuration shown in (a).

When solving for SSSs in large stressed systems like the samples we generated, the null space for the equilibrium matrix \mathbb{Q} has very high dimensions. We used the SPQR_RANK package [53] from SuiteSparse [55], which is a high performance sparse QR decomposition package and can provide a reliable determination of null space basis vectors for large sparse matrices, to solve for SSSs efficiently and reliably, especially when there are lots of degeneracies for diagonalizing \mathbb{Q} . Similarly, SPQR_RANK is also suitable when solving

for the null space of \mathbb{Q}^T to get ZMs in large systems.

5.6 Results

5.6.1 Spatial heterogeneity of stress fields

Structural disorder in glasses manifest as spatial heterogeneities in the stress fields when they are subject to external load. In particular, the heterogeneity is mostly visible in plots of stress change, instead of the total stress, which appears to be rather homogeneous in dense systems.

Remarkably, this heterogeneity is accurately depicted from the SSS calculation when prestress is included. In contrast, when the system is approximated as a stress-free mechanical network, the stress response appears to be homogeneous.

Fig. 5.7 gives a visualization of the tension increment responses in simulated colloidal glass systems. Heterogeneity of tension responses is observed in such systems. Similar tension response clustering is predicted using stressed elasticity when considering pre-stress in such systems. However, when using the stress-free model to predict the elasticity, no such tension increment clustering is observed and the tension increment response is quite homogeneous under the shear strain.

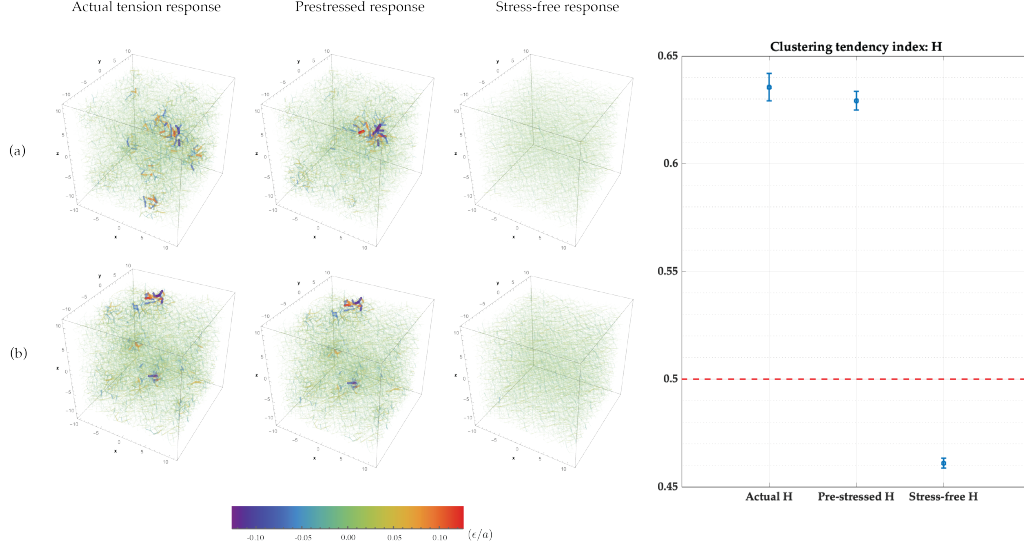


Figure 5.7: Actual tension increment compared to the tension increment prediction from pre-stressed elasticity and stress-free elasticity. (a) Cooling rate $\Gamma = 5 \times 10^{-2} \epsilon / (k_B T_0)$ with shear strain 1%, (b) cooling rate $\Gamma = 5 \times 10^{-6} \epsilon / (k_B T_0)$ with shear strain 0.01%. The system size is $N = 10976$ in both (a) and (b). (c) Clustering tendency index H averaged over two different samples with stress-free and pre-stressed elasticity compared to the actual H . The actual tension response is measured with shear strain 1% with system size $N = 10976$ and preparation cooling rate $\Gamma = 5 \times 10^{-6} \epsilon / (k_B T_0)$. The red dashed line indicates the threshold to determine whether or not the tension change is clustered.

We characterize this spatial heterogeneity using a clustering tendency index: the Hopkins statistic H [176], with a value close to 1 indicating the data is highly clustered, and a value around 0.5 from random data. Fig. 5.7(c) shows that the pre-stressed elasticity captures the tension increment clustering tendency which exists in actual tension responses, while in stress-free elasticity this clustering is overlooked.

5.6.2 Calculating stress response to shear using states of self-stress

We demonstrate the power of the SSSs as “stress-eigenstates” that characterize the stress-bearing capabilities of a system. To this end, we compute all SSSs of the system described in Sec. 5.5, and use Eq. (5.41) to calculate the change of stress as the system is under macroscopic shear, by taking e_{affine} to be an affine shear deformation field. At the same time, we also measure the change of the stress in the system in a numerical experiment

where the system is under a small quasistatic shear deformation. Figure. 5.8 shows the agreement between the tension change at each bond measured from quasistatic shear and the values calculated from SSSs.

To contrast this comparison, we also calculated the tension change treating the system as a stress-free network, i.e., as characterized by equilibrium matrix \mathbb{C}^{\parallel} instead of \mathbb{C} . As shown in Figure. 5.8, the calculated tension change is very different from actual tension change.

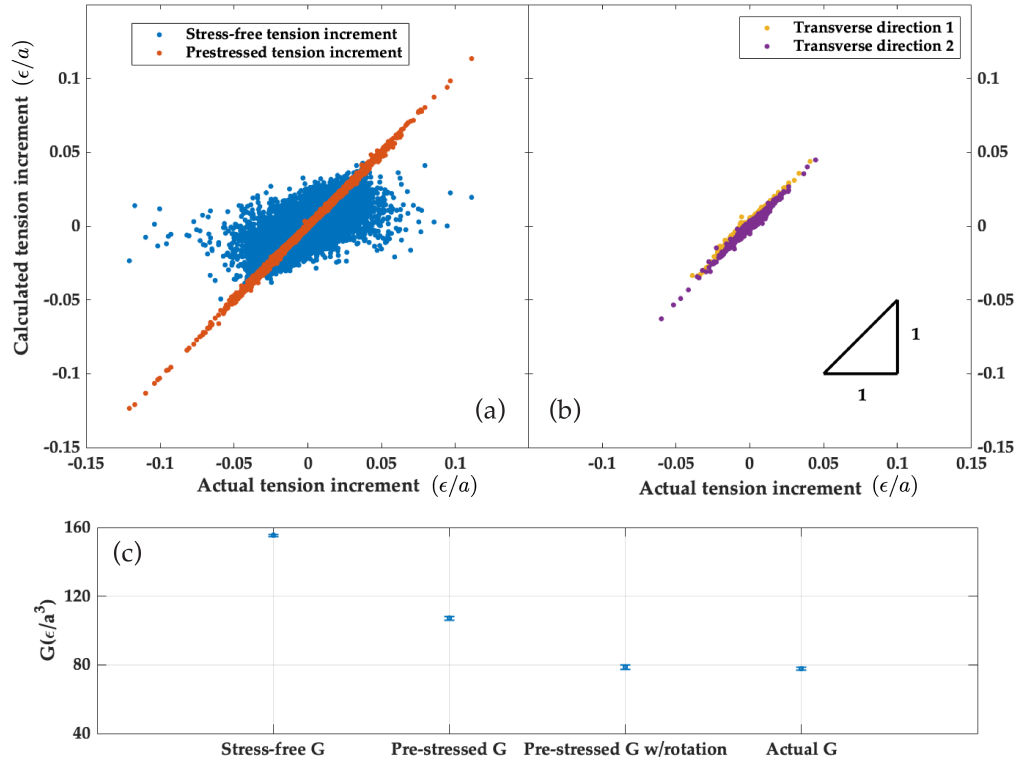


Figure 5.8: (a) Linear response of tension increment with and without considering pre-stress in the system. The pre-stressed tension increment are the tension increment along longitudinal directions; (b) Comparison to actual tension increment including transverse directions. Note: Here the actual tension increment response is from 0.01% strain compared to the initial configuration, and the system size is $N = 10976$, $\Gamma = 5 \times 10^{-6} \epsilon/(k_B\tau_0)$. (c) Shear modulus G from stress-free response and pre-stressed response compared to actual G . Note: Here the actual G is measured from 1% shear strain to the initial configuration, and the system size is $N = 10976$ with preparation cooling rate $\Gamma = 5 \times 10^{-6} \epsilon/(k_B\tau_0)$. G is averaged over three different samples for each data point.

The shear modulus G can be obtained from the stress distributions calculated from

either \mathbb{C}^{\parallel} or \mathbb{C} , and the results are shown in Fig. 5.8(c). Similar to the tension change measurements, the shear modulus calculated from \mathbb{C} is much closer to the actual shear modulus from energy minimization. This effect can also be viewed from the continuum elasticity formulation in Sec. 5.2.2: when the macroscopic shear deformation field $\partial_y u_x$ is plugged into the continuum theory, the elastic energy density is

$$E/V = \frac{1}{2}(K_{xyxy} + \sigma_{p,yy})(\partial_y u_x)^2, \quad (5.44)$$

leading to a prestress-corrected shear modulus of $G = K_{xyxy} + \sigma_{p,yy}$. It is straightforward from this relations that an isotropic compressional prestress ($\sigma_{ij} = -p\delta_{ij}$) destabilizes the shear rigidity of a network.

Besides the prestress effects on tension responses, the effect of bond rotations is characterized by calculating the shear modulus G with tension increment responses from prestressed elasticity, using the after-sheared bond orientations. From Fig. 5.8 one can see that prestressed elasticity captures the tension response behaviors, while bond rotations take another important part of role to contribute to G .

This demonstrates that the inclusion of prestress effects are essential in characterizing the mechanical response of glasses which are always prestressed.

5.6.3 General statistics of states of self-stress

Next, we collect statistical information on SSSs of glasses at different preparation protocols.

The total number of SSSs in a pre-stressed system, which equals the dimension of the null space of the \mathbb{Q} matrix, is directly related to the numbers of degrees of freedom and constraints via the Maxwell-Calladine index theorem,

$$N_0 - N_{SSS} = Nd - N_b d, \quad (5.45)$$

where N_0 is the number of ZMs. This can be proven using the rank-nullity theorem on the \mathbb{Q}, \mathbb{C} matrices, similar to the proof for stress-free systems. Here the main difference from stress-free systems is that the number of constraints is $N_b d$ instead of N_b , as each bond provides d constraints via one from e^{\parallel} and $d - 1$ from e^{\perp} .

In Fig. 5.9 we show the total numbers of SSSs in the repulsive glass systems we study at different preparation protocol. Fig. 5.9(a) verifies the Maxwell-Calladine index theorem for pre-stressed system in Equation. (5.45). The number N_{SSS} decreases with the increase of cooling rate, and the number of bonds and shear modulus decrease as well.

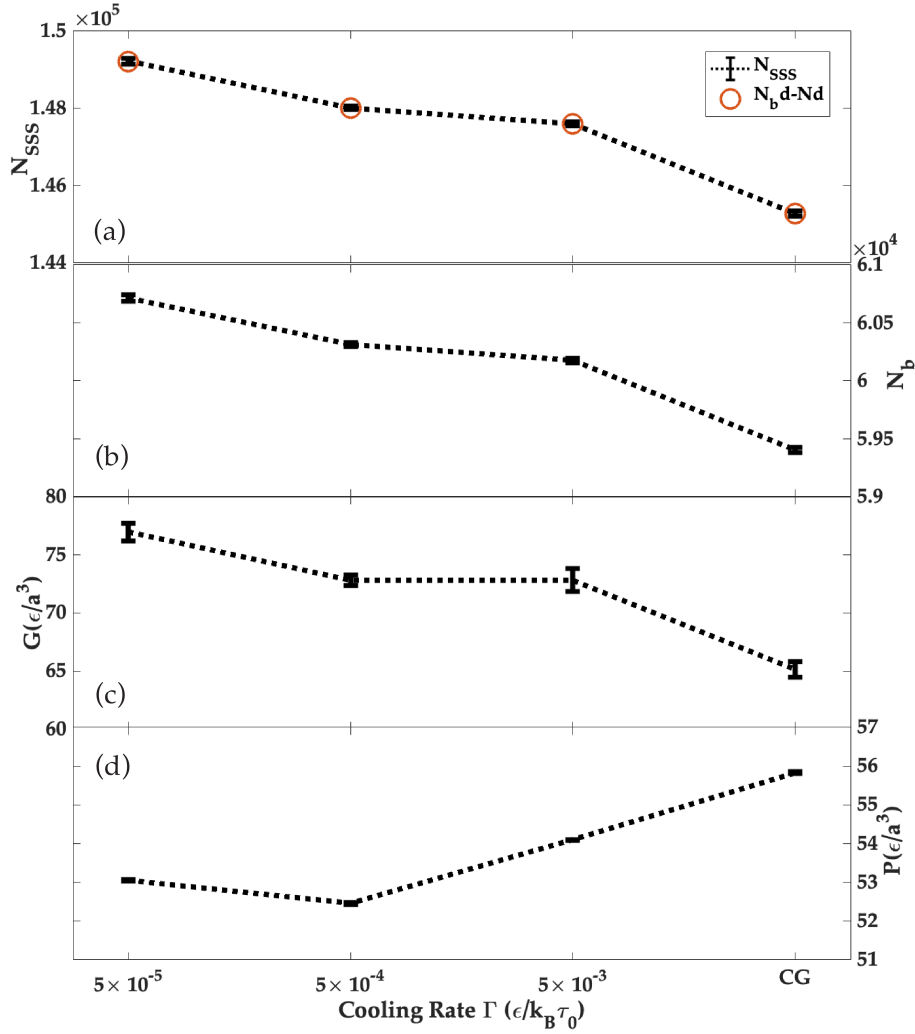


Figure 5.9: (a) Number of SSSs (N_{SSS}), (b) number of bonds (N_b), (c) measured shear modulus (G), (d) averaged normal stress (P) for different cooling rates Γ . Those quantities are averaged over 5 different configurations for each cooling rate, and the system size is $N = 10976$.)

5.6.4 Local dipole stiffness in prestressed glasses

We look at local dipole force responses in prestressed systems, with introducing transverse bond directions when defining the dipole stiffness κ . Bond locally minimized κ is calculated, representing the least stiffness of dipole force responses between the two particles, among all possible parallel and transverse directions (details in App. 5.8.2).

Fig. 5.10(a) gives an example of applying a transverse force dipole on a local bond

in prestressed systems, showing both \parallel and \perp tension responses. Such transverse force dipoles, which are studied at the first time, indicate the effect of prestress to determine the responses of soft solids. The near field of the local force dipole has larger magnitude of responses in \parallel bond directions while in the far field, the prestress induces more bond rotations.

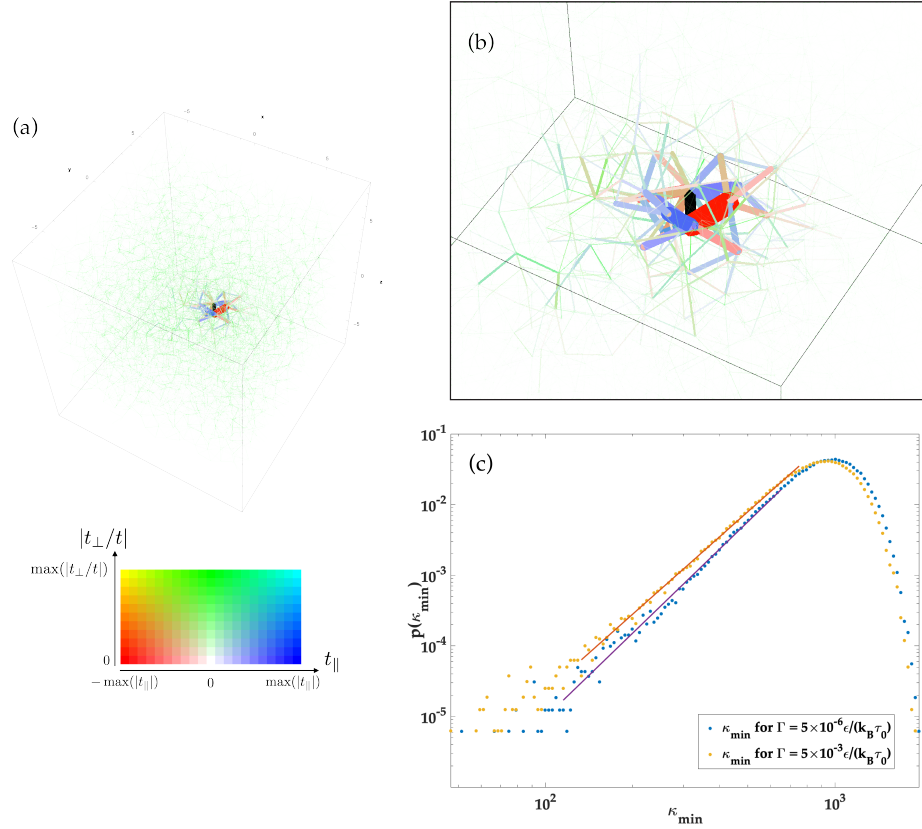


Figure 5.10: (a) Tension responses of a \perp force dipole applied on the highlighted bond with black color. The 2-D color scheme contains t_{\parallel} indicating tension/compression in bonds and $|t_{\perp}/t|$ indicating the rotational responses. (b) gives a zoomed-in view to the dipole force response in (a). The visualized sample configuration has system size $N = 2916$ with preparation cooling rate $\Gamma = 5 \times 10^{-6} \epsilon / (k_B \tau_0)$. (c) Distribution of minimum κ for systems with different preparation protocols. System size: $N = 2916$; The histogram is averaged over 10 different samples for each preparation cooling rate.

The minimized local dipole stiffness κ_{\min} is compared in two different preparation cooling rates as shown in Fig. 5.10(c), indicating the impact of preparation history to the mechanical stiffness in prestressed systems. From the statistics collected, $\bar{\kappa}_{\min}(\Gamma = 5 \times$

$10^{-6}) = 918.41 \pm 4.34 \epsilon/a^2$; $\bar{\kappa}_{min}(\Gamma = 5 \times 10^{-3}) = 861.45 \pm 3.35 \epsilon/a^2$. An exponent is extracted in small κ region as shown as fitted lines in Fig. 5.10(c). Noting the power exponent as β , we have $\beta(\Gamma = 5 \times 10^{-6}) = 3.96 \pm 0.07$; $\beta(\Gamma = 5 \times 10^{-6}) = 3.65 \pm 0.04$.

5.7 Discussion

The general method we introduce here incorporates the effect of prestress in elasticity of amorphous solids. Stress-bearing abilities of glasses, as characterized by SSSs, provide a new way to unravel mechanical response of glasses to any load, both macroscopic and local. The spatial heterogeneity of stress fields, which comes from prestress rather than geometry, indicates structural disorder in glasses. The statistics of these SSSs sheds new light on understanding yielding, shear thinning and thickening, as well as providing input to field theory for the dynamics of dense suspensions.

There are many more to work on along this route. The evolution of SSSs to external loads, especially when the geometry is almost intact but prestress evolves, indicates the impact of prestress on glassy dynamics and can provide a novel pathway to study glass behaviors beyond network geometry.

5.8 Appendices

5.8.1 SSSs formulation for shear response of prestressed networks

5.8.1.1 Projection of the shear load to the SSSs linear space

When a mechanical network is subject to a shear load, the resulting bond extensions and rotations can be written as the sum of contributions from the affine shear field e_{affine} and the nonaffine displacements $\mathbb{C}|u_{\text{rsp}}\rangle$,

$$|e\rangle = |e_{\text{affine}}\rangle + \mathbb{C}|u_{\text{rsp}}\rangle, \quad (5.46)$$

which is similar to Eq. (5.38) in the main text, but here we include both the parallel and the perpendicular components of e .

When force-balance is reached, net force on each particle vanishes,

$$|f\rangle = \mathbb{Q}|t\rangle = \mathbb{Q}\mathbb{K}(|e_{\text{affine}}\rangle + \mathbb{C}|u_{\text{rsp}}\rangle) = 0. \quad (5.47)$$

This means that $|t\rangle = \mathbb{K}(|e_{\text{affine}}\rangle + \mathbb{C} \cdot |u_{\text{rsp}}\rangle)$ must be a vector that belongs to the null space of \mathbb{Q} . Thus it can be written as a linear combinations of the SSSs of the system.

To facilitate the discussion of this SSSs linear combination, we define the following notations. Let $\{\vec{t}_s^{(1)}, \dots, \vec{t}_s^{(N_s)}\}$ be an orthonormal basis of the null space of \mathbb{Q} , and let P_s^Q denote the $N_b d \times N_s$ matrix whose columns are $\vec{t}_s^{(1)}, \dots, \vec{t}_s^{(N_s)}$, i.e., $P_s^Q = \begin{bmatrix} \vec{t}_s^{(1)} & \dots & \vec{t}_s^{(N_s)} \end{bmatrix}$. One can also define the $N_b d \times (N_b d - N_s)$ dimensional matrix P_r^Q whose columns are an orthonormal basis of the orthogonal compliment of the null space of \mathbb{Q} . Similarly one can define the $Nd \times N_0$ matrix P_s^C whose columns are an orthonormal basis of the null space of \mathbb{C} , and the $Nd \times (Nd - N_0)$ matrix P_r^C whose columns are an orthonormal basis of the orthogonal compliment of the null space of \mathbb{C} . These matrices are represented as,

$$P_s^Q = \begin{bmatrix} \vec{t}_s^{(1)} & \dots & \vec{t}_s^{(N_s)} \end{bmatrix}, \quad (5.48)$$

$$P_r^Q = \begin{bmatrix} \vec{t}_r^{(1)} & \dots & \vec{t}_r^{(N_b d - N_s)} \end{bmatrix}, \quad (5.49)$$

$$P_s^C = \begin{bmatrix} \vec{u}_s^{(1)} & \dots & \vec{u}_s^{(N_0)} \end{bmatrix}, \quad (5.50)$$

$$P_r^C = \begin{bmatrix} \vec{u}_r^{(1)} & \dots & \vec{u}_r^{(Nd - N_0)} \end{bmatrix}, \quad (5.51)$$

and they satisfy the following identities,

$$(P_s^Q)^T \cdot P_s^Q = \mathbb{I}_{(N_s)}, \quad (5.52)$$

$$(P_r^Q)^T \cdot P_r^Q = \mathbb{I}_{(N_b d - N_s)}, \quad (5.53)$$

$$(P_s^C)^T \cdot P_s^C = \mathbb{I}_{(N_0)}, \quad (5.54)$$

$$(P_r^C)^T \cdot P_r^C = \mathbb{I}_{(N d - N_0)}, \quad (5.55)$$

$$P_s^Q \cdot (P_s^Q)^T + P_r^Q \cdot (P_r^Q)^T = \mathbb{I}_{(N_b d)}, \quad (5.56)$$

$$P_s^C \cdot (P_s^C)^T + P_r^C \cdot (P_r^C)^T = \mathbb{I}_{(N d)} \quad (5.57)$$

As we discussed above, $|t\rangle$ is a linear combination of the SSSs,

$$|t\rangle = \sum_i^{N_s} \alpha_i |t_{\text{SSS},i}\rangle = P_s^Q \cdot \vec{\alpha},$$

where $\vec{\alpha}$ are coefficients of the linear combination of $|t\rangle$ as the SSSs.

Because the basis we use are orthonormal,

$$\vec{\alpha} = (P_s^Q)^T |t\rangle = (P_s^Q)^T \mathbb{K}(|e_{\text{affine}}\rangle + \mathbb{C}|u_{\text{rsp}}\rangle), \quad (5.58)$$

$$\vec{0} = (P_r^Q)^T |t\rangle = (P_r^Q)^T \mathbb{K}(|e_{\text{affine}}\rangle + \mathbb{C}|u_{\text{rsp}}\rangle). \quad (5.59)$$

Inserting identity matrix [Eq. (5.56)] into Eq. (5.59) and using the fact that,

$$\mathbb{Q} \cdot P_s^Q = \vec{0},$$

we have,

$$\begin{aligned}
\vec{0} &= (P_r^Q)^T \mathbb{K} \cdot [P_s^Q \cdot (P_s^Q)^T + P_r^Q \cdot (P_r^Q)^T] \cdot (|e_{\text{affine}}\rangle + \mathbb{C}|u_{\text{rsp}}\rangle) \\
&= (P_r^Q)^T \mathbb{K} \cdot [P_s^Q \cdot (P_s^Q)^T \cdot \mathbb{Q}^T + P_r^Q \cdot (P_r^Q)^T \cdot \mathbb{Q}^T] \cdot |u_{\text{rsp}}\rangle \\
&\quad + (P_r^Q)^T \mathbb{K} \cdot [P_s^Q \cdot (P_s^Q)^T + P_r^Q \cdot (P_r^Q)^T] \cdot |e_{\text{affine}}\rangle \\
&= (P_r^Q)^T \mathbb{K} \cdot P_r^Q \cdot (P_r^Q)^T \cdot \mathbb{Q}^T \cdot |u_{\text{rsp}}\rangle + (P_r^Q)^T \mathbb{K} \cdot [P_s^Q \cdot (P_s^Q)^T + P_r^Q \cdot (P_r^Q)^T] \cdot |e_{\text{affine}}\rangle \\
&= \mathbb{K}_{rr} (P_r^Q)^T \mathbb{Q}^T \cdot |u_{\text{rsp}}\rangle + [\mathbb{K}_{rs} (P_s^Q)^T + \mathbb{K}_{rr} (P_r^Q)^T] \cdot |e_{\text{affine}}\rangle \\
&\implies (P_r^Q)^T \mathbb{Q}^T \cdot |u_{\text{rsp}}\rangle = -(\mathbb{K}_{rr})^{-1} [\mathbb{K}_{rs} (P_s^Q)^T + \mathbb{K}_{rr} (P_r^Q)^T] \cdot |e_{\text{affine}}\rangle, \tag{5.60}
\end{aligned}$$

where we defined the decomposition of \mathbb{K} into the null and orthogonal compliment space as

$$\mathbb{K} \rightarrow \begin{pmatrix} (P_s^Q)^T \cdot \mathbb{K} \cdot P_s^Q & (P_s^Q)^T \cdot \mathbb{K} \cdot P_r^Q \\ (P_r^Q)^T \cdot \mathbb{K} \cdot P_s^Q & (P_r^Q)^T \cdot \mathbb{K} \cdot P_r^Q \end{pmatrix} = \begin{pmatrix} \mathbb{K}_{ss} & \mathbb{K}_{sr} \\ \mathbb{K}_{rs} & \mathbb{K}_{rr} \end{pmatrix} \tag{5.61}$$

and also used the fact that \mathbb{K}_{rr} is invertible.

The coefficients $\vec{\alpha}$ in Eq. (5.58) can then be solved as

$$\vec{\alpha} = (P_s^Q)^T \mathbb{K} \cdot [P_s^Q \cdot (P_s^Q)^T + P_r^Q \cdot (P_r^Q)^T] \cdot (\mathbb{Q}^T |u_{\text{rsp}}\rangle + |e_{\text{affine}}\rangle) \quad (5.62)$$

$$= (P_s^Q)^T \mathbb{K} \cdot P_r^Q \cdot (P_r^Q)^T \cdot \mathbb{Q}^T \cdot |u_{\text{rsp}}\rangle \quad (5.63)$$

$$+ (P_s^Q)^T \mathbb{K} \cdot [P_s^Q \cdot (P_s^Q)^T + P_r^Q \cdot (P_r^Q)^T] \cdot |e_{\text{affine}}\rangle \quad (5.64)$$

$$= \mathbb{K}_{sr} (P_r^Q)^T \mathbb{Q}^T \cdot |u_{\text{rsp}}\rangle + [\mathbb{K}_{ss} (P_s^Q)^T + \mathbb{K}_{sr} (P_r^Q)^T] \cdot |e_{\text{affine}}\rangle \quad (5.65)$$

$$\text{(from Equation (5.60))} = \mathbb{K}_{sr} \{ -(\mathbb{K}_{rr})^{-1} [\mathbb{K}_{rs} (P_s^Q)^T + \mathbb{K}_{rr} (P_r^Q)^T] \cdot |e_{\text{affine}}\rangle \} \quad (5.66)$$

$$+ [\mathbb{K}_{ss} (P_s^Q)^T + \mathbb{K}_{sr} (P_r^Q)^T] \cdot |e_{\text{affine}}\rangle \quad (5.67)$$

$$= \{ \mathbb{K}_{sr} (P_r^Q)^T + \mathbb{K}_{ss} (P_s^Q)^T - \mathbb{K}_{sr} (\mathbb{K}_{rr})^{-1} [\mathbb{K}_{rs} (P_s^Q)^T + \mathbb{K}_{rr} (P_r^Q)^T] \} \cdot |e_{\text{affine}}\rangle \quad (5.68)$$

$$= [\mathbb{K}_{ss} (P_s^Q)^T - \mathbb{K}_{sr} (\mathbb{K}_{rr})^{-1} \mathbb{K}_{rs} (P_s^Q)^T] \cdot |e_{\text{affine}}\rangle \quad (5.69)$$

$$= [\mathbb{K}_{ss} - \mathbb{K}_{sr} (\mathbb{K}_{rr})^{-1} \mathbb{K}_{rs}] \cdot (P_s^Q)^T \cdot |e_{\text{affine}}\rangle. \quad (5.70)$$

This can be further simplified by letting $\mathbb{A} = \mathbb{K}^{-1}$, and decompose \mathbb{A} into the column-space and null-space of \mathbb{Q} as,

$$\mathbb{A} \rightarrow \begin{pmatrix} (P_s^Q)^T \cdot \mathbb{A} \cdot P_s^Q & (P_s^Q)^T \cdot \mathbb{A} \cdot P_r^Q \\ (P_r^Q)^T \cdot \mathbb{A} \cdot P_s^Q & (P_r^Q)^T \cdot \mathbb{A} \cdot P_r^Q \end{pmatrix} = \begin{pmatrix} \mathbb{A}_{ss} & \mathbb{A}_{sr} \\ \mathbb{A}_{rs} & \mathbb{A}_{rr} \end{pmatrix} \quad (5.71)$$

One can see that

$$\mathbb{K}_{ss} \cdot \mathbb{A}_{ss} + \mathbb{K}_{sr} \cdot \mathbb{A}_{rs} = \mathbb{I}_{ss} \quad (5.72)$$

$$\mathbb{K}_{rs} \cdot \mathbb{A}_{ss} + \mathbb{K}_{rr} \cdot \mathbb{A}_{rs} = \vec{0}_{rs} \quad (5.73)$$

$$\implies \quad (5.74)$$

$$\mathbb{K}_{ss} + \mathbb{K}_{sr} \cdot \mathbb{A}_{rs} \cdot (\mathbb{A}_{ss})^{-1} = (\mathbb{A}_{ss})^{-1} \quad (5.75)$$

$$\mathbb{K}_{rs} = -\mathbb{K}_{rr} \cdot \mathbb{A}_{rs} \cdot (\mathbb{A}_{ss})^{-1} \quad (5.76)$$

$$\implies \quad (5.77)$$

$$\mathbb{K}_{ss} + \mathbb{K}_{sr} \cdot \mathbb{A}_{rs} \cdot \mathbb{A}_{ss}^{-1} = (\mathbb{A}_{ss})^{-1} \quad (5.78)$$

$$-(\mathbb{K}_{rr})^{-1} \cdot \mathbb{K}_{rs} = \mathbb{A}_{rs} \cdot (\mathbb{A}_{ss})^{-1} \quad (5.79)$$

$$\implies \quad (5.80)$$

$$\mathbb{K}_{ss} - \mathbb{K}_{sr} \cdot (\mathbb{K}_{rr})^{-1} \cdot \mathbb{K}_{rs} = (\mathbb{A}_{ss})^{-1} = ((\mathbb{K}^{-1})_{ss})^{-1} \quad (5.81)$$

As a result, $\vec{\alpha}$ is simplified to

$$\vec{\alpha} = ((\mathbb{K}^{-1})_{ss})^{-1} \cdot (P_s^Q)^T \cdot |e_{\text{affine}}\rangle \quad (5.82)$$

and the tension response to this external shear is

$$|t\rangle = P_s^Q \cdot ((\mathbb{K}^{-1})_{ss})^{-1} \cdot (P_s^Q)^T \cdot |e_{\text{affine}}\rangle. \quad (5.83)$$

Note that this t includes both t^{\parallel} and t^{\perp} , and this formulation applies to other types of homogeneous strain, such as hydrostatic compression, as well.

5.8.1.2 Affine bond deformation in prestressed systems

In this subsection we derive the e_{affine} field for any external load represented by a strain tensor ϵ .

The affine bond deformation for bond β from uniform strain ϵ_{ij} is given as,

$$e_{\beta}^{\text{aff}} = \hat{b}_{\beta,i} \epsilon_{ij} b_{\beta,j}$$

where \vec{b}_{β} is the end-to-end vector for bond β . This equation applies to the case when only considering parallel bond directions.

To have the bond deformation $|e_{\text{affine}}\rangle$ in Equation 5.40, one needs to incorporate transverse direction bond stretch. To start, one can write down the affine stretch of bond β as

$$e_{\beta}^{\text{aff}} = \hat{\mathbf{b}}_{\beta} \cdot (\mathbf{u}(s'_{\beta}) - \mathbf{u}(s_{\beta}))$$

In the linearized limit, the displacement vector \mathbf{u} for some point s is given as

$$\mathbf{u}(s) = \mathbf{\Gamma} \cdot \mathbf{X}(s)$$

Then the affine stretch of parallel direction is

$$\begin{aligned} e_{\beta,||}^{\text{aff}} &= \hat{\mathbf{b}}_{\beta} \cdot \mathbf{\Gamma} \cdot (\mathbf{X}(s'_{\beta}) - \mathbf{X}(s_{\beta})) \\ &= \hat{\mathbf{b}}_{\beta} \cdot \mathbf{\Gamma} \cdot \mathbf{b}_{\beta} \\ &= \hat{b}_{\beta,i} \cdot \epsilon_{ij} \cdot b_{\beta,j} \end{aligned} \tag{5.84}$$

where ϵ_{ij} is the strain tensor.

The affine stretch of transverse components is thus similarly when considering trans-

verse directions as:

$$\begin{aligned}
e_{\beta,\perp}^{\text{aff}} &= \hat{\mathbf{b}}_{\beta,\perp} \cdot (\mathbf{u}(s'_\beta) - \mathbf{u}(s_\beta)) \\
&= \hat{\mathbf{b}}_{\beta,\perp} \cdot \boldsymbol{\Gamma} \cdot (\mathbf{X}(s'_\beta) - \mathbf{X}(s_\beta)) \\
&= \frac{1}{2} \left(\hat{\mathbf{b}}_{\beta,\perp} \cdot \boldsymbol{\Gamma} \cdot \mathbf{b}_\beta + \mathbf{b}_\beta^T \cdot \boldsymbol{\Gamma}^T \cdot (\hat{\mathbf{b}}_{\beta,\perp})^T \right)
\end{aligned}$$

In the end, one can obtain $|e_{\text{affine}}\rangle$ as

$$|e_{\text{affine}}\rangle = \begin{pmatrix} |e_{\parallel}^{\text{aff}}\rangle \\ |e_{\perp}^{\text{aff}}\rangle \end{pmatrix}$$

5.8.2 Dipole stiffness κ in prestressed systems

When a pair of dipole forces is applied on a mechanical network between two particles that belong to the same rigid cluster, the network will show a linear response with tension distributed on the bonds. In this Appendix we derive the stress field of a prestressed network in response to the force dipole, and obtain a computationally efficient formula that gives the stiffness the system has against this force dipole.

5.8.2.1 Local dipole stiffness

We first consider the case of a force dipole acting on a pair of particles in contact (i.e., connected by a bond in the network, which we call bond b). In this case, the dipole force can be written as

$$|f_{\text{dipole}}\rangle = \mathbb{Q}|t_{\text{dipole}}\rangle = \mathbb{Q}\mathbb{K}|b\rangle,$$

where $|b\rangle$ is the bond space vector where only bond b is set to unity and all other bonds at zero. When \mathbb{K} acts on it we obtain a tension vector $|t_{\text{dipole}}\rangle$ where only bond b carries tension $k_b \cdot 1$. Acting \mathbb{Q} on this vector then gives the force vector where only this pair of

particle experience the dipole force (of magnitude $k_b \cdot 1$ and pointing along bond b) and all other particles feel no force, which is exactly the external force dipole acting on the system.

In response to this force dipole, the system produces a linear response, which can be written as a displacement field $|u_{\text{rsp}}\rangle$, which leads to a tension response on the network

$$|t_{\text{rsp}}\rangle = \mathbb{K}\mathbb{C}|u_{\text{rsp}}\rangle.$$

This bond tension vector is *not* a SSS of the system, because it leads to net forces on the two particles where the dipole acts on, which balances the external dipole. In other words, the sum of this response and the external dipole is a SSS,

$$\mathbb{Q}(|t_{\text{dipole}}\rangle + |t_{\text{rsp}}\rangle) = 0.$$

This sum can always be expanded as a linear combination of all SSSs of the prestressed network,

$$|t_{\text{dipole}}\rangle + |t_{\text{rsp}}\rangle = \sum_i^{N_{\text{SSS}}} \alpha_i |t_{\text{SSS},i}\rangle.$$

The coefficients α_i are determined in the same way as discussed in App. 5.8.1, just by replacing $|e_{\text{aff}}\rangle$ with $|b\rangle$. As a result

$$|t_{\text{dipole}}\rangle + |t_{\text{rsp}}\rangle = P_s^Q \cdot ((\mathbb{K}^{-1})_{ss})^{-1} \cdot (P_s^Q)^T \cdot |b\rangle.$$

We can thus use this in the expression for the dipole stiffness, where the denominator is now

$$\begin{aligned} -\langle f_{\text{dipole}} | u_{\text{rsp}} \rangle &= -\langle b | \mathbb{K}\mathbb{C} | u_{\text{rsp}} \rangle \\ &= k_b - \sum_{i,j}^{N_{\text{SSS}}} \langle b | t_{\text{SSS},i} \rangle [(\mathbb{K}^{-1})_{ss}]^{-1} \langle t_{\text{SSS},j} | b \rangle. \end{aligned}$$

Therefore the dipole stiffness is

$$\begin{aligned}
\kappa_b &= \frac{2\langle f_{\text{dipole}} | f_{\text{dipole}} \rangle}{-\langle f_{\text{dipole}} | u_{\text{rsp}} \rangle} \\
&= \frac{2\langle b | \mathbb{K} \mathbb{C} \mathbb{Q} \mathbb{K} | b \rangle}{\langle b | \mathbb{K} | b \rangle - \langle b | \sum_{i,j}^{N_{\text{SSS}}} | t_{\text{SSS},i} \rangle [(\mathbb{K}^{-1})_{ss}]^{-1} \langle t_{\text{SSS},j} | b \rangle} \\
&= \frac{4k_b^2}{k_b - \sum_{i,j}^{N_{\text{SSS}}} \langle b | t_{\text{SSS},i} \rangle [(\mathbb{K}^{-1})_{ss}]^{-1} \langle t_{\text{SSS},j} | b \rangle}
\end{aligned} \tag{5.85}$$

5.8.2.2 Non-local dipole stiffness

Besides applying the force dipole on an arbitrary existing bond b in the system, one could also apply a force dipole between two particles which are not originally connected.

The general formulation with imposed force dipole $|f_{\text{dipole}}\rangle$ can be written as:

$$0 = |f_{\text{final}}\rangle = |f_{\text{dipole}}\rangle + \mathbb{Q} \mathbb{K} \mathbb{C} |u\rangle,$$

where $|u\rangle$ indicates the particle displacements after force equilibrium. This can be interpreted as adding an auxiliary bond between the two sites that carry $|f_{\text{dipole}}\rangle$. In this sense, a new SSS is added to the system by the auxiliary bond.

Here we introduce the new mechanical matrices after introducing the auxiliary bond (which has zero stiffness so that it will not induce tension responses) as

$$\begin{aligned}
\tilde{\mathbb{C}} &= \begin{pmatrix} \mathbb{C} \\ C_a \end{pmatrix}, & \tilde{\mathbb{Q}} &= \begin{pmatrix} \mathbb{Q} & Q_a \end{pmatrix}, & \tilde{\mathbb{K}} &= \begin{pmatrix} \mathbb{K} \\ 0 \end{pmatrix}, \\
\tilde{\mathbb{C}} \cdot |u\rangle &= \begin{pmatrix} |e\rangle \\ e_a \end{pmatrix}, & \tilde{\mathbb{Q}} \cdot \begin{pmatrix} |t\rangle \\ t_a \end{pmatrix} &= |f\rangle.
\end{aligned}$$

The dimension of the matrices corresponding to bonds is extended with one additional

component from the auxiliary bond indexed as a .

Now the tension distribution can be written as

$$|\tilde{t}\rangle = \begin{pmatrix} |t\rangle \\ t_{\text{dipole}} \end{pmatrix} = \begin{pmatrix} \mathbb{K}\mathbb{C}|u\rangle \\ t_{\text{dipole}} \end{pmatrix} = \tilde{\mathbb{K}}\tilde{\mathbb{C}}|u\rangle + |\tilde{t}_{\text{dipole}}\rangle.$$

Similar to App. 5.8.1, one can define $P_s^{\tilde{Q}}, P_r^{\tilde{Q}}, P_s^{\tilde{C}}, P_r^{\tilde{C}}$ to the new mechanical matrices.

To decompose tension distributions onto SSSs,

$$|\tilde{t}\rangle = \sum_i^{N_{\text{SSS}}} \alpha_i |t_{\text{SSS},i}\rangle = P_s^{\tilde{Q}} \cdot \vec{\alpha},$$

where $\vec{\alpha}$ are coefficients of the linear combination on SSSs.

To calculate the tension distribution,

$$(P_s^{\tilde{Q}})^T |\tilde{t}\rangle = \vec{\alpha},$$

$$(P_r^{\tilde{Q}})^T |\tilde{t}\rangle = \vec{0}.$$

Thus

$$\begin{aligned} \vec{0} &= (P_r^{\tilde{Q}})^T \left(\tilde{\mathbb{K}}\tilde{\mathbb{C}}|u\rangle + |\tilde{t}_{\text{dipole}}\rangle \right) \\ &= (P_r^{\tilde{Q}})^T \tilde{\mathbb{K}} \left(P_r^{\tilde{Q}}(P_r^{\tilde{Q}})^T + P_s^{\tilde{Q}}(P_s^{\tilde{Q}})^T \right) \tilde{\mathbb{Q}}^T |u\rangle + (P_r^{\tilde{Q}})^T |\tilde{t}_{\text{dipole}}\rangle \\ &= (P_r^{\tilde{Q}})^T \tilde{\mathbb{K}} P_r^{\tilde{Q}} (P_r^{\tilde{Q}})^T \tilde{\mathbb{Q}}^T |u\rangle + (P_r^{\tilde{Q}})^T |\tilde{t}_{\text{dipole}}\rangle \\ &= \tilde{\mathbb{K}}_{rr} (P_r^{\tilde{Q}})^T \tilde{\mathbb{Q}}^T |u\rangle + (P_r^{\tilde{Q}})^T |\tilde{t}_{\text{dipole}}\rangle. \end{aligned}$$

As a result, one can have

$$(P_r^{\tilde{Q}})^T \tilde{\mathbb{Q}}^T |u\rangle = - \left(\tilde{\mathbb{K}}_{rr} \right)^{-1} (P_r^{\tilde{Q}})^T |\tilde{t}_{\text{dipole}}\rangle \quad (5.86)$$

Applying $P_r^{\tilde{Q}}$ on both sides of Eq.5.86,

$$\begin{aligned}
P_r^{\tilde{Q}}(P_r^{\tilde{Q}})^T \tilde{Q}^T |u\rangle &= -P_r^{\tilde{Q}} \left(\tilde{\mathbb{K}}_{rr} \right)^{-1} (P_r^{\tilde{Q}})^T |\tilde{t}_{\text{dipole}}\rangle \\
(\text{LHS}) &= \left(\mathbb{I} - P_s^{\tilde{Q}}(P_s^{\tilde{Q}})^T \right) \tilde{Q}^T |u\rangle \\
&= \tilde{Q}^T |u\rangle - P_s^{\tilde{Q}} \left(\tilde{Q} \cdot P_s^{\tilde{Q}} \right)^T |u\rangle \\
&= \tilde{Q}^T |u\rangle
\end{aligned}$$

One can then have the non-local dipole stiffness κ_a as (the force dipole $|f_{\text{dipole}}\rangle = \tilde{Q}|\tilde{t}_{\text{dipole}}\rangle \equiv \tilde{Q}|a\rangle$):

$$\begin{aligned}
\kappa_a &= \frac{2\langle f_{\text{dipole}} | f_{\text{dipole}} \rangle}{-\langle f_{\text{dipole}} | u \rangle} \\
&= \frac{2\langle \tilde{t}_{\text{dipole}} | \tilde{Q}^T \tilde{Q} | \tilde{t}_{\text{dipole}} \rangle}{-\langle \tilde{t}_{\text{dipole}} | \tilde{Q}^T | u \rangle} \\
&= \frac{2\langle \tilde{t}_{\text{dipole}} | \tilde{Q}^T \tilde{Q} | \tilde{t}_{\text{dipole}} \rangle}{\langle \tilde{t}_{\text{dipole}} | P_r^{\tilde{Q}} \left(\tilde{\mathbb{K}}_{rr} \right)^{-1} (P_r^{\tilde{Q}})^T | \tilde{t}_{\text{dipole}} \rangle} \\
&= \frac{2\langle a | \tilde{Q}^T \tilde{Q} | a \rangle}{\langle a | P_r^{\tilde{Q}} \left(\tilde{\mathbb{K}}_{rr} \right)^{-1} (P_r^{\tilde{Q}})^T | a \rangle} \\
&= \frac{4}{\langle a | P_r^{\tilde{Q}} \left(\tilde{\mathbb{K}}_{rr} \right)^{-1} (P_r^{\tilde{Q}})^T | a \rangle},
\end{aligned}$$

where $|a\rangle$ is the vector in the labeling space of bonds (including the auxiliary bond a) which has zeros in all components except for the a -th component is set to unity, and the a -th component is the component corresponding to the auxiliary bond.

The local force dipole response is a special case of non-local force dipole response. When considering local force dipoles, the auxiliary bond a overlaps with bond b . One can show that in this case, the non-local force dipole stiffness reduces to local force dipole stiffness.

5.8.2.3 Local minimum κ in prestressed system

To minimize κ for a local force dipole to bond b associated its arbitrary combination of \parallel and \perp directions, one is to find

$$|e_{\text{ext}}\rangle = \begin{pmatrix} 0 \\ \vdots \\ \cos \theta \\ \sin \theta \cos \phi \\ \sin \theta \sin \phi \\ \vdots \\ 0 \end{pmatrix} \equiv |b\rangle$$

As a result,

$$\begin{aligned} \kappa_b &= \langle b | \mathbb{P} | b \rangle \\ &= \begin{pmatrix} 0 & \cdots & \cos \theta & \sin \theta \cos \phi & \sin \theta \sin \phi & \cdots & 0 \end{pmatrix} \cdot \mathbb{P} \cdot \begin{pmatrix} 0 \\ \vdots \\ \cos \theta \\ \sin \theta \cos \phi \\ \sin \theta \sin \phi \\ \vdots \\ 0 \end{pmatrix} \\ &= \begin{pmatrix} \cos \theta & \sin \theta \cos \phi & \sin \theta \sin \phi \end{pmatrix} \cdot \mathbb{P}_b \cdot \begin{pmatrix} \cos \theta \\ \sin \theta \cos \phi \\ \sin \theta \sin \phi \end{pmatrix} \end{aligned}$$

where \mathbb{P} represents the matrix in between $|b\rangle$ vectors in Eq. (5.85) and \mathbb{P}_b is the b -th 3×3 block diagonal matrix for \mathbb{P} .

To minimize κ_b for the single bond b .

$$\kappa_b^{\min} = \min_{\theta, \phi} \left[\left(\cos \theta \quad \sin \theta \cos \phi \quad \sin \theta \sin \phi \right) \cdot \mathbb{P}_b \cdot \begin{pmatrix} \cos \theta \\ \sin \theta \cos \phi \\ \sin \theta \sin \phi \end{pmatrix} \right]$$

which is a straightforward optimization problem with respect to the two variables θ and ϕ . To solve for such optimization problems in our system, we used the Nelder-Mead simplex algorithm as described in [177].

After optimizing the bond direction to find κ_{\min} , one can see that the direction to obtain the minimum κ corresponds to the direction which has the smallest magnitude of κ_b . In our colloidal systems, this direction usually corresponds to \perp bond directions.

CHAPTER 6

Summary and Outlook

6.1 Conclusions

In this dissertation, we have explored a number of topics related to rigidity and elasticity of both low-density amorphous solids and high-density glasses, beyond the scope of typical isostatic systems like jamming or rigidity percolation. We have shown how correlation controls the rigidity of disordered systems, without changing the critical phenomena of the rigidity transition. We have also examined how pre-stress affects elastic responses of amorphous solids, especially on how the stress-bearing ability of a system evolves as the pre-stress changes, even when the geometry of the system is kept the same.

In Chapter 3, we have discussed the rigidity of structures with introducing correlations/attractions. Both the correlated lattice model and colloidal gel model elucidate that the emergence of rigidity is shifted to lower volume fractions compared with uncorrelated systems. The correlated lattice model suggests that correlation is an irrelevant perturbation to rigidity transition, with the critical exponents unchanged to classical rigidity percolation. Chapter 4 examined the emergence of rigidity in fractal lattices. In this Chapter we show that rigidity can exist even in arbitrarily low volume fraction of solids with the introducing of fractal structures. Rigidity transition in fractal lattices remains in the same universality class with classical rigidity percolation as well as correlated rigidity percolation models. Chapter 3 and Chapter 4 study correlated rigidity percolation, provide a way

of understanding ultra-low-density solids like hydrogels and aerogels, and shed light on designing amorphous solids with “smart” rigidity which reaches solid phase with very low consumption of particles.

Chapter 5 studies the elasticity of glasses, which are above the isostatic point with high densities. We have developed a method to investigate the effect of pre-stress to elastic responses of amorphous solids, and used this method to study the stress-bearing ability of systems based on preparation history. From the study of glasses to macroscopic shear strain and local dipole forces, pre-stressed amorphous solids show qualitatively different behaviors to un-stressed systems, even when the geometry of the system is unchanged. The general method we introduce here is applicable to a wide range of systems, both ordered and disordered, where pre-stress affects elasticity, and provides an efficient computational algorithm for finding the stress distribution when the system is under any load. Thus, it can be applied to yielding and shear thickening/thinning systems such as granular matter and dense suspensions, to potentially shed some light on the dynamical interplay between stress and geometry in these complex materials.

6.2 Outlook

So far We have presented rich phenomena and interesting results on rigidity and elasticity in amorphous solids, especially in low-density and high-density systems beyond isostaticity. There are many more steps to move forward. Below I’m pointing out some potentially interesting directions which can be conducted along the results by this dissertation.

When achieving rigidity in low-density solids, our results suggest that correlation can naturally introduce structural heterogeneity which lowers the rigidity threshold. In the meantime, fractal local structures, which can be introduced by non-equilibrium process of assembling the material, can lower the rigidity threshold to even arbitrarily low volume fractions. It is of great interest to manipulate the route of arranging particles in efficient

ways of transmitting stress to design low-density solids, and is interesting to understand how this occurs in experimental systems.

Since the models of studying correlated rigidity percolation in this dissertation are all in 2-D due to the limitation by the “pebble game” algorithm, it is worth looking at correlated rigidity percolation in 3-D systems, with modified “pebble game” algorithm or other computational efficient methods. 3-D attractive gel models as well as the Sierpiński Tetrahedron FCC lattice (mentioned in Chapter 4) are both interesting next steps based on our current study.

The stressed elasticity method we proposed for glasses take bond transverse directions into account, which have non-negligible impacts on elastic responses when there is pre-stress. SSSs are efficient tools to detect the role of pre-stress, external loads and system geometry in elasticity, thus it is worth looking at different aspects of properties for SSSs, especially their dynamical behaviors. When the geometry is almost intact but pre-stress evolves, it is of great interest to look at the evolution of SSSs under external loads.

With the pre-stress effect on stress-bearing ability captured, it is also of great interest to look at the rearrangement of particles and relate to behaviors in non-linear regime. The evolution of SSSs in pre-stressed systems can help understand yielding, shear thinning, shear thickening and other mechanical behaviors, to shed light on the study of dynamics of dense suspensions.

Mechanical responsiveness is essential to all biological systems down to the level of tissues and cells. Systems with biological rigidity can be used to build force-responsive materials. To design such active systems, correlation and pre-stress are crucial. A further step along this direction is to understand the rigidity in active systems by looking at the biological interactions and the introduced heterogeneity, and to design the elasticity based on the residual stress in systems like biological tissues. It can open the door to various applications like drug delivery, tissue engineering, etc.

It is always challenging to predict the long-time evolution of glassy systems, especially

when they are out of the linear regime. The connection between static properties from initial configurations of amorphous solids and their dynamical behaviors is not obvious. In this context, machine learning is a potentially well-suited tool for detecting the mechanical behaviors. Along the direction of this dissertation, physical interactions and residual stress are essential input features for supervised learning machines, for example support vector machines (SVMs), to obtain excellent predictive power on the elasticity of glassy systems. In the meantime, a state-of-art machine learning method in glassy systems by graph neural networks (GNN) [178], has shown impressive empirical performance but is still nevertheless a black-box function modeling method. As a result, it is also of great interest to look at the evolution of SSSs in the learned neural network structures, which can shed light on understanding the machine learning predictive power on glassy systems from the perspective of their physical properties.

BIBLIOGRAPHY

- [1] D. Jacobs and M. Thorpe, “Generic rigidity percolation in two dimensions,” *Physical Review E*, vol. 53, no. 4, p. 3682, 1996.
- [2] D. J. Jacobs and M. F. Thorpe, “Generic rigidity percolation: the pebble game,” *Physical review letters*, vol. 75, no. 22, p. 4051, 1995.
- [3] J. C. Maxwell, “L. on the calculation of the equilibrium and stiffness of frames,” *The London, Edinburgh, and Dublin Philosophical Magazine and Journal of Science*, vol. 27, no. 182, pp. 294–299, 1864.
- [4] C. R. Calladine, “Buckminster fuller’s “tensegrity” structures and clerk maxwell’s rules for the construction of stiff frames,” *International journal of solids and structures*, vol. 14, no. 2, pp. 161–172, 1978.
- [5] M. F. Thorpe, “Continuous deformations in random networks,” *Journal of Non-Crystalline Solids*, vol. 57, no. 3, pp. 355–370, 1983.
- [6] T. C. Lubensky, C. L. Kane, X. Mao, A. Souslov, and K. Sun, “Phonons and elasticity in critically coordinated lattices,” *Reports on Progress in Physics*, vol. 78, no. 7, p. 073901, 2015.
- [7] S. Guest and J. Hutchinson, “On the determinacy of repetitive structures,” *Journal of the Mechanics and Physics of Solids*, vol. 51, no. 3, pp. 383–391, 2003.
- [8] J. Heyman, *The science of structural engineering*. World Scientific, 1999.
- [9] A. Kassimali, *Structural analysis*. Cengage Learning, 2009.
- [10] S. Feng and P. N. Sen, “Percolation on elastic networks: new exponent and threshold,” *Physical review letters*, vol. 52, no. 3, p. 216, 1984.
- [11] S. Feng, P. Sen, B. Halperin, and C. Lobb, “Percolation on two-dimensional elastic networks with rotationally invariant bond-bending forces,” *Physical Review B*, vol. 30, no. 9, p. 5386, 1984.
- [12] W. G. Ellenbroek and X. Mao, “Rigidity percolation on the square lattice,” *Europhys. Lett.*, vol. 96, p. 540002, 2011.

- [13] L. Zhang, D. Z. Rocklin, B. G.-g. Chen, and X. Mao, “Rigidity percolation by next-nearest-neighbor bonds on generic and regular isostatic lattices,” *Phys. Rev. E*, vol. 91, p. 032124, Mar 2015.
- [14] A. J. Liu and S. R. Nagel, “Jamming is not just cool any more,” *Nature*, vol. 396, no. 6706, pp. 21–22, 1998.
- [15] M. Wyart, “On the rigidity of amorphous solids,” *arXiv preprint cond-mat/0512155*, 2005.
- [16] M. Wyart, S. R. Nagel, and T. A. Witten, “Geometric origin of excess low-frequency vibrational modes in weakly connected amorphous solids,” *EPL (Europhysics Letters)*, vol. 72, no. 3, p. 486, 2005.
- [17] M. van Hecke, “Jamming of soft particles: geometry, mechanics, scaling and isotaticity,” *Journal of Physics: Condensed Matter*, vol. 22, no. 3, p. 033101, 2009.
- [18] A. J. Liu and S. R. Nagel, “The jamming transition and the marginally jammed solid,” *Annu. Rev. Condens. Matter Phys.*, vol. 1, no. 1, pp. 347–369, 2010.
- [19] A. Souslov, A. J. Liu, and T. C. Lubensky, “Elasticity and response in nearly isostatic periodic lattices,” *Physical review letters*, vol. 103, no. 20, p. 205503, 2009.
- [20] X. Mao, N. Xu, and T. C. Lubensky, “Soft modes and elasticity of nearly isostatic lattices: Randomness and dissipation,” *Phys. Rev. Lett.*, vol. 104, p. 085504, 2010.
- [21] X. Mao and T. C. Lubensky, “Coherent potential approximation of random nearly isostatic kagome lattice,” *Physical Review E*, vol. 83, no. 1, p. 011111, 2011.
- [22] C. P. Broedersz and F. C. MacKintosh, “Modeling semiflexible polymer networks,” *Reviews of Modern Physics*, vol. 86, no. 3, p. 995, 2014.
- [23] D. A. Head, A. J. Levine, and F. MacKintosh, “Deformation of cross-linked semiflexible polymer networks,” *Physical review letters*, vol. 91, no. 10, p. 108102, 2003.
- [24] J. Wilhelm and E. Frey, “Elasticity of stiff polymer networks,” *Physical review letters*, vol. 91, no. 10, p. 108103, 2003.
- [25] C. Heussinger and E. Frey, “Floppy modes and nonaffine deformations in random fiber networks,” *Physical review letters*, vol. 97, no. 10, p. 105501, 2006.
- [26] C. Heussinger, B. Schaefer, and E. Frey, “Nonaffine rubber elasticity for stiff polymer networks,” *Physical Review E*, vol. 76, no. 3, p. 031906, 2007.
- [27] E. Huisman and T. C. Lubensky, “Internal stresses, normal modes, and nonaffinity in three-dimensional biopolymer networks,” *Physical review letters*, vol. 106, no. 8, p. 088301, 2011.
- [28] C. P. Broedersz, X. Mao, T. C. Lubensky, and F. C. MacKintosh, “Criticality and isotaticity in fibre networks,” *Nature Physics*, vol. 7, no. 12, p. 983, 2011.

- [29] X. Mao, O. Stenull, and T. C. Lubensky, “Elasticity of a filamentous kagome lattice,” *Physical Review E*, vol. 87, no. 4, p. 042602, 2013.
- [30] J. Phillips, “Topology of covalent non-crystalline solids ii: Medium-range order in chalcogenide alloys and a si (ge),” *Journal of Non-Crystalline Solids*, vol. 43, no. 1, pp. 37–77, 1981.
- [31] M. Thorpe, “Rigidity percolation in glassy structures,” *Journal of Non-Crystalline Solids*, vol. 76, no. 1, pp. 109–116, 1985.
- [32] C. S. O’hern, L. E. Silbert, A. J. Liu, and S. R. Nagel, “Jamming at zero temperature and zero applied stress: The epitome of disorder,” *Physical Review E*, vol. 68, no. 1, p. 011306, 2003.
- [33] C. Kane and T. Lubensky, “Topological boundary modes in isostatic lattices,” *Nature Physics*, vol. 10, no. 1, pp. 39–45, 2014.
- [34] X. Mao and T. C. Lubensky, “Maxwell lattices and topological mechanics,” *Annual Review of Condensed Matter Physics*, vol. 9, pp. 413–433, 2018.
- [35] D. Bi, J. Zhang, B. Chakraborty, and R. P. Behringer, “Jamming by shear,” *Nature*, vol. 480, no. 7377, pp. 355–358, 2011.
- [36] K. Shundyak, M. van Hecke, and W. van Saarloos, “Force mobilization and generalized isostaticity in jammed packings of frictional grains,” *Physical Review E*, vol. 75, no. 1, p. 010301, 2007.
- [37] S. Henkes, M. van Hecke, and W. van Saarloos, “Critical jamming of frictional grains in the generalized isostaticity picture,” *EPL (Europhysics Letters)*, vol. 90, no. 1, p. 14003, 2010.
- [38] S. Henkes, D. A. Quint, Y. Fily, and J. Schwarz, “Rigid cluster decomposition reveals criticality in frictional jamming,” *Physical review letters*, vol. 116, no. 2, p. 028301, 2016.
- [39] K. Liu, S. Henkes, and J. Schwarz, “Frictional Rigidity Percolation: A New Universality Class and Its Superuniversal Connections through Minimal Rigidity Proliferation,” *Phys. Rev. X*, vol. 9, p. 021006, Apr. 2019. Publisher: American Physical Society.
- [40] E. Zaccarelli, “Colloidal gels: equilibrium and non-equilibrium routes,” *Journal of Physics: Condensed Matter*, vol. 19, no. 32, p. 323101, 2007.
- [41] P. J. Lu, E. Zaccarelli, F. Ciulla, A. B. Schofield, F. Sciortino, and D. A. Weitz, “Gelation of particles with short-range attraction,” *Nature*, vol. 453, no. 7194, p. 499, 2008.
- [42] P. J. Flory, “Molecular size distribution in three dimensional polymers. i. gelation1,” *Journal of the American Chemical Society*, vol. 63, no. 11, pp. 3083–3090, 1941.

- [43] W. H. Stockmayer, “Theory of molecular size distribution and gel formation in branched polymers ii. general cross linking,” *The Journal of Chemical Physics*, vol. 12, no. 4, pp. 125–131, 1944.
- [44] D. Stauffer and A. Aharony, *Introduction to percolation theory: revised second edition*. CRC press, 2014.
- [45] S. Zhang, L. Zhang, M. Bouzid, D. Z. Rocklin, E. Del Gado, and X. Mao, “Correlated Rigidity Percolation and Colloidal Gels,” *Phys. Rev. Lett.*, vol. 123, p. 058001, July 2019. Publisher: American Physical Society.
- [46] S. Machlus, S. Zhang, and X. Mao, “Correlated rigidity percolation in fractal lattices,” *Physical Review E*, vol. 103, no. 1, p. 012104, 2021.
- [47] D. J. Jacobs and B. Hendrickson, “An algorithm for two-dimensional rigidity percolation: the pebble game,” *Journal of Computational Physics*, vol. 137, no. 2, pp. 346–365, 1997.
- [48] G. Laman, “On graphs and rigidity of plane skeletal structures,” *Journal of Engineering mathematics*, vol. 4, no. 4, pp. 331–340, 1970.
- [49] J. Machta, Y. Choi, A. Lucke, T. Schweizer, and L. Chayes, “Invaded cluster algorithm for potts models,” *Physical Review E*, vol. 54, no. 2, p. 1332, 1996.
- [50] M. E. Newman and R. M. Ziff, “Fast monte carlo algorithm for site or bond percolation,” *Physical Review E*, vol. 64, no. 1, p. 016706, 2001.
- [51] <https://www.caam.rice.edu/software/ARPACK/>.
- [52] C. P. Goodrich, “Unearthing the anticrystal: criticality in the linear response of disordered solids,” *arXiv preprint arXiv:1510.08820*, 2015.
- [53] L. V. Foster and T. A. Davis, “Algorithm 933: Reliable calculation of numerical rank, null space bases, pseudoinverse solutions, and basic solutions using suitesparseqr,” *ACM Transactions on Mathematical Software (TOMS)*, vol. 40, no. 1, pp. 1–23, 2013.
- [54] T. A. Davis, “Algorithm 915, suitesparseqr: Multifrontal multithreaded rank-revealing sparse qr factorization,” *ACM Transactions on Mathematical Software (TOMS)*, vol. 38, no. 1, pp. 1–22, 2011.
- [55] <https://people.engr.tamu.edu/davis/suitesparse.html>.
- [56] R. L. Truby and J. A. Lewis, “Printing soft matter in three dimensions,” *Nature*, vol. 540, no. 7633, p. 371, 2016.
- [57] R. Mezzenga, P. Schurtenberger, A. Burbidge, and M. Michel, “Understanding foods as soft materials,” *Nature materials*, vol. 4, no. 10, p. 729, 2005.

- [58] B. Keshavarz, T. Divoux, S. Manneville, and G. H. McKinley, “Nonlinear viscoelasticity and generalized failure criterion for polymer gels,” *ACS Macro Letters*, vol. 6, no. 7, pp. 663–667, 2017.
- [59] H. He and M. F. Thorpe, “Elastic properties of glasses,” *Physical Review Letters*, vol. 54, no. 19, p. 2107, 1985.
- [60] M. Sahimi, “Non-linear and non-local transport processes in heterogeneous media: from long-range correlated percolation to fracture and materials breakdown,” *Physics Reports*, vol. 306, no. 4-6, pp. 213–395, 1998.
- [61] M. Thorpe, D. Jacobs, M. Chubynsky, and J. Phillips, “Self-organization in network glasses,” *Journal of Non-Crystalline Solids*, vol. 266, pp. 859–866, 2000.
- [62] M. Bauchy and M. Micoulaut, “Atomic scale foundation of temperature-dependent bonding constraints in network glasses and liquids,” *Journal of Non-Crystalline Solids*, vol. 357, no. 14, pp. 2530–2537, 2011.
- [63] W. G. Ellenbroek, V. F. Hagh, A. Kumar, M. Thorpe, and M. Van Hecke, “Rigidity loss in disordered systems: Three scenarios,” *Physical review letters*, vol. 114, no. 13, p. 135501, 2015.
- [64] M. Chubynsky and M. F. Thorpe, “Algorithms for three-dimensional rigidity analysis and a first-order percolation transition,” *Physical Review E*, vol. 76, no. 4, p. 041135, 2007.
- [65] V. Trappe, V. Prasad, L. Cipelletti, P. Segre, and D. A. Weitz, “Jamming phase diagram for attractive particles,” *Nature*, vol. 411, no. 6839, p. 772, 2001.
- [66] S. Manley, L. Cipelletti, V. Trappe, A. Bailey, R. Christianson, U. Gasser, V. Prasad, P. Segre, M. Doherty, S. Sankaran, *et al.*, “Limits to gelation in colloidal aggregation,” *Physical review letters*, vol. 93, no. 10, p. 108302, 2004.
- [67] P. Boolchand, D. Georgiev, and B. Goodman, “Discovery of the intermediate phase in chalcogenide glasses,” *Journal of Optoelectronics and Advanced Materials*, vol. 3, no. 3, pp. 703–720, 2001.
- [68] C. P. Goodrich, A. J. Liu, and S. R. Nagel, “Finite-size scaling at the jamming transition,” *Physical review letters*, vol. 109, no. 9, p. 095704, 2012.
- [69] D. M. Sussman, C. P. Goodrich, and A. J. Liu, “Spatial structure of states of self stress in jammed systems,” *Soft matter*, vol. 12, no. 17, pp. 3982–3990, 2016.
- [70] D. J. Koeze and B. P. Tighe, “Sticky matter: Jamming and rigid cluster statistics with attractive particle interactions,” *arXiv:1807.06526 [cond-mat.soft]*, 06 2018.
- [71] G. Lois, J. Blawdziewicz, and C. S. O’Hern, “Jamming transition and new percolation universality classes in particulate systems with attraction,” *Physical review letters*, vol. 100, no. 2, p. 028001, 2008.

- [72] D. A. Head, “Well defined transition to gel-like aggregates of attractive athermal particles,” *The European Physical Journal E*, vol. 22, pp. 151–155, Feb 2007.
- [73] I. Jorjadze, L.-L. Pontani, K. A. Newhall, and J. Brujić, “Attractive emulsion droplets probe the phase diagram of jammed granular matter,” *Proceedings of the National Academy of Sciences*, vol. 108, no. 11, pp. 4286–4291, 2011.
- [74] T. A. Witten and P. Pincus, *Structured fluids: polymers, colloids, surfactants*. Oxford University Press, 2004.
- [75] J.-P. Hansen and I. R. McDonald, *Theory of simple liquids*. Elsevier, 1990.
- [76] D. Richard, J. Hallett, T. Speck, and C. P. Royall, “Coupling between criticality and gelation in “sticky” spheres: a structural analysis,” *Soft matter*, 2018.
- [77] P. G. de Gennes, *Scaling concepts in polymer physics*. Ithaca, N.Y.: Cornell University Press, 1979.
- [78] A. Dinsmore and D. Weitz, “Direct imaging of three-dimensional structure and topology of colloidal gels,” *Journal of Physics: Condensed Matter*, vol. 14, no. 33, p. 7581, 2002.
- [79] E. Del Gado, A. Fierro, L. de Arcangelis, and A. Coniglio, “Slow dynamics in gelation phenomena: From chemical gels to colloidal glasses,” *Phys. Rev. E*, vol. 69, no. 5, p. 051103, 2004.
- [80] P. N. Segrè, V. Prasad, A. B. Schofield, and D. A. Weitz, “Glasslike Kinetic Arrest at the Colloidal-Gelation Transition,” *Phys. Rev. Lett.*, vol. 86, pp. 6042–6045, June 2001.
- [81] K. Broderix, H. Löwe, P. Müller, and A. Zippelius, “Critical dynamics of gelation,” *Physical Review E*, vol. 63, no. 1, p. 011510, 2000.
- [82] K. Kroy, M. Cates, and W. Poon, “Cluster mode-coupling approach to weak gelation in attractive colloids,” *Physical review letters*, vol. 92, no. 14, p. 148302, 2004.
- [83] R. Ball, D. Weitz, T. Witten, and F. Leyvraz, “Universal kinetics in reaction-limited aggregation,” *Physical review letters*, vol. 58, no. 3, p. 274, 1987.
- [84] M. Lin, H. Lindsay, D. Weitz, R. Ball, R. Klein, and P. Meakin, “Universality in colloid aggregation,” *Nature*, vol. 339, no. 6223, p. 360, 1989.
- [85] M. E. Cates, M. Fuchs, K. Kroy, W. C. Poon, and A. M. Puertas, “Theory and simulation of gelation, arrest and yielding in attracting colloids,” *Journal of Physics: Condensed Matter*, vol. 16, no. 42, p. S4861, 2004.
- [86] C. P. Royall, S. R. Williams, T. Ohtsuka, and H. Tanaka, “Direct observation of a local structural mechanism for dynamic arrest,” *Nature materials*, vol. 7, no. 7, p. 556, 2008.

- [87] N. E. Valadez-Pérez, Y. Liu, A. P. Eberle, N. J. Wagner, and R. Castaneda-Priego, “Dynamical arrest in adhesive hard-sphere dispersions driven by rigidity percolation,” *Physical Review E*, vol. 88, no. 6, p. 060302, 2013.
- [88] A. Zaccone, H. Winter, M. Siebenbürger, and M. Ballauff, “Linking self-assembly, rheology, and gel transition in attractive colloids,” *Journal of Rheology*, vol. 58, no. 5, pp. 1219–1244, 2014.
- [89] L. Hsiao, R. S. Newman, S. C. Glotzer, and M. J. Solomon, “Role of isostaticity and load-bearing microstructure in the elasticity of yielded colloidal gels,” *Proceedings of the National Academy of Sciences*, vol. 109, no. 40, pp. 16029–16034, 2012.
- [90] H. Tsurusawa, M. Leocmach, J. Russo, and H. Tanaka, “Gelation as condensation frustrated by hydrodynamics and mechanical isostaticity,” *arXiv preprint arXiv:1804.04370*, 04 2018.
- [91] D. Z. Rocklin, L. C. Hsiao, M. Szakasits, M. J. Solomon, and X. Mao, “Elasticity of colloidal gels: structural heterogeneity, floppy modes, and rigidity,” *manuscript in preparation*, 2018.
- [92] V. J. Anderson and H. N. Lekkerkerker, “Insights into phase transition kinetics from colloid science,” *Nature*, vol. 416, no. 6883, p. 811, 2002.
- [93] M. Bantawa, M. Bouzid, and E. Del Gado, “Computational studies of soft particle gels: numerical models.,” *Manuscript in preparation.*, 2018.
- [94] R. N. Zia, B. J. Landrum, and W. B. Russel, “A micro-mechanical study of coarsening and rheology of colloidal gels: Cage building, cage hopping, and smoluchowski’s ratchet,” *Journal of Rheology*, vol. 58, no. 5, pp. 1121–1157, 2014.
- [95] E. D. Gado, D. Fiocco, G. Foffi, S. Manley, V. Trappe, and A. Zaccone, “Colloidal gelation,” *Fluids, Colloids and Soft Materials: An Introduction to Soft Matter Physics*, pp. 279–291, 2016.
- [96] V. Prasad, V. Trappe, A. Dinsmore, P. Segre, L. Cipelletti, and D. Weitz, “Rideal lecture universal features of the fluid to solid transition for attractive colloidal particles,” *Faraday Discussions*, vol. 123, pp. 1–12, 2003.
- [97] A. Dinsmore, V. Prasad, I. Wong, and D. Weitz, “Microscopic structure and elasticity of weakly aggregated colloidal gels,” *Physical review letters*, vol. 96, no. 18, p. 185502, 2006.
- [98] J. P. Pantina and E. M. Furst, “Elasticity and critical bending moment of model colloidal aggregates,” *Physical review letters*, vol. 94, no. 13, p. 138301, 2005.
- [99] C. J. Dibble, M. Kogan, and M. J. Solomon, “Structural origins of dynamical heterogeneity in colloidal gels,” *Phys. Rev. E*, vol. 77, p. 050401, 2008.

- [100] T. Ohtsuka, C. P. Royall, and H. Tanaka, “Local structure and dynamics in colloidal fluids and gels,” *EPL (Europhysics Letters)*, vol. 84, no. 4, p. 46002, 2008.
- [101] E. Del Gado and W. Kob, “A microscopic model for colloidal gels with directional effective interactions: network induced glassy dynamics,” *Soft Matter*, vol. 6, no. 7, pp. 1547–1558, 2010.
- [102] J. Colombo and E. Del Gado, “Self-assembly and cooperative dynamics of a model colloidal gel network,” *Soft matter*, vol. 10, no. 22, pp. 4003–4015, 2014.
- [103] J. Colombo and E. Del Gado, “Stress localization, stiffening, and yielding in a model colloidal gel,” *Journal of rheology*, vol. 58, no. 5, pp. 1089–1116, 2014.
- [104] D. Frenkel and B. Smit, “Understanding molecular simulation: From algorithms to applications,” 2002.
- [105] M. G. Noro and D. Frenkel, “Extended corresponding-states behavior for particles with variable range attractions,” *The Journal of Chemical Physics*, vol. 113, no. 8, pp. 2941–2944, 2000.
- [106] S. Plimpton, “Fast parallel algorithms for short-range molecular dynamics,” *Journal of computational physics*, vol. 117, no. 1, pp. 1–19, 1995.
- [107] P. J. Steinhardt, D. R. Nelson, and M. Ronchetti, “Bond-orientational order in liquids and glasses,” *Physical Review B*, vol. 28, no. 2, p. 784, 1983.
- [108] A. Coniglio, H. E. Stanley, and W. Klein, “Site-bond correlated-percolation problem: a statistical mechanical model of polymer gelation,” *Physical Review Letters*, vol. 42, no. 8, p. 518, 1979.
- [109] A. Coniglio, “Cluster size and shape in random and correlated percolation,” *Journal of Physics A: Mathematical and General*, vol. 12, no. 4, p. 545, 1979.
- [110] T. A. Witten and L. M. Sander, “Diffusion-limited aggregation, a kinetic critical phenomenon,” *Phys. Rev. Lett.*, vol. 47, pp. 1400–1403, Nov 1981.
- [111] H. Ricateau, L. F. Cugliandolo, and M. Picco, “Critical percolation in the slow cooling of the bi-dimensional ferromagnetic ising model,” *Journal of Statistical Mechanics: Theory and Experiment*, vol. 2018, no. 1, p. 013201, 2018.
- [112] M. Bouzid and E. Del Gado, “Network topology in soft gels: Hardening and softening materials,” *Langmuir*, vol. 34, no. 3, pp. 773–781, 2017.
- [113] V. Trappe and P. Sandkühler, “Colloidal gels—low-density disordered solid-like states,” *Current Opinion in Colloid & Interface Science*, vol. 8, pp. 494–500, Apr. 2004.
- [114] H. Tsurusawa, M. Leocmach, J. Russo, and H. Tanaka, “Direct link between mechanical stability in gels and percolation of isostatic particles,” *Science Advances*, vol. 5, May 2019.

- [115] A. R. Wufsus, N. E. Macera, and K. B. Neeves, “The hydraulic permeability of blood clots as a function of fibrin and platelet density,” *Biophys. J.*, vol. 104, pp. 1812–1823, Apr. 2013.
- [116] J. A. Michel and P. J. Yunker, “Structural hierarchy confers error tolerance in biological materials,” *PNAS*, vol. 116, pp. 2875–2880, Feb. 2019. Publisher: National Academy of Sciences Section: Physical Sciences.
- [117] J. H. Cho, R. Cerbino, and I. Bischofberger, “Emergence of Multiscale Dynamics in Colloidal Gels,” *Phys. Rev. Lett.*, vol. 124, p. 088005, Feb. 2020.
- [118] M. Carpineti and M. Giglio, “Spinodal-type dynamics in fractal aggregation of colloidal clusters,” *Phys. Rev. Lett.*, vol. 68, pp. 3327–3330, Jun 1992.
- [119] T. Gisler, R. C. Ball, and D. A. Weitz, “Strain hardening of fractal colloidal gels,” *Phys. Rev. Lett.*, vol. 82, pp. 1064–1067, Feb 1999.
- [120] P. A. Evans, K. Hawkins, R. H. K. Morris, N. Thirumalai, R. Munro, L. Wakeman, M. J. Lawrence, and P. R. Williams, “Gel point and fractal microstructure of incipient blood clots are significant new markers of hemostasis for healthy and anticoagulated blood,” *Blood*, vol. 116, pp. 3341–3346, Oct. 2010.
- [121] J. Vermant and M. Solomon, “Flow-induced structure in colloidal suspensions,” *Journal of Physics: Condensed Matter*, vol. 17, no. 4, p. R187, 2005.
- [122] Y. Gefen, A. Aharony, Y. Shapir, and B. B. Mandelbrot, “Phase transitions on fractals. II. Sierpinski gaskets,” *Journal of Physics A Mathematical General*, vol. 17, pp. 435–444, Feb. 1984.
- [123] J. H. Luscombe and R. C. Desai, “Statistical mechanics of a fractal lattice: Renormalization-group analysis of the Sierpinski gasket,” *Physical Review B*, vol. 32, pp. 1614–1627, Aug. 1985.
- [124] E. L. da Rocha and C. R. da Cunha, “The transition from fracton to phonon states in a Sierpinski triangle lattice,” *Chaos, Solitons & Fractals*, vol. 44, pp. 241–247, May 2011.
- [125] K.-W. Yu, “Vibrational spectrum on an exact fractal lattice,” *Physica A Statistical Mechanics and its Applications*, vol. 128, pp. 307–317, Nov. 1984.
- [126] R. Burioni, D. Cassi, M. P. Fontana, and A. Vulpiani, “Vibrational thermodynamic instability of recursive networks,” *EPL*, vol. 58, p. 806, June 2002.
- [127] S. H. Liu and A. J. Liu, “Spectral dimension of elastic Sierpinski gaskets with general elastic forces,” *Phys. Rev. B*, vol. 32, pp. 4753–4755, Oct. 1985. Publisher: American Physical Society.
- [128] S. H. Liu, “Spectral dimension of elastic Sierpinski gaskets,” *Physical Review B*, vol. 30, pp. 4045–4047, Oct. 1984.

- [129] <https://github.com/shaemachlus/Fractal-correlation-RP>.
- [130] M. E. Cates, J. P. Wittmer, J. P. Bouchaud, and P. Claudin, “Jamming, force chains, and fragile matter,” *Physical review letters*, vol. 81, no. 9, p. 1841, 1998.
- [131] L. Zhang, D. Z. Rocklin, L. M. Sander, and X. Mao, “Fiber networks below the isostatic point: Fracture without stress concentration,” *Phys. Rev. Materials*, vol. 1, p. 052602, Oct 2017.
- [132] L. Zhang and X. Mao, “Fracturing of topological maxwell lattices,” *New Journal of Physics*, vol. 20, no. 6, p. 063034, 2018.
- [133] S. Alexander, “Amorphous solids: their structure, lattice dynamics and elasticity,” *Physics reports*, vol. 296, no. 2-4, pp. 65–236, 1998.
- [134] M. Gei, A. B. Movchan, and D. Bigoni, “Band-gap shift and defect-induced annihilation in prestressed elastic structures,” *Journal of Applied Physics*, vol. 105, no. 6, p. 063507, 2009.
- [135] Z. Chen, Q. Guo, C. Majidi, W. Chen, D. J. Srolovitz, and M. P. Haataja, “Nonlinear geometric effects in mechanical bistable morphing structures,” *Phys. Rev. Lett.*, vol. 109, p. 114302, Sep 2012.
- [136] F. Fraternali, G. Carpentieri, A. Amendola, R. E. Skelton, and V. F. Nesterenko, “Multiscale tunability of solitary wave dynamics in tensegrity metamaterials,” *Applied Physics Letters*, vol. 105, no. 20, p. 201903, 2014.
- [137] A. S. Meeussen, E. C. Oğuz, M. van Hecke, and Y. Shokef, “Response evolution of mechanical metamaterials under architectural transformations,” *New Journal of Physics*, vol. 22, p. 023030, feb 2020.
- [138] C. Merrigan, C. Nisoli, and Y. Shokef, “Topologically protected steady cycles in an icelike mechanical metamaterial,” *Phys. Rev. Research*, vol. 3, p. 023174, Jun 2021.
- [139] S. Armon, E. Efrati, R. Kupferman, and E. Sharon, “Geometry and mechanics in the opening of chiral seed pods,” *Science*, vol. 333, no. 6050, pp. 1726–1730, 2011.
- [140] M. A. Wyczalkowski, Z. Chen, B. A. Filas, V. D. Varner, and L. A. Taber, “Computational models for mechanics of morphogenesis,” *Birth Defects Research Part C: Embryo Today: Reviews*, vol. 96, no. 2, pp. 132–152, 2012.
- [141] M. Wyart, L. E. Silbert, S. R. Nagel, and T. A. Witten, “Effects of compression on the vibrational modes of marginally jammed solids,” *Phys. Rev. E*, vol. 72, p. 051306, Nov 2005.
- [142] E. DeGiuli, A. Laversanne-Finot, G. Düring, E. Lerner, and M. Wyart, “Effects of coordination and pressure on sound attenuation, boson peak and elasticity in amorphous solids,” *Soft Matter*, vol. 10, pp. 5628–5644, 2014.

- [143] W. G. Ellenbroek, M. van Hecke, and W. van Saarloos, “Jammed frictionless disks: Connecting local and global response,” *Phys. Rev. E*, vol. 80, p. 061307, Dec 2009.
- [144] A. J. Licup, S. Münster, A. Sharma, M. Sheinman, L. M. Jawerth, B. Fabry, D. A. Weitz, and F. C. MacKintosh, “Stress controls the mechanics of collagen networks,” *Proceedings of the National Academy of Sciences*, vol. 112, no. 31, pp. 9573–9578, 2015.
- [145] L. Yan and D. Bi, “Multicellular rosettes drive fluid-solid transition in epithelial tissues,” *Phys. Rev. X*, vol. 9, p. 011029, Feb 2019.
- [146] M. Merkel, K. Baumgarten, B. P. Tighe, and M. L. Manning, “A minimal-length approach unifies rigidity in underconstrained materials,” *Proceedings of the National Academy of Sciences*, vol. 116, no. 14, pp. 6560–6568, 2019.
- [147] H. Liu, D. Zhou, L. Zhang, D. K. Lubensky, and X. Mao, “Topological floppy modes in epithelial tissues,” *arXiv preprint arXiv:2104.14743*, 2021.
- [148] J. Alvarado, M. Sheinman, A. Sharma, F. C. MacKintosh, and G. H. Koenderink, “Molecular motors robustly drive active gels to a critically connected state,” *Nature Physics*, vol. 9, no. 9, pp. 591–597, 2013.
- [149] P. Ronceray, C. P. Broedersz, and M. Lenz, “Fiber networks amplify active stress,” *Proceedings of the national academy of sciences*, vol. 113, no. 11, pp. 2827–2832, 2016.
- [150] S. F. Edwards and R. Oakeshott, “Theory of powders,” *Physica A: Statistical Mechanics and its Applications*, vol. 157, no. 3, pp. 1080–1090, 1989.
- [151] R. Blumenfeld and S. F. Edwards, “Granular entropy: Explicit calculations for planar assemblies,” *Physical review letters*, vol. 90, no. 11, p. 114303, 2003.
- [152] J. H. Snoeijer, T. J. H. Vlugt, M. van Hecke, and W. van Saarloos, “Force network ensemble: A new approach to static granular matter,” *Phys. Rev. Lett.*, vol. 92, p. 054302, Feb 2004.
- [153] B. P. Tighe, A. R. T. van Eerd, and T. J. H. Vlugt, “Entropy maximization in the force network ensemble for granular solids,” *Phys. Rev. Lett.*, vol. 100, p. 238001, Jun 2008.
- [154] B. P. Tighe, J. H. Snoeijer, T. J. Vlugt, and M. van Hecke, “The force network ensemble for granular packings,” *Soft Matter*, vol. 6, no. 13, pp. 2908–2917, 2010.
- [155] D. Bi, S. Henkes, K. E. Daniels, and B. Chakraborty, “The statistical physics of athermal materials,” *Annual Review of Condensed Matter Physics*, vol. 6, no. 1, pp. 63–83, 2015.
- [156] X. Mao, P. M. Goldbart, X. Xing, and A. Zippelius, “Elastic heterogeneity of soft random solids,” *Europhysics Letters (EPL)*, vol. 80, p. 26004, oct 2007.

- [157] S. Henkes and B. Chakraborty, “Statistical mechanics framework for static granular matter,” *Phys. Rev. E*, vol. 79, p. 061301, Jun 2009.
- [158] X. Mao, P. M. Goldbart, X. Xing, and A. Zippelius, “Soft random solids and their heterogeneous elasticity,” *Phys. Rev. E*, vol. 80, p. 031140, Sep 2009.
- [159] A. Lemaître, “Inherent stress correlations in a quiescent two-dimensional liquid: Static analysis including finite-size effects,” *Phys. Rev. E*, vol. 96, p. 052101, Nov 2017.
- [160] E. DeGiuli, “Field theory for amorphous solids,” *Phys. Rev. Lett.*, vol. 121, p. 118001, Sep 2018.
- [161] J. N. Nampoothiri, Y. Wang, K. Ramola, J. Zhang, S. Bhattacharjee, and B. Chakraborty, “Emergent elasticity in amorphous solids,” *Phys. Rev. Lett.*, vol. 125, p. 118002, Sep 2020.
- [162] S. Pellegrino and C. R. Calladine, “Matrix analysis of statically and kinematically indeterminate frameworks,” *International Journal of Solids and Structures*, vol. 22, no. 4, pp. 409–428, 1986.
- [163] K. Sun, A. Souslov, X. Mao, and T. Lubensky, “Surface phonons, elastic response, and conformal invariance in twisted kagome lattices,” *Proceedings of the National Academy of Sciences*, vol. 109, no. 31, pp. 12369–12374, 2012.
- [164] J. Paulose, A. S. Meeussen, and V. Vitelli, “Selective buckling via states of self-stress in topological metamaterials,” *Proceedings of the National Academy of Sciences*, vol. 112, no. 25, pp. 7639–7644, 2015.
- [165] M. Born, K. Huang, and M. Lax, “Dynamical theory of crystal lattices,” *American Journal of Physics*, vol. 23, no. 7, pp. 474–474, 1955.
- [166] B. DiDonna and T. Lubensky, “Nonaffine correlations in random elastic media,” *Physical Review E*, vol. 72, no. 6, p. 066619, 2005.
- [167] R. Connelly and W. Whiteley, “The stability of tensegrity frameworks,” *International Journal of Space Structures*, vol. 7, no. 2, pp. 153–163, 1992.
- [168] R. Connelly and W. Whiteley, “Second-order rigidity and prestress stability for tensegrity frameworks,” *SIAM Journal on Discrete Mathematics*, vol. 9, no. 3, pp. 453–491, 1996.
- [169] M. Wyart, H. Liang, A. Kabla, and L. Mahadevan, “Elasticity of floppy and stiff random networks,” *Physical review letters*, vol. 101, no. 21, p. 215501, 2008.
- [170] M. F. Vermeulen, A. Bose, C. Storm, and W. G. Ellenbroek, “Geometry and the onset of rigidity in a disordered network,” *Physical Review E*, vol. 96, no. 5, p. 053003, 2017.

- [171] O. K. Damavandi, V. F. Hagh, C. D. Santangelo, and M. L. Manning, “Energetic rigidity: a unifying theory of mechanical stability,” *arXiv preprint arXiv:2102.11310*, 2021.
- [172] E. Lerner, “Quasilocalized states of self stress in packing-derived networks,” *The European Physical Journal E*, vol. 41, no. 8, pp. 1–9, 2018.
- [173] J. D. Weeks, D. Chandler, and H. C. Andersen, “Role of repulsive forces in determining the equilibrium structure of simple liquids,” *The Journal of chemical physics*, vol. 54, no. 12, pp. 5237–5247, 1971.
- [174] V. V. Vasisht and E. Del Gado, “Computational study of transient shear banding in soft jammed solids,” *Physical Review E*, vol. 102, no. 1, p. 012603, 2020.
- [175] V. V. Vasisht, G. Roberts, and E. Del Gado, “Emergence and persistence of flow inhomogeneities in the yielding and fluidization of dense soft solids,” *Physical Review E*, vol. 102, no. 1, p. 010604, 2020.
- [176] B. Hopkins and J. G. Skellam, “A new method for determining the type of distribution of plant individuals,” *Annals of Botany*, vol. 18, no. 2, pp. 213–227, 1954.
- [177] J. C. Lagarias, J. A. Reeds, M. H. Wright, and P. E. Wright, “Convergence properties of the nelder–mead simplex method in low dimensions,” *SIAM Journal on optimization*, vol. 9, no. 1, pp. 112–147, 1998.
- [178] V. Bapst, T. Keck, A. Grabska-Barwińska, C. Donner, E. D. Cubuk, S. S. Schoenholz, A. Obika, A. W. Nelson, T. Back, D. Hassabis, *et al.*, “Unveiling the predictive power of static structure in glassy systems,” *Nature Physics*, vol. 16, no. 4, pp. 448–454, 2020.